12-2008

Multispectral Imaging For Face Recognition Over Varying Illumination

Hong Chang
University of Tennessee - Knoxville

To the Graduate Council:

I am submitting herewith a dissertation written by Hong Chang entitled "Multispectral Imaging For Face Recognition Over Varying Illumination." I have examined the final electronic copy of this dissertation for form and content and recommend that it be accepted in partial fulfillment of the requirements for the degree of Doctor of Philosophy, with a major in Electrical Engineering.

Mongi A. Abidi, Major Professor

We have read this dissertation and recommend its acceptance:

Paul B. Crilly, Seddik M. Djouadi, Andreas Koschan, Hamparsum Bozdogan

Accepted for the Council:

Carolyn R. Hodges

Vice Provost and Dean of the Graduate School

(Original signatures are on file with official student records.)

To the Graduate Council:

I am submitting herewith a dissertation written by Hong Chang entitled “Multispectral imaging for face recognition over varying illumination.” I have examined the final electronic copy of this dissertation for form and content and recommend that it be accepted in partial fulfillment of the requirements for the degree of Doctor of Philosophy, with a major in Electrical Engineering.

Mongi A. Abidi, Major Professor

We have read this thesis and recommend its acceptance:

Paul B. Crilly

Seddik M. Djouadi

Andreas Koschan

Hamparsum Bozdogan

Acceptance for the Council:

Carolyn R. Hodges

Vice Provost and Dean of the Graduate School

(Original signatures are on file with official student records)

Multispectral Imaging For Face Recognition Over Varying Illumination

A Dissertation
Presented for the
Doctor of Philosophy Degree

The University of Tennessee, Knoxville

Hong Chang
December 2008

Abstract

This dissertation addresses the advantage of using multispectral narrow-band images over conventional broad-band images for improved face recognition under varying illumination. To verify the effectiveness of multispectral images for improving face recognition performance, three sequential procedures are taken into action: multispectral face image acquisition, image fusion for multispectral and spectral band selection to remove information redundancy.

Several efficient image fusion algorithms are proposed and conducted on spectral narrow-band face images in comparison to conventional images. Physics-based weighted fusion and illumination adjustment fusion make good use of spectral information in multispectral imaging process. The results demonstrate that fused narrow-band images outperform the conventional broad-band images under varying illuminations. In the case where multispectral images are acquired over severe changes in daylight, the fused images outperform conventional broad-band images by up to 78%. The success of fusing multispectral images lies in the fact that multispectral images can separate the illumination information from the reflectance of objects which is impossible for conventional broad-band images.

To reduce the information redundancy among multispectral images and simplify the imaging system, distance-based band selection is proposed where a quantitative evaluation metric is defined to evaluate and differentiate the performance of multispectral narrow-band images. This method is proved to be exceptionally robust to parameter changes.

Furthermore, complexity-guided distance-based band selection is proposed using model selection criterion for an automatic selection. The performance of selected bands outperforms the conventional images by up to 15%. From the significant performance improvement via distance-based band selection and complexity-guided distance-based band selection, we prove that specific facial information carried in certain narrow-band spectral images can enhance face recognition performance compared to broad-band images. In addition, both algorithms are proved to be independent to recognition engines.

Significant performance improvement is achieved by proposed image fusion and band selection algorithms under varying illumination including outdoor daylight conditions. Our proposed imaging system and image processing algorithms lead to a new avenue of automatic face recognition system towards a better recognition performance than the conventional peer system over varying illuminations.

Publications

1. H. Chang, Y. Yao, A. Koschan, B. Abidi, and M. Abidi, “Improving face recognition via narrow-band spectral range selection using Jeffrey divergence,” accepted *IEEE Trans. on Information Forensics and Security*
2. H. Chang, A. Koschan, B. Abidi, and M. Abidi, “Fusing visible continuous spectral images for face recognition under indoor and outdoor illuminations,” accepted *Machine Vision and Applications,* 2008.
3. H. Chang, Y. Yao, A. Koschan, B. Abidi, and M. Abidi, “Spectral range selection for improving face recognition under varying illuminations,” *IEEE proc. ICIP 2008,* pp. 2756-2759.
4. H. Chang, C.-H. Won, S.G. Kong, A. Koschan, and M. Abidi, "Multispectral visible and infrared imaging for face recognition,” *Proc. IEEE Conference on Computer Vision and Pattern Recognition CVPR 2008, Fifth IEEE International Workshop on Object Tracking and Classification Beyond the Visible Spectrum (OTCBVS),* 2008.
5. H. Chang, A. Koschan, B. Abidi, and M. Abidi, “Physics-based fusion of multispectral data for improved face recognition,” *IEEE proc. ICPR2006,* vol. III, 2006, pp. 1083-1086.
6. H. Chang, H. Harishwaran, M. Yi, A. Koschan, B. Abidi, and M. Abidi, “An indoor and outdoor, Multimodal, Multispectral and Multi-illuminant database for face recognition,” *IEEE proc. CVPR2006, workshop on multi-model biometrics*, 2006, pp. 54-61.
7. H. Chang, M. Yi, H. Harishwaran, A. Koschan, B. Abidi, and M. Abidi, “Multispectral face data fusion for indoor, outdoor authentication,” *Biometrics Symposium,* 2006.
8. H. Chang and M. Howlader, “Fractional symbol differential detection for DS-CDMA over Rayleigh fading channels,” *IEEE proc. Wireless Communication and Networking Conference,* vol.1, 2004, pp. 543-547.
9. M. Howlader and H. Chang, “Performance of chip-level differential detection for DS-CDMA in multipath fading channels,” *IEEE proc. Military Communications Conference,* vol. 2, 2003, pp.1065-1070.
10. H. Chang and J. Dong, “Research in software radio architecture,” *Telecommunication Technology*, vol. 3, pp. 17-19, 2001.

Table of contents

List of figures

List of tables

1 Introduction

An increase security concern worldwide has focused public attention on the accuracy of computer-based face recognition systems for security applications, such as identity authentication and access control. As the result of the increasing requirement on safety and security issues on the public and highly secured locations, various advanced imaging system and imaging process for a better verification and recognition performance are under intensive research.

One of the main challenges to face recognition system is the degradation caused by varying illumination. In this dissertation, multispectral imaging in visible spectrum, as a new solution to illumination variation challenge, for the first time is introduced into research for the application of face recognition. There are two main reasons of employing multispectral imaging to face recognition application. First, we believe that there is unique face information contained in certain narrow-band spectral images which can be acknowledged and employed and can enhance face recognition performance compared to broad-band images. On the other hand, the broad-band imaging is not an optimal imaging solution which could have deteriorated those embedded information in the narrow-band image due to the integration process of the formation of images. The second main reason of exploring multispectral images (MSIs) for face recognition lies in the fact that multispectral images can separate the illumination information from the reflectance of objects so that we can take advantage of the illumination information to outperform conventional broad-band images. On the other hand, it is impossible to separate and employ the illumination distribution information from broad-band images.

In my dissertation, I focus on this new solution to the illumination variation challenge and plan to answer the following questions. First, is multispectral imaging system a better and more efficient system for possible superior recognition performance, especially under varying illumination? To conduct the comparison between the multiple narrow-band images and broad-band images, most advanced standard face recognition engines need to be used and the input of these engines can only be one image for one subject in face identification. Therefore, sequentially, the second question has to be what fusion algorithm on these spectral images can provide more accurate verification and identification performance. The third question is weather there is an optimal subset of these narrow-band spectral images which can also enhance the face recognition performance compared to broad-band images.

To answer the above questions, in this dissertation, sequential tasks are designed to demonstrate the effectiveness of using multispectral images compared with the conventional images. First, the collection of a large face database of multispectral images and conventional images in visible spectrum under indoor and outdoor lighting conditions need to be collected. Second, novel image fusion algorithms are required to be implemented on spectral images to obtain one fused image for each participant. Furthermore, redundancy reduction via efficient band selection algorithms are proposed and compared with the state of the art. The performance investigation and comparison are conducted via two well known commercial recognition engines and our proposed algorithms proved to be independent on recognition engines.

The remainder of this chapter outlines the motivation for this research in section 1.1. Section 1.2 gives a brief review of the state of the art. The pipeline and contributions of this dissertation are presented in section 1.3. Section 1.4 concludes this chapter with the document organization.

1.1 Motivation

Successful gate access control is essential for highly secured facilities. The most common control is guards checking identification card at gate which is shown in Figure 1.1(a). However, the card can be stolen or forged easily (Figure 1.1(b)). Plus, human checking is not stable but heavily depends on guards' performance. Automatic face recognition system for gate access is brought into attention with the quick development in computer vision techniques, computer design and sensor design. An accurate computer-based face recognition system for automatic gate access gets more attention and gives a better and more stable performance. For example, person A can get access to this room with his own valid ID card. However, person B gets A's ID card and he can get access to this room without problem, which is illustrated in Figure 1.2 (a). Suppose that there is a camera at the door and a face recognition system to compare the temporary card holder's face to true ID card holder from face database, imposter B has no chance to get into the secured room shown in Figure 1.2(b).

Existing automatic face recognition systems have demonstrated good recognition performance with frontal, centered and expressionless views of faces acquired under controlled lighting conditions [Chellappa95, Phillips98, Phillips00]. However, variability in appearance due to the changes in lighting conditions reduces the recognition performance of these systems significantly, especially when the images were acquired outdoors, even on the same day. Therefore, outdoor face recognition performance still has a large margin for improvement.

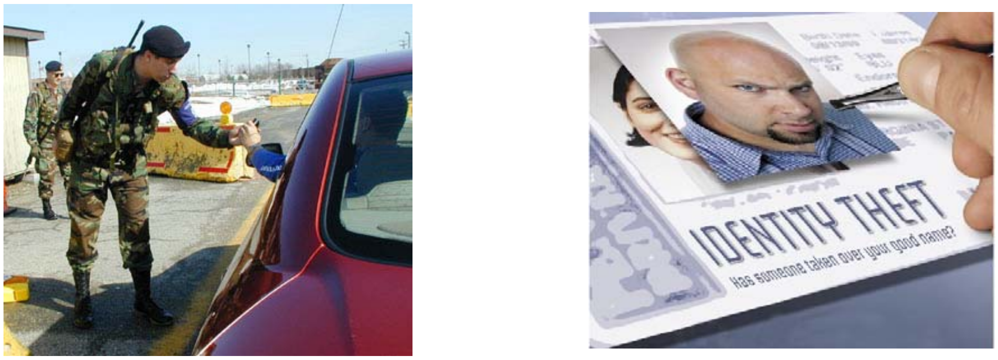

(a) (b)

Figure 1.1. (a) Guards checking ID card at the gate (http://www.delawarenationalguard.com/dngnews/mar03/signal/280th/gate_check.jpg) and (b) the illustration of an ID card can be easily forged (http://weblog.infoworld.com/zeroday/archives/images/IDTheft.jpg).

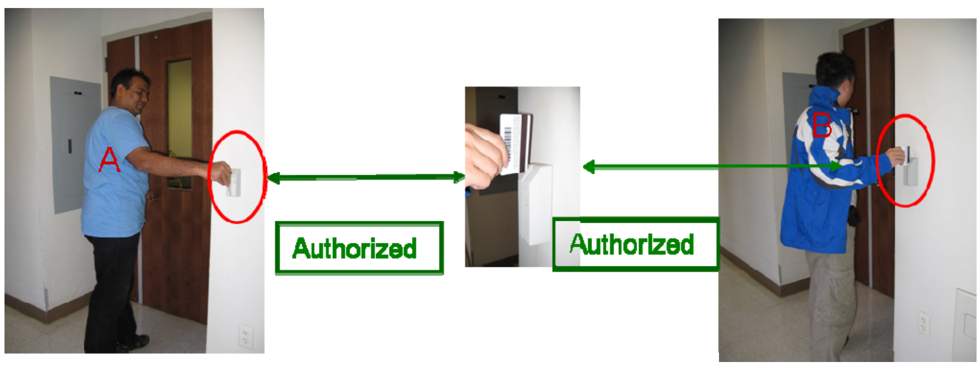

(a)

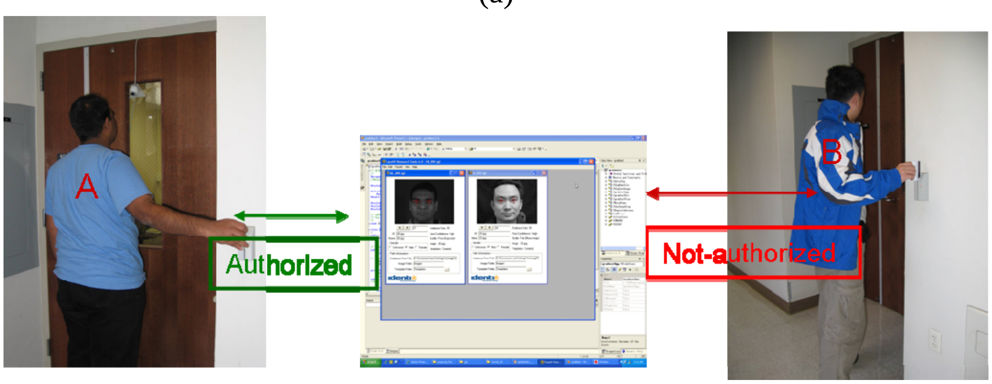

(b)

Figure 1.2. Illustration of the automatic face recognition for gate access. (a) Person B gets A's ID card and gets access to the room. (b) B is not authorized by using A's card with a face recognition system.

Conventional cameras with broad-band sensor response are used in most of the existing face recognition system. However, Broad-band images have several limitations. For example, in a color image acquisition process, the scene of interest is imaged under a given illuminant. Due to metamerism, the color image of this scene under another illuminant cannot be accurately estimated. In a word, same subject in the scene can appear very differently due to the illumination at the acquisition moment. For instance, color face image of a subject under fluorescent light in Figure 1.3(a) looks paler than the one under daylight in Figure 1.3(b). Also, we can notice how side-directional illumination causes shadows on the face in daylight. Two monochromatic images of another subject with different illuminations and directions are shown in Figure 1.3(c) and (d). Another limitation is the integration process of the formation of the broad-band images. This integration could degrade the information that might be very useful in certain narrow range of wavelength.

To illustrate varying illumination effects on the face recognition performance, a set of experiment is given to in Table 1.1. Gallery images are acquired under indoor halogen light. Two probe sets are acquired under indoor the same halogen light at different time and under daylight. Table 1.1 demonstrates dramatic degradation in face recognition performance caused by illumination changes from indoor halogen light to outdoor daylight.

Very few researchers have exploited raw multispectral images to improve face recognition. One of the main reasons is that most of the multispectral imaging tools are specified and customized for certain area research and applications. First, there are not many multispectral cameras available for face recognition application. Secondly, a good multispectral face database which can be used for testing is urgently needed in the research direction. Thirdly, even though face recognition has received increasing attention in recent research, very few researchers have effectively utilized multispectral image fusion to improve face recognition. The fusion of multispectral images has been used in many applications, such as analysis of satellite data, and has yielded better recognition than single broad band processing.

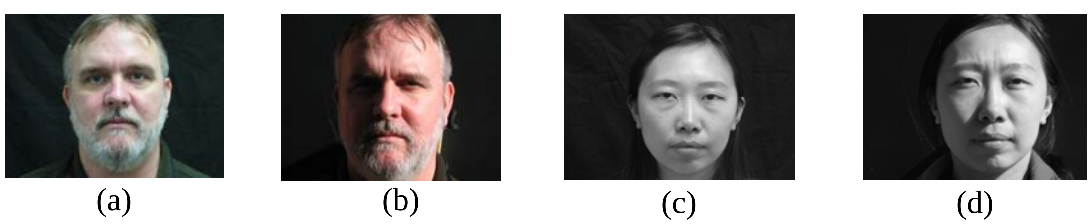

Figure 1.3. Face under different lighting conditions: (a) an RGB color image of a male subject under fluorescent light, (b) an RGB color image of the same subject by the same camera under daylight, (c) a monochromatic image of a female subject under fluorescent light, and (d) a monochromatic image of the same subject by the same camera under daylight.

Table 1.1. Rank-one value of two probe sets, one under halogen light and the other is under daylight.

Data set	Gallery	Probe 1	Probe 2
Illumination	Indoor halogen	Indoor fluorescent	Outdoor daylight
Rank-one (%)		88%	40%

MSIs give access to more useful information since narrow-band images can enhance certain features that otherwise might go unnoticed in images acquired by a monochrome or color camera. In addition, multispectral imaging allows the spectral distribution of an imaged object to be distinguished from others [Fairchild01]. This facilitates recognition in situations where an ordinary imaging system might not be able to separate the effects of illumination from changes in the object. Inspired by these thoughts, a practical multispectral imaging and spectral image fusion can be a new avenue for better face recognition under varying illumination.

In image fusion, my goal is to fuse narrow-band spectral images which can outperform conventional broad-band images, especially when the probe and gallery images are acquired under different illuminations. This lies in the fact that with multispectral images, we have the freedom to emphasize and/or suppress the contribution of images from certain narrow bands. Contrarily, conventional broad-band images provide only compromised broad-band responses. Also, we make use of this illumination information in image fusion so that the illumination-adjusted face images can outperform the conventional ones. Last but not least, searching for optimal subset of spectral bands is our ultimate goal so that a simple spectral imaging system can be achieved. Two different well-known recognition engines can be employed to verify the generality of the algorithms. A simplified multispectral face imaging system can be achieved based on this work and it can be practically used for a customized sensor associated with given illuminations to benefit the security system based on face recognition.

1.2 State of the art

Although approaches to improved face recognition performance have been intensively studied, most of the existing work has drawbacks while it gains some performance. Chen *et al.* [Chen06] summarized the main algorithms towards the goal of improving the performance under varying lighting conditions. They classified these into three main algorithm categories: (a) preprocessing and normalization, (b) invariant feature extraction, and (c) face modeling. Preprocessing and normalization, such as histogram equalization, gamma correction, and more local processing [Pizer87, Shan03, Xie05] are easy to implement but may not provide the best results. Edge maps, derivatives of the gray-level and Gabor-like filters [Cootes98] are all regarded as illumination invariant signature images. However, empirical studies show that none of these representations are sufficient to overcome image variations due to changes in the direction of illumination. 3-D face model can be used to render face images with different poses and under varying lighting conditions [Moghaddam00, Liu98].

Multispectral imaging has been widely used in various fields, such as remote sensing for resource monitoring, medicine, agriculture, manufacturing, forensics, etc. In this technology, information is collected over contiguous narrow wavelength intervals across the visible, near infrared or infrared regions and can generate precise optical spectra at every pixel.

Most common multispectral imaging for face recognition uses the near infrared range of spectrum with visual images because the face images captured using thermal infrared sensors is nearly invariant to changes in ambient illumination [Socolinsky01, Bebis06]. This fusion can bring extra information other than visible spectral domain to improve face recognition [Kong07]. In literature, fusion multispectral images for face recognition can be grouped into two categories: fusion near infrared broad-band with visible domain broad-band images [Kong05] and fusion narrow NIR band images with visible domain broad-band images.

The Munsell Color Science Laboratory initiated efforts with multispectral images using a Liquid crystal tunable filter (LCTF) over the visible spectrum, especially for high resolution art portrait reconstruction [Imai96, Imai00]. They also acquired the Lippmann2000 database [Rosen99] that contains spectral images of several objects including faces from 4 Caucasians and 3 East-Asians. This data was acquired by a film camera with approximately 15-25s lapses between exposures and 16 exposures for each person, under flash lighting. Pan *et al.* [Pan03, Pan04, Pan05] used narrow-band spectral images in near infrared. However, there was no direct recognition performance comparison between their method and the conventional broad-band images in visible domain.

1.3 Contributions

The pipeline of this dissertation work is illustrated in Figure 1.4. There are five blocks including my three contributions in two of them with yellow highlights. The framework is designed for verification of our proposed idea that multispectral images can outperform the broad-band images. Therefore, first, a multispectral imaging system and multispectral face database are needed. Then, the image processing includes two sections and two three contributions. The first section and contribution is multispectral image fusion. To simplify our imaging system, optimal spectral band selection should be conducted to the multispectral face data before the recognition comparison. Two novel algorithms that automatically specifies the optimal spectral band selection is proposed as the second and third contributions.

A solid foundation of my work is the design of the multispectral imaging system for data acquisition which includes hardware design and user interface development. Eventually, a complete face database is obtained for our theory study. The database includes narrow-band spectral face images, conventional broad-band images, and the illumination information of each data record. Accordingly, my three contributions are described as follows.

- **Image fusion:** Image fusion is one of the most powerful techniques to explore information and reduce noise among multiple images. In addition, in order to use the most advanced accessible recognition engines which are developed in the way that the smallest input unit is a two-dimensional image, we also need image fusion to reduce three-dimensional information of narrow-band spectral images to two-dimensional images as a direct input to the engines. Therefore, image fusion on spectral images is necessary and required. The proposed fusion algorithms of MSIs, including physics-based weighted fusion, illumination adjustment, wavelet fusion and rank-based decision level fusion, are proved to outperform conventional broad-band images under varying illuminations. The reason for a better performance from proposed algorithms lies in the fact that proposed algorithms can take advantage of the narrow-band spectral information which is not available for conventional images. Their performances are also better than

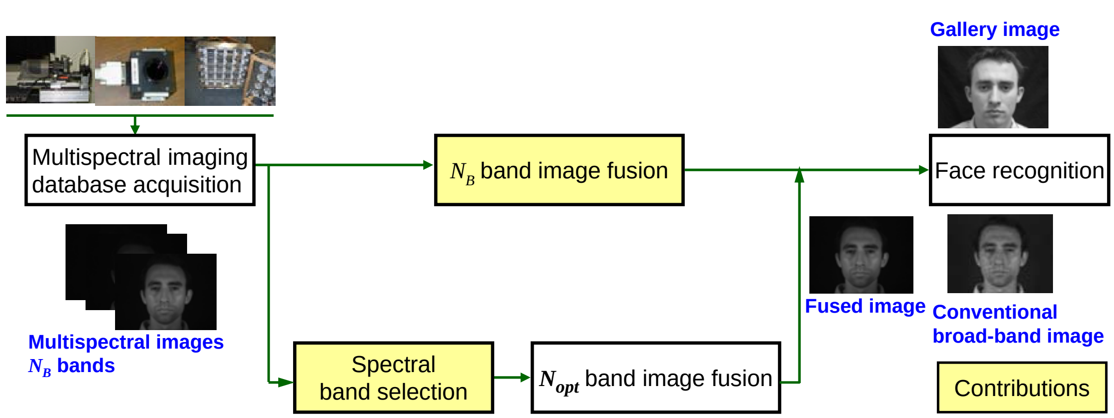

Figure 1.4. Pipeline of the dissertation work.

principal component analysis (PCA) fusion and averaging fusion. The fused narrow-band images by proposed algorithms outperform conventional broad-band images by up to 78%.

- **Distance-based band selection:** In a stack of multispectral images, there is more information than conventional one broad-band image for potential better performance. In the meanwhile, the performances of multispectral bands different substantially. To reduce the volume of data handling and system complexity, it is desired to select a subset of those multispectral bands for consecutive processing. Therefore, I propose a novel band selection algorithm for the narrow-band spectral face images customized for face recognition application. This algorithm provides the ranked band candidates for improved face recognition performance in visible domain. The novelty of this method lies in the introduction of quantitative performance evaluation metric which uses distribution separation measure and the selection of the optimal bands by ranking these separation values. In this algorithm, kernel density estimation is used to estimate the distributions of the genuine and imposter sets for one band images. A promising property of this method is the robustness to changes of each of the free parameters in the algorithm, such as different kernels, different smoothing parameters and various distance measures. From experiments, the top one, two or three ranked bands are proved to outperform the conventional images and state of the art.
- **Complexity-guided distance-based band selection:** This is an automatic band selection algorithm which balances the band selection results between the performance metric and the dependency/correlation among bands. The balance is achieved by conducting the model selection criterion-information complexity to the performance metric. The selected bands have been proved with effectiveness by experiments from both simulated data and real data with different illumination conditions. The selected bands outperform the conventional images by up to 15%. A simple and practical multispectral face imaging system can be customized and it will benefit the security system based on biometric recognition.

1.4 Document organization

According to the aforementioned topics and pipeline, the remainder of this dissertation is organized as follows:

- Chapter 2 reviews existing work in the topics covered by this dissertation work, including face recognition algorithms, multispectral imaging systems, multispectral image fusion, and band selection algorithms.

- Chapter 3 describes the hardware development of our multispectral imaging system and the graphic user interface development for acquisition and synchronization between equipments. In addition, our multispectral face database description is presented in this chapter.
- Chapter 4 presents the work in multispectral image fusion. The proposed physics-based weighted fusion, illumination adjustment and rank-based decision level fusion are described in details and several experimental results have shown the improvement of the proposed algorithms in face recognition performance while the gallery and probe image are acquired under different illuminants.
- Chapter 5 discusses the distance-based band selection algorithm. The introduction and knowledge background of similarity scores are explained. Then the description of the algorithm is given in details. Last but not least, the ranked band selection results from four independent experiments demonstrate extraordinary robustness of this algorithm.
- Chapter 6 gives the complexity-guided distance-based band selection algorithm. This is an improved distance-based band selection algorithm using the model selection criterion, information complexity in the form of multivariate kernel estimation to achieve the automatic selection of the number of bands. This chapter also presents the efficiency and improvement of our proposed band selection algorithms by multiple experiments, including both simulated data sets and real face data sets.
- Chapter 7 concludes my work and contributions in multispectral imaging for face recognition over varying illuminations. Several potential avenues of performance improvement are also discussed in this chapter.

2 Related work

The needs for robust face recognition systems are extensive in a practical world with pressing issues in identity authentication and recognition. A substantial evolution has been made in face recognition research over the last 20 years. However, the use of multispectral images for face recognition is a relatively new application area that so far has only been studied by a few research groups.

This chapter discusses research work in three relevant areas: section 2.1 addresses the challenges to face recognition and existing approaches to these challenges. Section 2.2 reviews various types of multispectral imaging systems. Section 2.3 discusses existing image fusion algorithms for multispectral images and spectral band selection algorithms.

2.1 Challenges to face recognition

Automatic face recognition system for gate access is brought into attention with the quick development in computer vision techniques, computer design and sensor design. Existing automatic face recognition systems have demonstrated good recognition performance with frontal, centered and expressionless views of faces acquired under controlled lighting conditions [Chellappa95, Phillips98, Phillips00].

US government funded competitions allow for direct comparisons among multiple recognition algorithms. Performance is measured in these competitions using standardized evaluation procedures applied to large sets of facial images (e.g., Face Recognition Technology (FERET) [Phillips00], Face Recognition Vendor Test 2000 [Blackburn01], Face Recognition Vendor Test 2002, [Phillips02], and Face Recognition Grand Challenge (FRGC) [Phillips06]). However, variability in appearance due to the changes in lighting conditions, pose, facial expression, and disguise reduces the recognition performance of these systems significantly. Due to difficulty in controlling the lighting conditions in practical applications, variable illumination is one of the most challenging problems with face recognition. In this dissertation, we focus on the algorithms that improve the performance under various illuminations.

2.1.1 Face recognition

Face recognition starts typically with image preprocessing, including segmentation and enhancement normalization. For example, in the face recognition system in Colorado State University, image preprocess includes the following steps [Blome05]. 1. Integer to float conversion. 2. Geometric normalization – Lines up human chosen eye coordinates. 3. Masking – Crops the image using an elliptical mask and image borders such that only the face from forehead to chin and cheek to cheek is visible. 4. Histogram equalization – Equalizes the histogram of the unmasked part of the image. 5. Pixel normalization – scales the pixel values to have a mean of zero and a standard deviation of one. The FERET 1996/97 studies pre-processed the raw face data. This pre-processing is a critical to many of the algorithms distributed though this web site. The original code for preprocessing of the FERET data is distributed with the National Institute of Standards and Technology data.

After image preprocessing, feature extraction is required to represent high dimensional image data into low dimensional feature vectors. In other words, many researchers have focused on face representation techniques that are invariant to some of these variations [Grudin00, Kong07]. In general, there are two approaches to feature extraction, a local method and a global method. Local feature extraction is based on the localization of salient facial features, such as the eyes, eyebrows, nose, mouth and their interrelation [Wiskott97, Tefas01, Viola03, Gokberk07, Yuille89, Zuo03, Zuo04, Wang06, Tu07]. These feature extraction methods use prior knowledge of geometric relation with regard to facial topology. In a global method, faces are represented as a whole and statistical techniques are used to extract features from faces [Moghaddam02, Kim04, Liu00, Liu06, Turk91, Belhumeur97]. The most famous one among the global methods is Principal Component Analysis (PCA) [Turk1991] which employs principal component analysis to form eigenfaces as a characterization for recognition. It is a global method because it extracts face features using the bases which describe a whole face. For example, the feature extraction technique is based on local feature analysis of facial texture vial multi-scale filters from the available document online. There are also hybrid approaches which incorporate complementary knowledge from both [Liu03]. Classifier is used after the feature extraction.

Face recognition has proved to be a difficult problem in computer vision because of intra-personal variations caused by facial expressions, view point changes, and illumination variations are significant when compared to inter-personal variations. The face recognition is processed by well-known recognition engines in our work. Those face recognition algorithms are patented by those commercial companies and they are basically black box to us. Therefore, face recognition algorithms are not in the main scope of my research.

2.1.2 Illumination variation

Adini *et al.* concluded [Adini97] that “The variations between the images of the same face due to illumination and viewing direction are almost always larger than image variations due to change in face identity”. Person identification from a facial image across lighting variations is still the most challenging problem in face recognition. Phillips *et al*. [Phillips03] discussed that outdoor face recognition performance is significantly reduced, indicating that the variation and structure of outdoor lighting has a drastic affect on performance.

Many methods have been proposed to solve this problem with improvements in face recognition. Preprocessing and normalization with global processing techniques [Savvides03], such as histogram equalization and gamma correction, were easy to implement but provides inferior performance while non-uniform illumination variation exists. Recently, more local processing, such as adaptive histogram equalization [Pizer87], region-based histogram equalization [Shan03], and block-based histogram equalization [Xie05] have also been proposed to cope with non-uniform illumination variations. [Pizer87] computed the histogram of a local image region centered at a given pixel to determine the mapped value for that pixel; this can achieve a local contrast enhancement. However, the enhancement often leaded to noise amplification in “flat” regions, and “ring” artifacts at strong edges. In addition, this technique was computationally intensive. Vossepoel *et al.* [Vossepoel88] and Jim *et al.* [Jin01] introduced some modified adaptive histogram equalization methods. [Chen06] presented an illumination normalization approach using a discrete cosine transform to compensate for illumination variations.

Although recognition rates on face databases with non-uniform illumination variations could be improved compared with the histogram equalization, their performance improvement needed many assumptions. Zhao and Chellappa [Zhao00] developed a shape-based face recognition system by means of an illumination-independent ratio image derived by applying a symmetric shape-from-shading technique to face images. However, this method is only efficient for exact frontal face images and it is assumed that all faces share a similar common shape. Riklin-Raviv and Shashua [Riklin-Raviv99] used quotient images to solve the problem of class-based recognition and image-synthesis under varying illumination. Zhao *et al.* [Zhao03] proposed illumination ratio images, which can be used to generate new training images for face recognition with a single frontal view.

Early works in illumination-invariant face recognition was also focused on image representations that are mostly insensitive to changes under various lighting. Edge maps, derivatives of the gray-level and Gabor-like filters [Cootes98] are all regarded as illumination invariant signature images. However, empirical studies show that none of these representations are sufficient to overcome image variations due to changes in the direction of illumination. First, the different representations of image can be only extracted once they overcome some degree of illumination variations. Second, features for the person’s identity are weakened whereas the illumination-invariant features are extracted. However, empirical studies show that none of these representations are sufficient to overcome image variations due to changes in the direction of illumination. Another well-known feature extraction method is called fisherface also known as linear discriminant analysis which linearly projects the image space to a low-dimensional subspace to discount variations in lighting and facial expressions [Belhumeur97]. [Jian07] in depth presented automatic parameters selection for kernel -based linear discriminant analysis method.

Face recognition from 3D image data is another topic being actively studied by researchers [Zhang02, Clarkson01]. 3-D face model can be used to render face images with different poses and under varying lighting conditions [Bronstein04, Moghaddam00, Liu98]. The illumination subspace approach [Georghiades98] was reported to perform significantly better for unknown illumination. However, this method requireed a set of training images which is not always available to construct an illumination cone of a face taken under unknown lighting conditions.

Linear subspace method, Lambertian surface of an image under varying illumination, was discussed in [Hallinan94, Bichsel95, Belhumeur97, Shashua97]. A 3D linear subspace of the image space, three or more images of an object under different lighting conditions can be used to compute a basis for the 3D illumination subspace.

Recently, some researchers attempt to construct a generative 3-D face model that can be used to render face images with different poses and under varying lighting conditions. A generative model called illumination cone was presented in [Belhumeur98, Georghiades98, Georghiades00]. The main idea of this method was that the set of face images in fixed pose but under different illumination conditions can be represented using an illumination convex cone which can be constructed from a number of images acquired under variable lighting conditions and the illumination cone can be approximated in a low-dimensional linear subspace. Ishiyama and Sakamoto [Ishiyama01] proposed a geodesic illumination basis model, which calculates pose-independent illumination bases for a 3D model; these bases are warped into view-dependent bases for any pose. In [Basri03], the authors showed that the set of images of a convex Lambertian object obtained under a variety of lighting conditions can be well approximated by a 9D linear subspace. One of the drawbacks of the model-based approaches is that a number of images of the subject under varying lighting conditions or 3-D shape information are needed during the training phase. This drawback limits its applications in practical face recognition systems. In addition, existing model-based approaches assume that the human face is a convex object. The specularity problem is also ignored even though the human face is not a perfect Lambertian surface.

Another promising approach is to combine infrared with visual images because the face images captured using thermal infrared sensors is nearly invariant to changes in ambient illumination [Socolinsky01, Bebis06]. The recognition results in [Kong05, Kong07] showed that both visible and near infrared imagery perform similarly across algorithms and that fusion of infrared and visible imagery is a viable means of enhancing performance beyond that of either acting alone. However, these approaches can not be done with a single camera and also require a registration procedure.

2.1.3 Face databases

Not since the mid 1990s has there been such a renewed interest in developing new methods for automatic face recognition. This renewed interest has been fueled by advances in computer vision techniques, computer design, sensor design, and interest in fielding face recognition systems. These techniques hold the promise of reducing the error rate in face recognition systems by an order of magnitude over the Face Recognition Vendor Test 2002 results. The Face Recognition Grand Challenge is being conducted to fulfill the promise of these new techniques. In the last couple years there have been advances in computer graphics and computer vision on modeling lighting and pose changes in facial imagery. These advances have lead to the development of new computer algorithms that can automatically correct for lighting and pose changes in facial imagery. These new algorithms work by preprocessing a facial image to correct for lighting and pose prior to being processed through a face recognition system.

Face databases are crucial for testing face recognition methods. Many databases have been collected with the intent of promoting face recognition research. Programs like the Facial Recognition Technology [Blackburn00] and Face Recognition Grand Challenge [Phillips05] have shown great interest in furthering face recognition technologies by providing the necessary face images for testing.

Face databases using the visual modality have been collected over the past years in abundance. They are very useful in visual face recognition applications and experiments. Databases like the AR [Martinez98], BANCA [Bailly-Bailliere03], CAS-PEAL [Gao04], CMU PIE [Gross01], FERET [Blackburn00], Korean (KDFB) [Hwang04], and University of Texas [O'Toole05] face databases have been used heavily in face recognition research. Images are typically grayscale or color, with images of people taken under different resolutions, ethnicity, illumination, pose and expression. These databases do not include images from the infrared spectrum.

Multimodal databases are made of images acquired under different imaging sensors, typically with visual and thermal imaging sensors. For facial images the sensors used most widely are long wave infrared (LWIR), and visible wavelength CCD arrays. In our previous work, we have collected a visual and thermal image database to investigate the effects of pose and illumination changes and to study the case of registration of visual and thermal images using Gaussian fields [IRIS03]. The images accessible at the Equinox database are simultaneously imaged in the LWIR (0.8-1.4 μm), and in the visible wavelength spectrum. Image frame sequences with different expressions were acquired simultaneously for both modalities. Additional images were taken for participants who wore glasses. In addition, three static images were taken with frontal illumination while smiling, frowning and with a surprised expression [Socolinksy01]. The Notre Dame database [Flynn03] has images from visual and thermal modalities of people under different illumination and poses.

Munsell Color Science Laboratory has conducted a huge amount of research with multispectral images using a liquid crystal tunable filter over the visual spectrum, especially for high resolution art portrait reconstruction [Imai98, Imai01]. They also offer the Lippmann2000 database [Rosen99] that contains spectral images of several objects including faces from 4 Caucasians and 3 East-Asians. This data was acquired by a film camera with approximately 15-25s lapses between exposures and 16 exposures for each person, under flash lighting. Pan *et al*. [Pan03, Pan04] acquired spectral images over the near-infrared spectrum (700-1000nm) and demonstrated that spectral images of faces acquired in the near infrared range can be used to recognize an individual under different poses and expressions. It is evident from the literature that not much research has been done using MS imaging in the visible domain to address the problem of face recognition, especially with respect to changes in illumination conditions. They did not compare the recognition performance by grey-level images under the similar lighting conditions.

2.2 Multispectral imaging

Multispectral imaging is a technique that provides images of a scene at multiple wavelengths and can generate precise optical spectra at every pixel. Multispectral imaging produces three dimensional image cube with two spatial dimensions (horizontal and vertical) and one spectral dimension. The spectral dimension contains spectral information for each pixel on the multispectral cube. Multispectral imaging can enhance and expand the capability of detecting materials as well as the spatial distributions. For example, spin-offs from NASA's multi- and hyper-spectral imaging remote sensing technology developed for earth resources monitoring, are creative techniques that combine and integrate spectral with spatial methods. Such techniques are finding use in medicine, agriculture, manufacturing, forensics, and an ever expanding list of other applications which is shown in Figure 2.1. The images are obtained from (a) http://jrscience.wcp.muohio.edu/photos/ Keith100100multispectral.jpg; (b) http://www.fs.fed.us/r5/rsl/local-resources/images/ remotesensing/ mss.gif, (c) http://www.ars.usda.gov/is/AR/archive/aug02/food0802.htm, (d) www.acg.cit.ie/project3.jpg, and (e) http://www.neuroscience.med.utah.edu/Faculty /MarcAnim_kainate _bcs.gif. Many such applications are easier to implement using a sensor design different from the push-broom or whiskbroom air- or space-borne counterparts [Gat00].

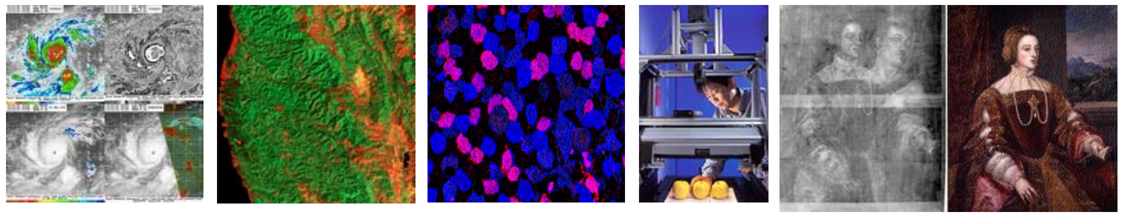

(a) (b) (c) (d) (e)

Figure 2.1. Multispectral imaging has been used in (a) weather forecast, http://jrscience.wcp.muohio.edu/photos/ Keith100100multispectral.jpg; (b) resource information, http://www.fs.fed.us/r5/rsl/local-resources /images/remotesensing/mss.gif, (c) biomedical imaging, http://www.ars.usda.gov/is/AR/archive/aug02/food0802.htm; (d) fruit quality monitoring, www.acg.cit.ie/project3.jpg, and (e) art/color reproduction, http://www.neuroscience.med.utah.edu/Faculty/MarcAnim_kainate_bcs.gif

Multispectral or hyperspectral sensors collect the electromagnetic spectrum at dozens or hundreds of wavelength ranges in the visible and near infrared spectra. Spectral resolution of a multispectral sensor is higher and is defined as a measure of the narrowest spectral wavelength that can be resolved by a sensor.

Due to hardware limitations (i.e. most of the color cameras are RGB cameras) all the spectral information is converted to RGB triplets during image acquisition. It is a projection from an infinitely dimensional color space to a three dimensional space, or many-to-one projection which results in colors with different spectral distributions giving the same RGB response. Colors with the same tristimulus data but with different power distributions are called metameric colors [Drew92, Jaehne00].

The compromise between tristimulus data collection and spectrographic information is the employment of multiple (more than 3) color filters with narrow bandwidth mounted in front of a camera. Such an apparatus allows us to obtain spatial information about the imaged scene at high spectral resolution. The collection and processing of 2D images of the same scene under many spectral (often narrow bandpass) filters, particularly in the visible range, is often referred to as multispectral imaging [Poger01].

According to the process of multispectral imaging, we first introduce light sources and illumination definition and the effects on acquired images with different lighting conditions in section 2.2.1. Then human skin reflectance is discussed in section 2.2.2. Multispectral imaging system with a monochromatic camera and a rotating wheel is presented in section 2.2.3. Last but not least, multispectral imaging system with liquid crystal tunable filter is introduced in section 2.2.4.

2.2.1 Light sources

Light is the portion of electromagnetic radiation that can be detected by the human eye. The wavelengths visible to humans lie between x-rays and radio waves, exhibiting a unique mix of ray, wave, and quantum properties. Figure 2.2 shows the photonic spectrum with the highlighted visible spectrum. Human eyes can only observe very limited part of the whole spectrum, visible spectrum which is around the range of 400nm to 720nm. The color that we can perceive from 400nm to 720nm is from violet to blue, then green, orange to red. X-rays has been used in medicine and ultraviolet rays has been widely use in crime detection. Infrared rays are used in all type of equipments to detect lives which can not be seen by human eyes.

Light sources have been used for hundreds of years and it has created a whole new world and effect the scientific research from the first day they were created. The sun, moon and stars are the natural light sources. Light bulbs and tubes have been tremendous used in many applications. Light sources have some basic properties, such as the power, radiance, luminance, etc. Some of the characteristics of any light source are shown in Table 2.1. The photomatrics of some light sources can be quite different and even for the same light source, there are still changes. For example, in a bright sunny day, the illuminance is as high as 100 Klux. However, it is only 2 Klux when it is very cloudy.

In computer vision, the light's propagating wave front is modeled as a ray traveling in a straight line. The spectral distribution of the illumination existing during image acquisition has an influence on the generated color image. The color of a face, which was photographed in the light of the midday sun, appears totally different in the photo of this same face that was acquired at sunset or under indoor lighting. In order to reduce this variety, some spectral distributions were standardized internationally. Standard

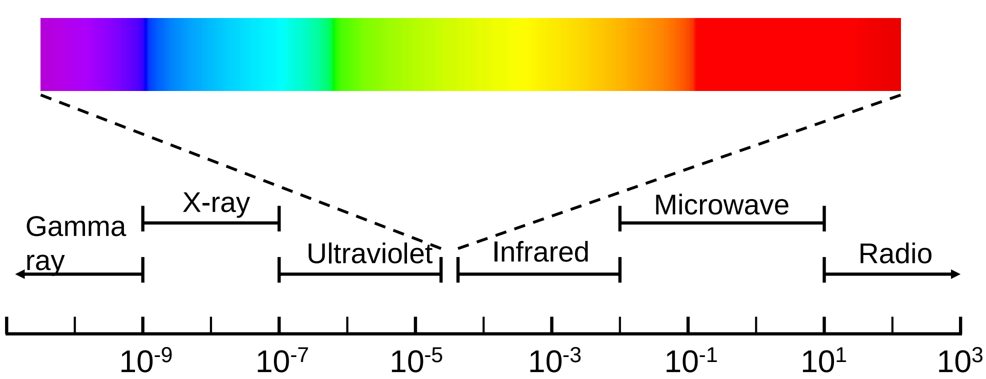

Figure 2.2. Photonic spectrum with the highlighted visible spectrum, adopted from http://anothro.palomar.edu/primate/images/spectrum.gif

Table 2.1. Definitions of light source properties

Quantity	Radiometric	Photometric
Power	Radiant Flux watt (W)	Luminous Flux lumen (lm)
Power per unit solid angle	Radiant Intensity	Luminous Intensity candela (cd)
Power per unit area	Irradiance	Illuminance lux(lx)
Power per area / solid angle	Radiance	Luminance cd/m^2= nit

illuminants were set in 1931 by the International Commission on Illumination CIE (and were subsequently adopted in the German standard DIN 5033). The spectral distribution of the illumination directly influences the perceived or measured body color of the illuminated object. The spectral power distribution depends on the wavelength and the color temperature. As representative for average daylight with the most similar color temperature 6500 K, this standard illuminant was set as *D*65. Earlier the standard illuminant *C* (the most similar color temperature, likewise at 6500 K) was used for "daylight". The disadvantage of the standard illuminant *D*65 is that it cannot be reproduced by any technical lighting source. At the present time filtered short arc Xenon lamps are the nearest alternative to *D*65. In DIN 5033 the illuminants *B* (sunlight), *G* (tungsten light), as well as *D*50, *D*55, and *D*75 are specified. However, they are not regarded as standard illuminants. Standard illuminants also play a role in the calculation of color constancy. Most of the knowledge can be referred to [Koschan08].

2.2.2 Human skin reflectance

Skin color detection has become an often used cue in computer vision for detecting, segmenting, and tracking face and hands in the past 10 years. It is used in many different applications, such as motion capture, human-computer interaction, access control, surveillance, and content-based image retrieval and indexing of image databases. The majority of existing skin color data is in the form of Red-Green-Blue (RGB) triplets. For most cases, describing color in the tristimulus space is sufficient for communicating color information to a human observer. However, Hall concluded that [Hall83, Hall99] if the whole computation of light reflection and transfer is performed in tristimulus space significant color distortions are introduced.

Skin reflectance has been modeled using Monte Carlo simulation [Hanrahan93], and several aggregate reflectance descriptions have been recorded from real people [Marschner99]. Ohtsuki *et al.* [Ohtsuki98] have looked into exploiting skin spectrograph data in skin color detection and modeling. However, their techniques are limited to using

RGB input images. A more accurate color descriptor that directly depicts the optical properties of the material is the ratio of the amount of reflected light divided by the amount of incident light over a continuum of wavelengths. Stoerring *et al.* [Stoerring99, Stoerring00] have used a skin reflectance model over the 300-800nm range to propose a method for skin detection under varying lighting conditions. In particular, a combination of standard RGB bands with three near infrared bands below 100nm is investigated. A skin reflectance model has also been used to synthesize face images after changes in lighting and viewpoint [Debevec00]. Recent research [Angelopoulou01] has measured skin reflectance spectra over the visible wavelengths and proposed models for the spectra. They suggested capturing skin reflectance with five band-pass filters assuming the illumination is known. The existence of the "W" pattern implies the presence of live human skin, which is supported by the physics of skin reflectance [Van Gemert89, Clement85].

2.2.3 Multispectral imaging using rotating wheels

In recent years, modern spectral image capture systems tend to rely on combinations of CCD cameras with various types of narrow or broad band filters [Imai96]. The images are then processed using normal high-capacity computational machinery with software developed to properly treat the spectral data. Therefore, capturing multispectral images can be accomplished by swapping narrow band-pass glass filters in front of the camera lens. It is common for such filters to be mounted in a filter wheel. Nowadays, color filters with minimum bandwidth of approximately 10 nm are available off-the-shelf.

Ohta *et al.* [Ohta81] used a film-based system for multispectral image capture. They used a mechanical rotating filter wheel with eight gelatin filters and imaged rigid objects. Only rays within a small wavelength band experience constructive interference and pass through the interference filters. In such use interference filters offer a large aperture, large field of view, and good optical quality.

Different filters and combinations were proposed for different applications. Tominaga proposed a six-color camera system with six color filters [Tominago96], which had six spectral channels of the color filters' fixed wavelength bands. However, these fixed-filter systems have essential restrictions: (1) the selection of color filters and the number of filters are limited, and (2) filters with a narrow band-pass are difficult to make. (3) Since it is a mechanical system selecting the filters, moving parts are necessary. Therefore, Time on the order of seconds can be required to step filters in a preset sequence. (4) To reduce calibration and registration concerns, the number of moving parts needed to be minimized.

2.2.4 Multispectral imaging using electronically tunable filters

A more elegant solution involves electronically tunable filters (ETFs). A tunable filter is a device whose spectral transmission can be electronically controlled through the application of voltage or acoustic signal, etc. In addition, the large aperture and imaging capability of these devices represent a distinct advantage over conventional dispersive spectral analysis techniques. Unlike conventional filter wheels, there are no moving parts and no discontinuity in the spectral transmission range, thus providing finer spectral sampling, and rapid and random switching between color bands. Also, they are light weight, making them attractive for airborne or remote sensor platforms. A wide variety of different ETFs is commercially available and the principles of operation of each of the ETF categories and introduce their advantages and limitations are discussed in [Poger01]. [Gat00] reviews more details of the available tunable filters, system design considerations, and general analysis techniques for retrieving the intrinsic scene properties from the measurements, and applications and examples.

Electronically tunable filters offer the fastest, most accurate and flexible color filtering techniques that are currently available. The majority of ETFs can be classified under three categories: liquid crystal devices based on birefringence, Acousto-Optical based on diffraction, and Fabry-Perot based on optical interference. Each of these three types has its own peculiarities. Although each of the three types of ETFs is based on different principles of optics, each of them is successful in selecting individual band pass over a continuum of spectral ranges with high speed and accuracy. Nowadays, a considerable variety of Liquid Crystal Tunable Filters, Acousto-Optic Tunable Filters, and Electro-Optic Fabry-Perot is available in the market. Most of them have comparable performance characteristics. For successful multispectral imaging, one should choose the apparatus that best fits the application at hand. Figure 2.3 shows the rotating wheels, the specified multispectral camera and a multispectral imaging system with liquid crystal tunable filter in front of a camera.

This multispectral imaging system has been used by several research groups [Imai96, Imai98, Imai01, Pan03, Pan04, Pan05, Hardeberg02, Rosen99, Tominago96] for many applications. The Munsell Color Science Laboratory initiated efforts with multispectral images using a liquid crystal tunable filter over the visible spectrum, especially for high resolution art portrait reconstruction [Imai96, Imai98, Imai01]. They also acquired the Lippmann2000 database [Rosen99] that contains spectral images of several objects including faces from 4 Caucasians and 3 East-Asians. This data was acquired by a film camera with approximately 15 to 25 second lapses between exposures and 16 exposures for each person, under flash lighting.

Pan *et al*. [Pan03, Pan04, Pan05] acquired spectral images over the near-infrared spectrum (700-1000nm) and demonstrated that spectral images of faces acquired in the

(a) (b) (c)

Figure 2.3. Different multispectral imaging systems. (a) a camera with rotating wheels (http://www.isl.titech.ac.jp/~guchi/NV/NV-IntroE.html), (b) specified multispectral camera (http://images.Vertmarkets.com/ crlive/files/Images/9974C610-6524-4EB9-A4D 4-E6E2066427AE/orion.jpg), and (c) cameras with liquid crystal tunable filters in front (http://www.techexpo.com/WWW/opto-knowledge /E-tunable-filters.pdf).

near infrared range can be used to recognize an individual under different poses and expressions. It is evident from the literature that not much research has been done using multispectral imaging in the visible domain to address the problem of face recognition, especially with respect to changes in illumination conditions. The multispectral databases mentioned above either have very few data records or are not in the visible spectrum. In addition, these datasets were not compared with the conventional face images by recognition engines.

2.3 Multispectral image fusion

Image fusion is a general technique to combine two or more images to gain more information than from each image alone. Image fusion can be classified into two groups, multi-sensor fusion and same-sensor fusion according to acquisition sensors. Multi-sensor fusion combines the information carried and acquired by different sensors, for example, IR and visible sensors [Lallier00, Toet03, Abidi04, Luo95]. The same-sensor images are acquired by the same sensor but with different shoots. The purpose of the fusion of same-sensor images is to either enhance or augment scene information, such as panorama or multi-perspective mosaic. Same-sensor fusion is usually constrained by the physics-limitation of the sensor. Most of the fusion algorithms need registration to align two or more images. Image fusion can also be grouped by processing levels, such as pixel-based and feature-based fusion. Pixel-based fusions are easy to implement but more sensitive to registration errors. Feature-based fusion methods are more computationally complex but robust to registration errors. There have been many fusion algorithms for hyperspectral images, among which the most popular are based on the Wavelet, PCA, and Intensity-Hue-Saturation transforms [Wang05, Sadjadi05, Gonzalez-Audicana04, Gonzalez-Audicana06, Pohl98].

Image fusion is not commonly used for face recognition except biometric fusion for multi-modal biometrics, such as face, palm print, signature, iris, and gait to improve the recognition performance [Hong98, Jain02, Ross03, Chatzis99, Verlinde00, Prabhakar02, Jing07]. Multi-modal biometric fusion techniques have attracted increasing research interest in the belief that the supplementary information between different biometrics might improve the recognition performance. Hong *et al*. [Hong98] achieved improvements by integrating fingerprint and face biometric while Jain *et al.* [Jain02] combined three biometrics, face, fingerprint, and hand geometry. These topics are beyond my research scope. We only focus on the multispectral image fusion and band selection.

2.3.1 Multispectral band selection

A very desirable step when we have a large amount of multispectral information is a process to reduce this initial information without losing classification accuracy in a significant way. This reduction can be achieved by two methodologies: feature extraction [Jimenez98, Kumar01, Luis98, El-ghazawi01, Bruce02, Roweis00, Tenenbaum00, Healey99, Parkkinen88, Slater01, Jiang02, Lennon01, Du03] or feature selection [Korycinski03, Kudo00, Bruzzonne95, Sotoca04, Sotoca07, Koller96, Vidal-Naquet03, Peng05].

In feature extraction, a new and reduced data set representing the transformed initial information is obtained, whereas in feature selection a subset of relevant data from the original bands is chosen. Compared to feature extraction, feature/band selection methods identify bands which are a subset of the original spectral bands that contains most of the characteristics. Selecting a subset of relevant bands from the original set allows the process of image acquisition to be reduced to a certain number of bands instead of dealing with the whole amount of data, making simpler the image acquisition and analysis [Sotoca07].

Feature extraction embed the data into a lower dimensional space, which extract features from the original spectral band to construct a lower-dimension feature space, thereby transforming the original data onto the destination feature space through projections such as Projection Pursuit (PP) [Luis98], Principal Component Analysis (PCA) [El-ghazawi01], locally linear embedding [Roweis00], Isomap [Tenenbaum00] and subspace theory [Healey99, Parkkinen88, Slater01], wavelet transform [Jiang02, Bruce02] and Independent Component Analysis (ICA) [Lennon01, Du03]. These projections preserve most desired information but change the physical meaning of each spectral band. These methods rank the influence of each single spectral band on the new lower dimensional space. Bands with the highest influence are considered to include more information and are therefore selected [Bajcsy04, Chang99]. It is hard to decide the number of data dimension required for dimension reduction to avoid significant loss of information. In addition, the data is transformed and no longer original data. Some crucial and critical information may have been compromised and distorted.

The goal of feature selection is to minimize information loss from the information preservation point of view. Mutual information is a good candidate for feature selection as a measure of independence between random variables [Koller96, Vidal-Naquet03, Sotoca04, Peng05]. For example, Sotoca *et al.* [Sotoca04, Sotoca07] used conditional entropy as an approximation of mutual information to measure the independent information carried by one band given a sub-band set. Peng *et al.* [Peng05] argued that maximizing the relevance between each individual feature and the class, as well equivalent to the maximum dependency criterion if one feature is selected at a time. Their method needs samples from the class, as well as out of the class, to evaluate the relevance of each individual feature with the class, and is thus not applicable if no samples outside the class are available. It is basically an unsupervised feature selection criterion to obtain the relevant spectral bands from a set of sample images, minimizing the dependent information between spectral bands while maximize the conditional entropies of the selected bands [Sotoca07].

In general, the problem of subset selection using numerical techniques for model selection requires two components:

(1) An algorithm for the efficient searching of the solution space, such as greedy and genetic algorithm. Exhaustive search [Kohavi97] over the entire feature data set and branch-and-bound algorithm [Brusco03] dues of the computational costs have used rarely in analysis of high-dimension data even though they lead to an optimal solution. Heuristic search [Hill-climbing01] such as greedy climbing hill, backward elimination, forward selection, stepwise selection, is commonly used algorithms.

(2) A criterion or measure for the comparison of competing models to help guide the search. The criterion can be human perception, which is hardware dependent, participant dependent, quite subjective and also time consuming. Other criteria mentioned in literature include first or second spectral derivatives [Bajcsy04]. Entropy is interpreted as a measure of stability of each individual wavelength band in [Bajcsy04]. Low entropy values correspond to low uncertainty and thus bands with small entropy are considered good feature bands. Bassett and Shen [Bassett97] used entropy to measure the difference between different classes. Cross Entropy-Information divergence-based [Chang99], dependent information-maximize the conditional entropies at the same time minimize the mutual information [Sotoca04].

In most of work, researchers tended to consider the band selection method with the consideration of classification outputs. In [Bajcsy04], they address issue of hyperspectral band and method selection using unsupervised and supervised methods driven by classification accuracy and computational cost. Their formulation is more general by optimizing over several methods and the combinations of supervised and unsupervised methods evaluations.

One goal of band selection is to identify a reflectance feature that remains invariant when the viewing conditions change. Wang and Angelopoulou [Wang06] propose a new technique for extracting color information that is invariant to geometry and incident illumination. They examine the rate of change in reflected intensity with respect to wavelength over the visible part of the electromagnetic spectrum. For diffuse surfaces, independent of the particular model of reflectance, the only factor that contributes to variations over the wavelength is the albedo of the surface.

When there is a desired target signature vector while considering other band images as unknown signature vectors, Chang *et al.* [Chang06] proposed constrained band selection using the concept of constrained energy minimization to linearly constrain a band image.

In multispectral and hyperspectral remote sensing problems, the observed value is just a vector of gray levels at specific wavelengths of the sensor spectrum. During the past forty years, various algorithms were introduced for classification of multispectral data in a pixel-wise manner [Shaw02, Landgrebe02, Landgrebe03, Farag02]. These algorithms, exploit the fact that each class of materials has its own spectral signature which is related to their molecular compositions. Using the above facts, spectral signature of certain material enables spatial classification for vegetation investigation, cancer or tumor detection and other applications.

2.3.2 Multispectral data fusion

In the past, various techniques for fusion of multispectral images have been proposed. A standard technique is to fuse three component images into a color image. Transformation to other color spaces can then be applied [Carper90, Shettigara92]. Similar techniques have been applied in medical images [Alfano95]. Extension of these ideas is based on linear projection techniques as principal component analysis and projection pursuit [Harikumar92]. Using multi-resolution techniques, the information of the component images is fused at different resolutions. Laplacian pyramids [Toet90] as well as wavelets [Yocky95, Li95] were applied. Kohonen's Self-organizing Maps (SOM) [Kohonen95] was also proposed. Mappings can be applied globally as papers mentioned above and can also be spatially locally mapped [Scheunders00] to improve local contrast.

In multispectral imaging, the most common fused image fusion is applied to spatially co-register panchromatic (PAN) and multispectral images, especially on modern earth resource satellites images. Due to high spatial resolution and low spectral resolution of PAN image, and low spatial resolution and high spectral resolution of MS image, image fusion aims at combining these two kinds of images to form new images for improving the performances of the fused images in information content, resolution, and reliability of registration and interpretation [Ma06].

There have been many fusion algorithms for this purpose, among which the most popular ones are based on PCA [Chavez89], HPF [Chavez90], and IHS transforms [Carper90, Wang05, Sadjadi05, Gonzalez-Audicana04, Pohl98]. In these algorithms, the low-resolution images need to be interpolated to the size of panchromatic one, and the features of low resolution images should be correctly matched to those of high resolution panchromatic image. More specifically, in the PCA based method, the MSIs are first interpolated to the size of panchromatic image, and then the first PCA components of MSIs are replaced by that of panchromatic image. In the case of IHS based method, the IHS transform is applied to each MSI and the Intensity component of the MSIs are replaced by that of panchromatic image. In Wavelet based fusion algorithm, the panchromatic and interpolated MSI images are wavelet-transformed, and the images are matched and fused using the low-pass band information. Those methods distort the spectral characteristics of the multispectral data. Wavelet-based approaches [Civco89, Garguet-Duport96, Li95, Luo92, Yocky96] are spectrum-preserving image fusion using multi-resolution wavelet transform to fuse multispectral images and high-resolution images. [Tseng01] proposed integer wavelet transform and principal component analysis to fuse low-resolution Landsat TM multispectral images and a panchromatic image to generate high-resolution multispectral images. In the serial work of Krueger [Krueger99, Krueger00], a tracking scheme based on the wavelet subspace is presented. The wavelet subspace is a vector space spanned by a set of wavelets. [Garzelli04] reviews for multispectral and panchromatic image fusion based on either intensity-hue-saturation transformation, or redundant multi-resolution analysis. In either case, lower-resolution MS bands are sharpened by injecting details taken from the higher-resolution Pan image.

Multispectral image data often present complementary information about investigated region so that image fusion provides an effective method to enable comparison and analysis of such data. In other words, the joint processing of multispectral bands serves to enhance details that are unique to a certain band by reducing the relative contribution of the common component of the different bands. The different bands of multispectral images are generally correlated because the bands represent different aspects of the same underlying physical scene. Therefore, wavelet fusion can be applied on different bands and achieve a fused image with enhanced information [Scheunders00]. [Scheunders01] introduced a wavelet representation for sub-spectral images, and average the low resolutions image of the original bands. The fused grey-level image contains the fused edge information of the different bands.

In face recognition, image fusion happens when infrared face images are combined with visible images because the face images captured using thermal infrared sensors is nearly invariant to changes in ambient illumination [Socolinsky01, Bebis06, Kong05, Kong07].

3 Multispectral imaging system

The requirements for robust face recognition systems are extensive in a practical world with pressing issues in identity authentication and recognition. In spite of the diversity of techniques and face recognition tools designed, evaluated and tested, face recognition is not robust enough to under illumination changes. Most of the promising methods use conventional cameras with a broad-band sensor response. However, very few researchers have exploited multispectral imaging and images to improve face recognition even though multispectral imaging has been used in many research area and applications. One of the main obstacles to implementation of multispectral images in face recognition is that most of the multispectral imaging tools are specified and customized and very expensive. Hence, a multispectral face database which can be used for verification of our theory is hardly available. Especially there is not one multispectral face database in visible spectrum over daylight.

Multispectral images are typically acquired by specialized systems. In recent years, modern spectral image capture systems tend to rely on combinations of CCD cameras with various types of narrow or broad band filters. The images are then processed using normal high-capacity computational machinery with software developed to properly treat the spectral data. With the advances in filter technology, using a variety of electronically tunable filters that are mounted in front of a monochrome camera to produce a stack of images at a sequence of wavelengths can form a image cube. The combined spectral/spatial analysis offered by such image cubes takes advantage of tools borrowed from spatial image processing, specific spectroscopy, and new custom exploitation tools developed specifically for these applications.

Our ultimate goal is to investigate the benefits of utilizing multispectral images over the existing conventional broad-band images. Therefore, a multispectral imaging system in visible spectrum needs to be designed and the corresponding spectral images to be collected. The system setup of the mobile multispectral imaging system is described in section 3.1. Section 3.2 discusses the design of various light sources corresponding to the physics characteristics of the liquid crystal tunable filter. The first multispectral face database in visible spectrum is described in section 3.3. Finally, we summarize our data acquisition in section 3.4.

3.1 System setups

Our imaging system is unique in two aspects. (1) There are three different imaging modalities on one translation platform to acquire well-aligned face image data in a short duration. This allows the participants to maintain their expression and pose during acquisition. (2) It is the first multispectral imaging system used to acquire a relatively large database of people under different illuminations in the visible spectrum. In this section, the hardware and software components are described in section 3.1.1 and 3.1.2.

3.1.1 Hardware components

The multimodal imaging system is mounted on a mobile platform shown in Figure 3.1. The mobile imaging system was integrated on one translational platform to acquire well-aligned face images in a short duration of time, which allows the participants to maintain their expression and pose. The cameras were mounted on an optical breadboard (24 × 6 inches) and arranged on machined bases such that there was no pitch, yaw or roll inconsistencies between them. The optical breadboard is mounted on a heavy aluminum 80-20 slide base that allows the cameras to displace with almost no mechanical vibrations. The operator slides the camera to the desired position and switches between the cameras using video source selector. An onboard computer and monitor are used to interface with the cameras and the live feed.

The lateral view of the multimodal imaging system is shown in Figure 3.2 (a), which consists of multispectral imaging components, a thermal camera and a RGB color camera. The multispectral imaging components are shown in Figure 3.2 (b). Instead of using the turning wheel in our image acquisition, a liquid crystal tunable filter (LCTF) in visible spectrum which can provide narrow band filters at different wavelengths between 400nm and 720nm is used. The multispectral module consists of a monochrome camera coupled with an electronically tuned LCTF. The LCTF from Cambridge Research Institute (CRI) provides narrowband filters with a full width-at-half-maximum bandwidth of 7nm. The aperture of the LCTF is 35mm and field of view is $\pm 7^{\circ}$. A maximum of 321 narrow-band MSIs can be acquired by continuously tuning the LCTF. A wide angle lens is mounted on the monochrome camera (Sony XC-75) and this is coupled with the LCTF through a hardware interconnection. The camera auto-gain is set to 0 dB in order to acquire raw data. The black current of Sony XC-75 is measured by covering the lens and read the pixel values of black images. After averaging, the typical black current is 4 or 5 out of 256.

A Raytheon Palm-IR-Pro® infrared camera is used for thermal data acquisition. A digital visible RGB camera (Canon PowerShot A80) is used to acquire the RGB images in daylight and indoor fluorescent lighting conditions.

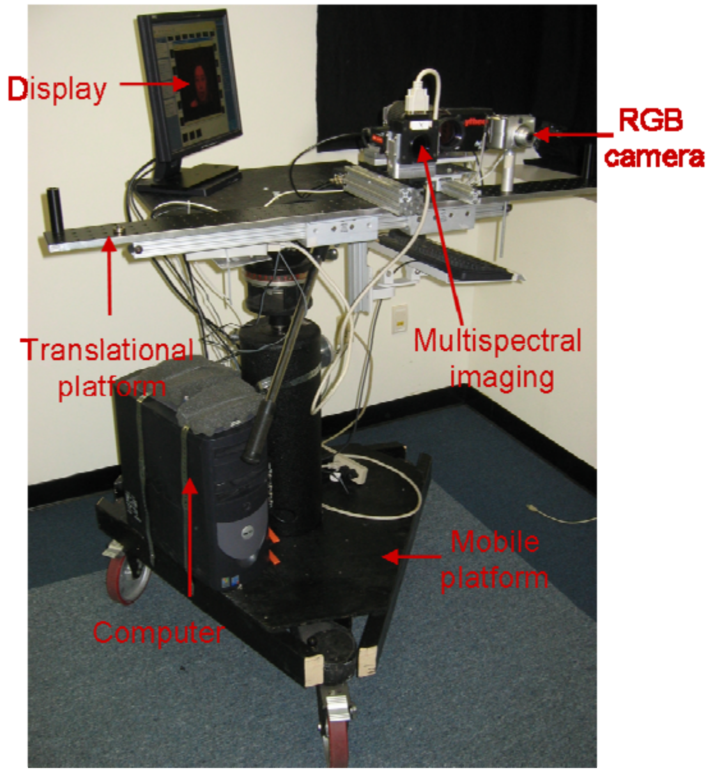

Figure 3.1. The all-inclusive multimodal and multispectral mobile imaging system for indoor and outdoor face data acquisition.

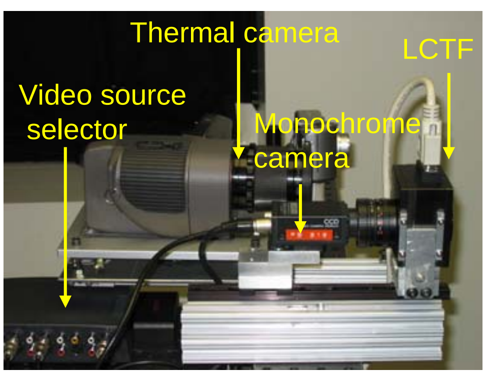

(a) (b)

Figure 3.2. (a) The lateral view of the multimodal imaging system. (b) Multispectral imaging components.

A Matrox Meteor-II frame grabber is employed to capture the analog video signals from the Sony XC-75 and the thermal camera. Software tunes the desired wavelength of the band and captures the corresponding narrow band image via the frame grabber. A video source selector was used to reduce the hardware switching time between Sony XC-75 and the thermal camera.

During our database acquisition, we characterized the illumination by using a light meter and a spectrometer. The EasyView30 light meter is used to measure the illuminance and the Ocean Optics USB2000 Spectrometer is used to measure the irradiance of the illuminant. These tools are shown in Figure 3.3. The equipment involved in our imaging system is tabulated in Table 3.1.

3.1.2 Software development

A functional, user friendly, completely automated graphical software package was developed to interface between the cameras, the LCTF and the data acquisition. The software governs the sweeping of the filter and synchronization of the frame grabber with the filtering sequence, while providing a graphical user interface (GUI). The GUI has the functional blocks such as filter detection, tuning/sweeping and storing images. The act of saving the MSIs is synchronized with the filter centering at the corresponding wavelength. Figure 3.4 shows the entire GUI with the live feed video display and the control panel.

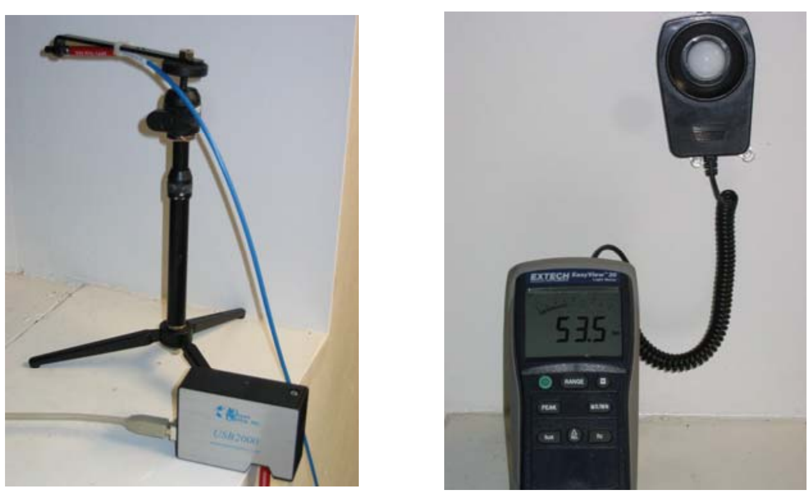

(a) (b)

Figure 3.3. Spectrometer and light meter used in our image acquisition, (a) Ocean Optics USB2000 Spectrometer and (b) EasyView30 light meter.

Table 3.1. Equipment used in the multimodal imaging system.

Equipment	Brand name
Monochrome camera	Sony XC-75
Lens	Fuji 16mm
LCTF	CRI's VariSpec Tunable filter 0.4 -0.72 µm.
Thermal camera	Raytheon Palm-IR-Pro®
Digital RGB camera	Canon Powershot A80
Frame grabber	Matrox Meteor-II
Video source selector	RCA VH915
Spectrometer	Ocean Optics USB2000
Light meter	EasyView30

Figure 3.4 shows the entire GUI with the live feed video display and the control panel. We use visual aids displayed on the GUI, by means of red bounding boxes and a centering blue line to assist the operator in centering the face region to the preferred scale and size. The visual aids are displayed only on the GUI as an image reference and do not feature in the image database. The visual aids help mainly with the registration of the various modalities. The images acquired using the designed setups are well-aligned except for minor exclusions in scale and translation. To reduce the effects of these minor exclusions, we developed a user-interactive affine transform registration tool, which uses separate registration.

3.2 Lighting engineering

Based on the physics characteristics of our imaging system, several light sources are designed and assembled for data acquisition which is described in section 3.2.1. Additional filters for illumination compensation are tested in section 3.2.2.

3.2.1 Light source design

Light sources play an important role in the image acquisition and affect the corresponding multispectral image intensity levels. Considering the transmittance characteristics of LCTF shown in Figure 3.5 (a), the ideal light source in theory should have a power distribution as shown by the blue line in Figure 3.5 (b). The light intensity or illuminance should be around 10 to 15Klux according to my experiments.

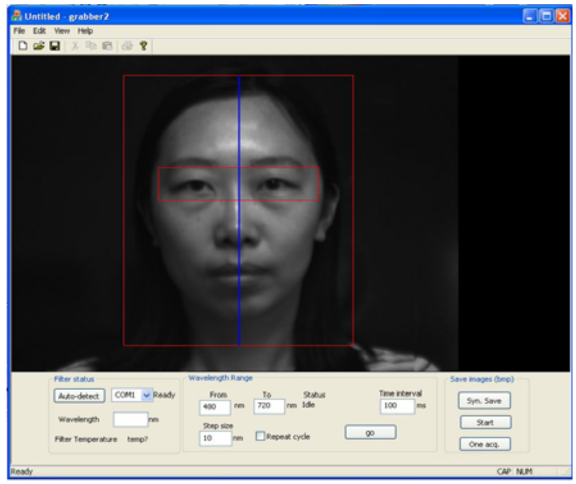

Figure 3.4. Graphical user interface of the software developed to synchronize the tuning of the LCTF with the frame acquisition process.

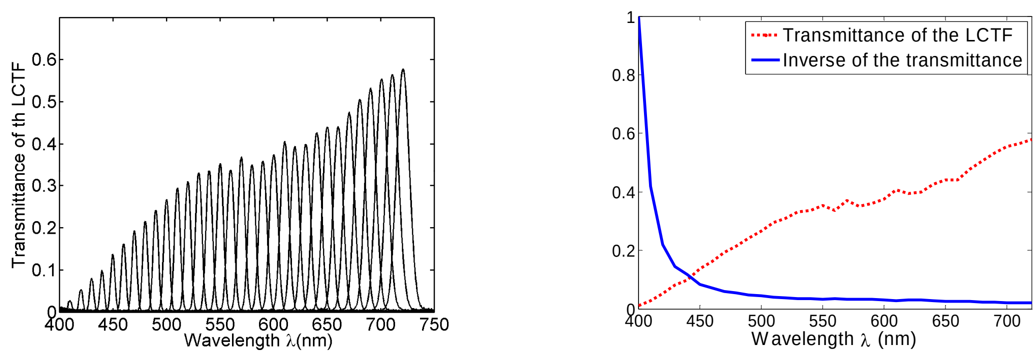

(a) (b)

Figure 3.5. (a) The narrow-band transmittances of the LCTF from 400nm to 720nm with the increment of 10nm. (b) The ideal spectral distribution of a light source which can completely compensate the transmittance of the filter (red line) is indicated by the blue line.

Every light source has its unique spectral power distribution and intensity. Our selection of light sources is based on the most common used light sources. We have assembled more than 10 arrays of light sources. Some illumination setups used for our data acquisition are shown in Figure 3.6. The quadruple halogen lights with a pair on each side of the participant are shown in Figure 3.6(a). The second illumination setup was a pair of fluorescent light panels shown in Figure 3.6(b). It is assumed that the indoor illuminants, halogen light and fluorescent light, are homogenously distributed on the face.

The face data was acquired in day light with side illumination, meaning that the participants were not directly facing the sun. This was due to the fact that many participants were unable to maintain pose or expression with bright sunlight and wind streaming directly into the eyes. In Figure 3.6(c), an example of the outdoor side illumination is shown.

The spectral power distributions (SPDs) of different illuminants are shown in Figure 3.7. The SPD of halogen light (a) is very smooth and the peak is at the orange part of the spectrum. The SPD of the fluorescent light panel (b) is spiky at certain wavelengths. The day light (Figure 3.7 (c)) tends to have more green and blue color compared to the other two illuminants. The SPD of another fluorescent light has some spikes at different wavelengths (Figure3.7 (d)). The information contained in the spectral distribution is incorporated into our proof of concept tests, for illumination adjustment, to improve the face recognition rate.

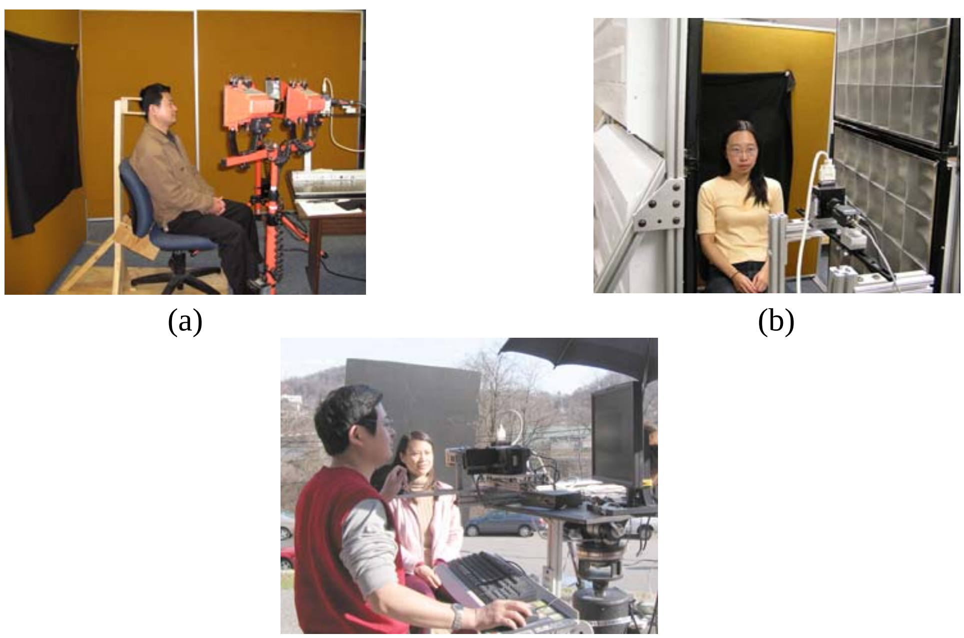

(a) (b)

(c)

Figure 3.6. Three illumination setups, (a) quadruple halogen lights with a pair on each side halogen lighting setup, (b) a pair of fluorescent light panels, and (c) daylight with side illumination.

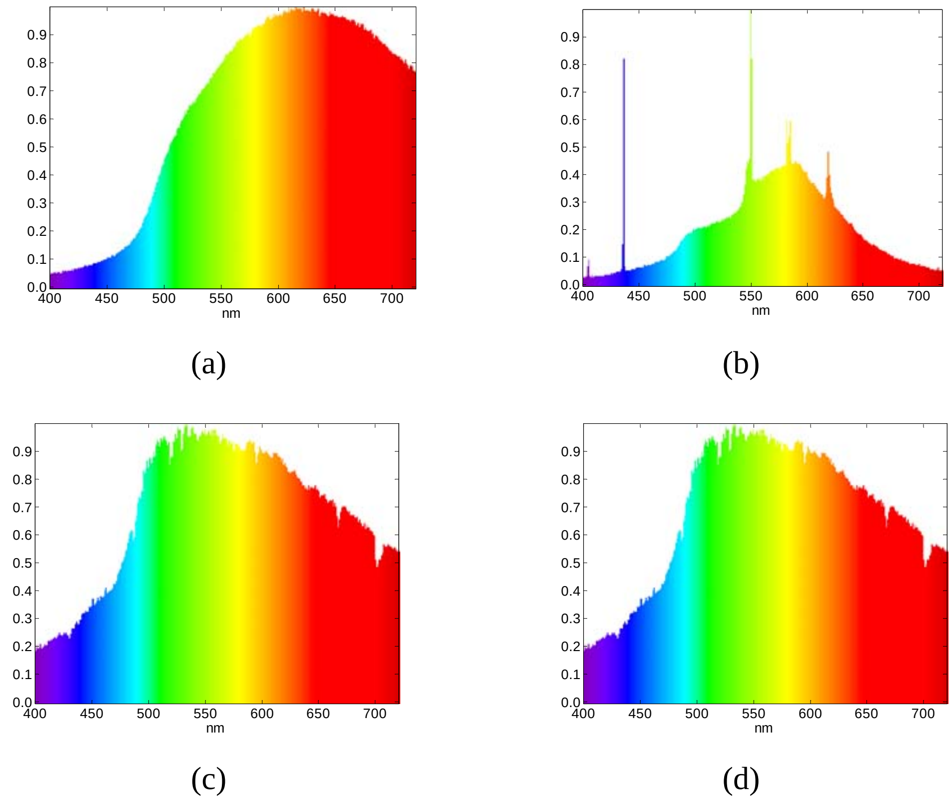

Figure 3.7. Normalized spectral power distribution of (a) halogen light (b) fluorescent light, (c) day light, and (d) another fluorescent light.

3.2.2 Additional filters

From engineering point of view, additional filter is a good choice with constrains of the existing illuminant. Therefore, we tested the Cokin creative filters A 375 shown in Figure 3.8 in front of the LCTF with 20 different color filters which have different spectral transmittance each. However, these additional filters reduce the illuminance dramatically which leads to more intensive light source and cause the participants blinking. Therefore, it is not practical to utilize filters right in front of the LCTF.

The other possible solution of using additional filter is to insert one between the light source and the subject. There are several choices, such as transparent fabrics, gelatins, painted glass and programmable filters. For research purpose, a programmable filter is the optimal solution. Therefore, a tunable liquid crystal display (LCD) filter was built from the 19” widescreen X191WSD from Acer with the contrast ratio of 800:1 and resolution of 1440x900. The tunable filter is shown in Figure 3.9(a) and the measurement of the transmittance of the tunable filter is shown in Figure 3.9 (b). A user friendly graphic user interface shown in 3.10 is developed to control the spectral of the filter.

(a)

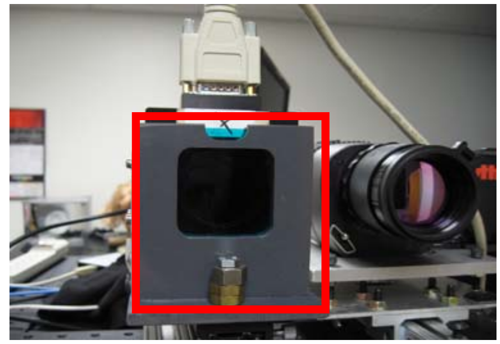

(b)

Figure 3.8. (a) Cokin creative filter A 375. (b) One filter is mounted in front of our multispectral imaging system. The red line indicates the position of the filter.

(a)

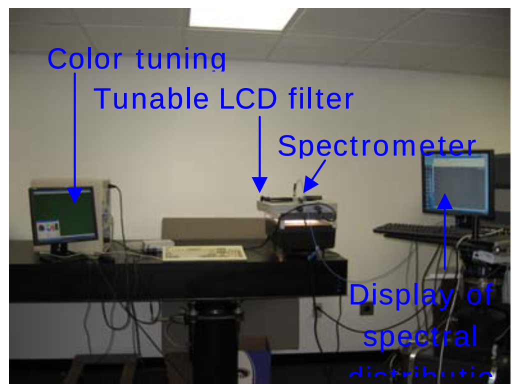

(b)

Figure 3.9. (a) Tunable LCD filter (b) the setup of the measurement of the transmittance of the filter.

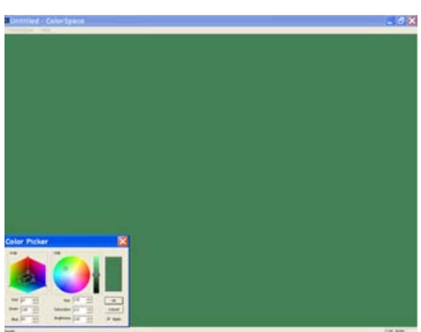

(a)

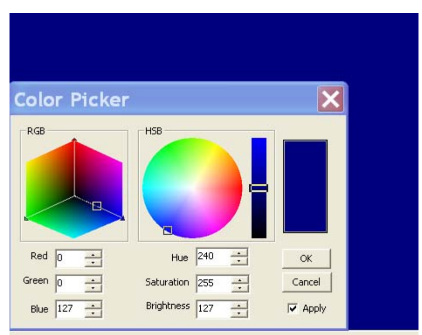

(b)

Figure 3.10. (a) Screen cut of the interface of the GUI. (b) Enlarged spectral tunable control panel.

The measured tunable spectral transmittance is shown in Figure 3.11. The measurement is conducted for the change of hue values while saturation value of 255 and brightness of 127 are fixed. As it is noted that the spectral transmittance around green wavelength has a peak while the hue value is tuned to green color zone. The same pattern works for red color. It is proved that the tunable LCD filter works correctly for the spectral tuning purpose.

The transmittance of the LCTF transformed to CIEXYZ space is

$$XYZ = \begin{bmatrix} 0.33 & 0.32 & 0.16 \end{bmatrix}, \tag{3.1}$$

and the corresponding RGB value under D65 day light is

$$\begin{aligned} &\mathrm{RGB} = [0.498 \quad 0.287 \quad 0.122] \text{ in the range of } [0 \quad 1] \\ &\mathrm{RGB} = [127 \quad 73 \quad 31] \text{ in the range of } [0 \quad 255] \end{aligned} \; . \tag{3.2}$$

Therefore, the inverse of the transmittance can also be calculated into XYZ and RGB value which are

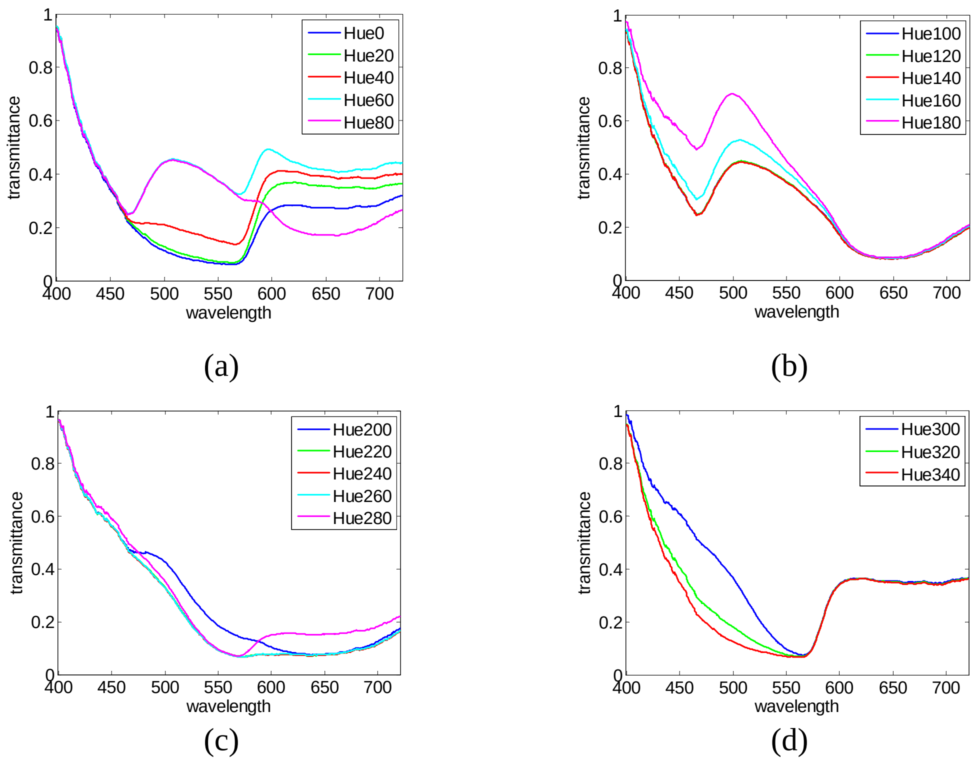

Figure 3.11.The spectral transmittance of the tunable LCD filter with different hue values and fixed value of saturation 255 and brightness 127.

$$\begin{aligned}&CIEXYZ=[0.52\ 0.53\ 0.94]\\&RGB=[114\ \ 121\ \ 235]\end{aligned}\quad . \tag{3.3}$$

The percentage of light intensity that can pass through the filter varies according to the tuned spectrum. For example, when it is completely white, or RGB=[255 255 255], 5.79% of the light can pass through. When the color is tunable to completely compensating the LCTF which is the results of equation (3.3), 1.84% of the light can pass through the filter. Therefore, in order to utilize this filter, a much more intensive light source is needed. According to experiments, 100Klux or higher is needed. The metal halide which provides as strong as 300Klux is built for testing. The spectral distributions measured with the LCD filter and without the filter are shown in Figure 3.12. The spectrum with the filter has less intensity in red color zone which is the effect of the filter of suppressing the trespass of the red.

3.3 Multispectral face database

The multispectral face database has noteworthy characteristics. This is the first database with registered images in the visible, multispectral and thermal modalities, coupled with spectral distributions of the illumination sources used during acquisition. Participants were imaged under various illumination conditions such as with halogen light, fluorescent light and day light. Another interesting fact is the large amount of multispectral bands available in our database. Previous databases [Rosen99] have provided 16 bands per participant and a total of 7 people, while our database has 25 bands per participant and totally 82 participants.

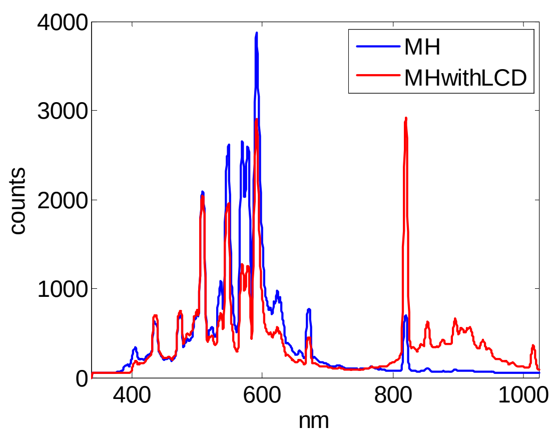

Figure 3.12. Spectral distribution comparison with and without the filter in front of the metal halide light.

Narrow-band multispectral face images in the near infrared spectrum have been collected for face recognition [Pan03]. However, these narrow-band spectral images cannot be compared to the existing system or recognition performance.

The participation in this study was fully voluntary. Male and female participants from various ethnicities and ages were involved. The participants were asked to be seated in the mobile seating platform at 1.2 meters from the camera setup. The participants were asked to rest their heads on the head rest and stay relaxed with a neutral expression. Once the participants acclimatized to this setting, the image acquisition was performed. The demographics and hardware settings were encoded in the file name using a standard coding procedure.

The imaging procedure had to be sufficiently fast to image a non-rigid participant. Based on the ability of the participant to withstand the glare from the sun, we decided to use a 10nm increment in the outdoor data acquisition while tuning from 480 to 720nm. This allowed the acquisition of 25 MSIs in less than 10 seconds. The aperture of the lens was controlled based on the radiance of the illuminant.

We acquired the thermal, MSIs and visible images of faces under various illuminations. The image resolution of thermal and MSIs is 640×480 pixels. The outdoor visible RGB images also have a resolution of 640×480 pixels. The visible RGB images under fluorescent-2 have high resolution, 2272×1704 pixels. The details about the physical size of the database are shown in Table 3.2 and the total size of the uncompressed database is 8.91GB.

The database was collected in 10 sessions between August 2005 and March 2006. There is a total number of 82 participants of different ethnicities, ages, facial hair characteristics and genders in our database. Figure 3.13 shows the demographics of the 82 participants in our database. The database is made up of 76% male and 24% female; the ethnic diversity is defined as a collection of 57% Caucasian, 23% Asian (Chinese, Japanese, Korean and similar ethnicity), 12% Asian Indian and 8% African Descent. Some examples, shown in Figure 3.14, demonstrate the demographic diversity of our database.

In Figure 3.15, we show one data record in our database. The color image acquired under fluorescent-2 is shown in (a) and the outdoor color image is shown in (h). The thermal image acquired with the Raytheon Palm-IR Pro® is shown in (b). The MSIs are shown in (d)-(h), with the wavelength centered at 0.48 μm, 0.54 μm, 0.60 μm, 0.66 μm and 0.72 μm.

Figure 3.16 gives an image sequence under halogen light with each gray level image colored indicating the exact color corresponding to the wavelength at which the image is acquired. Figure 3.17 give another image sequence under daylight with color indication of the corresponding wavelength.

Table 3.2. Physical size of database on disk.

Image/Video Type	Physical Size on Disk
Halogen light database	4.65GB
Fluorescent-1 database	2.27GB
Daylight database	1.73GB
Thermal database	0.078GB
Fluorescent-2 database	0.084GB
Total size on disk	8.91GB

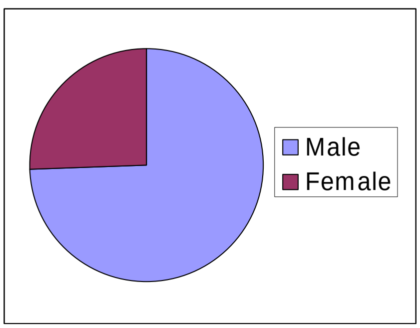

(a)

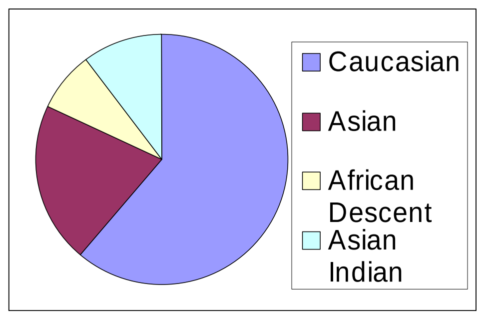

(b)

Figure 3.13. Demographics of participants. Pie chart of (a) male (lilac)/female(maroon) participants and, (b) the different ethnicities such as Caucasian (lilac), Asian (maroon), African descent (yellow) and Asian Indian (light blue) in our database.

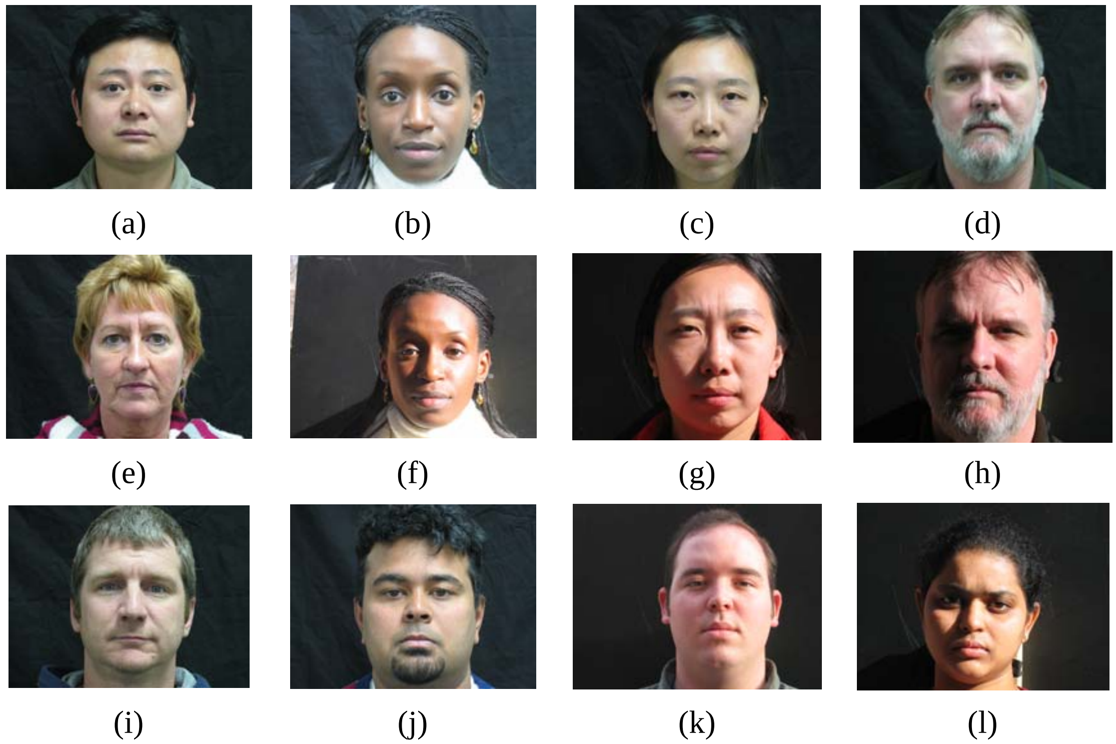

Figure 3.14. Examples of 12 participants, (a) male Asian under fluorescent light, (b) female African descent under fluorescent light, (c) female Asian under fluorescent light, (d) male Caucasian under fluorescent light, (e) female Caucasian under fluorescent light, (f) female African descent under daylight, (g) female Asian under daylight, (h) male Caucasian under daylight, (i) male Caucasian under halogen light, (j) male Asian Indian under fluorescent light, (k) male Caucasian under daylight, and (l) female Asian Indian under daylight.

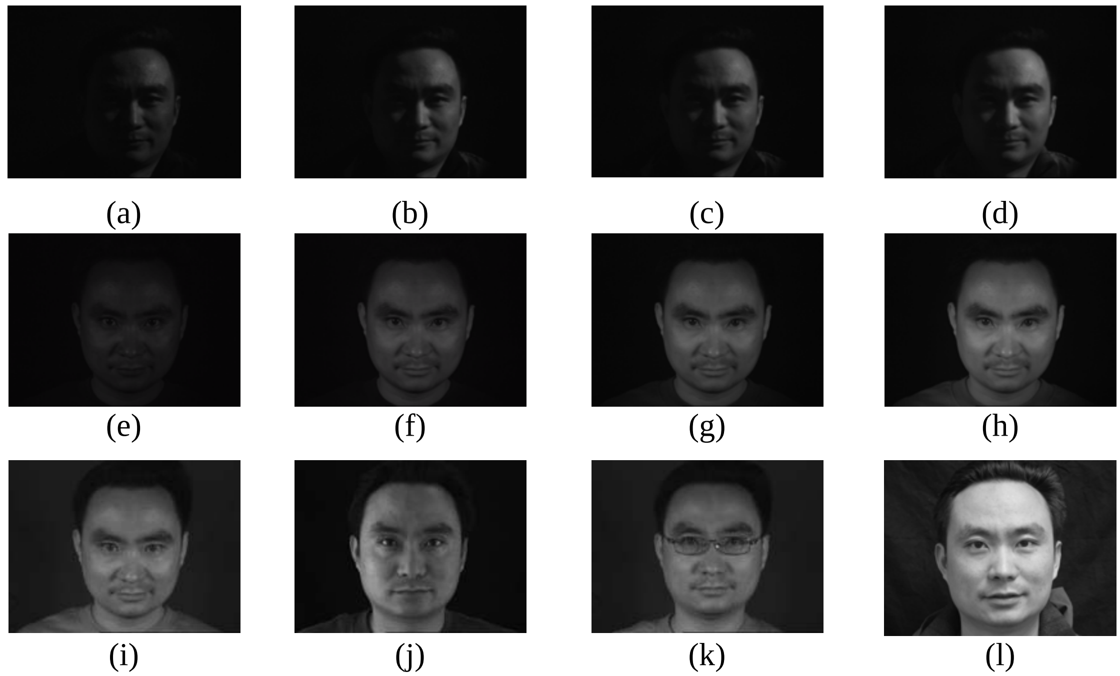

Figure 3.15. Sample images in a data record in the IRIS-M^3 database; spectral image under indoor halogen light at (a) band 580nm, (b) band 620nm, (c) band 660nm, and (d) band 700nm. Spectral image under daylight, side illumination at (e) band 580nm, (f) band 620nm, (g) band 660nm, and (h) band 700nm. Conventional broad-band image (i) under halogen light, (j) slightly fluorescent light, (k) under another fluorescent light, and (l) under daylight.

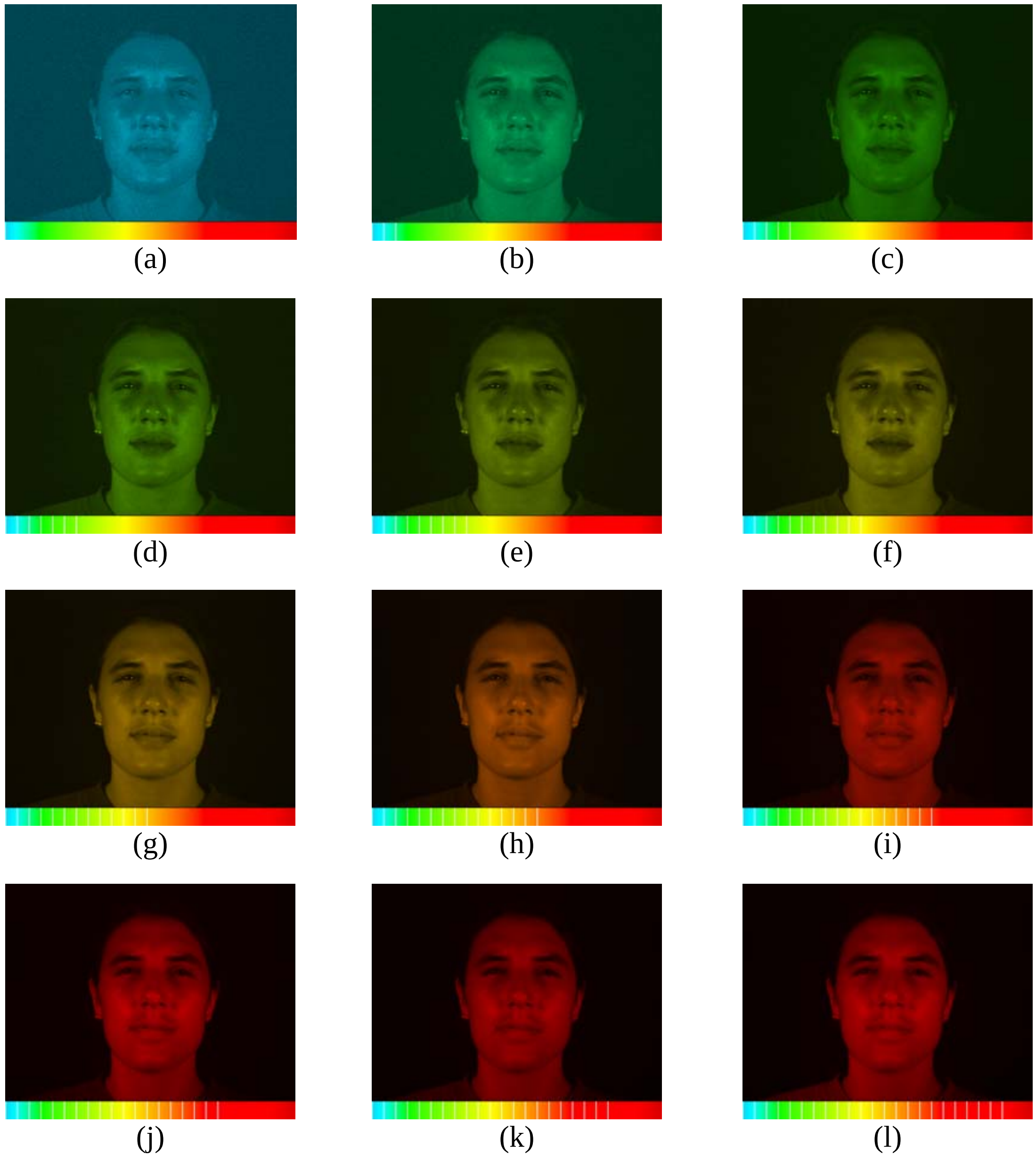

Figure 3.16. An image sequence of one subject under halogen light with each gray level image colored indicating the exact color corresponding to the wavelength at which the image is acquired, (a) 480nm, (b) 500nm, (c) 520nm, (d) 540nm, (e) 560nm, (f) 580nm, (g) 600nm, (h) 620nm, (i) 640nm, (j) 660nm, (k) 680nm, and (l) 700nm.

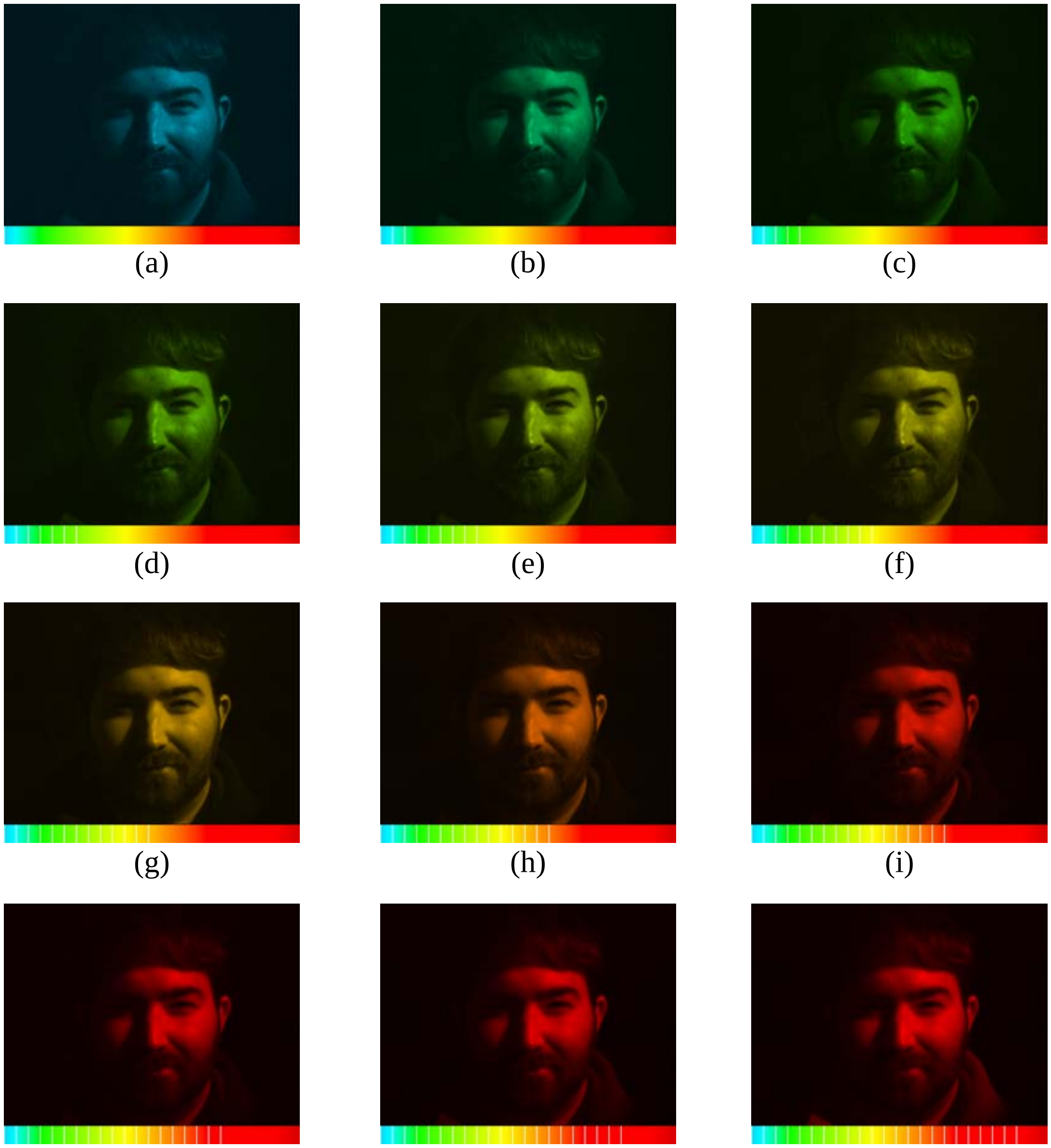

(a) (b) (c) (d) (e) (f) (g) (h) (i) (j) (k) (l)

Figure 3.17. An image sequence of one subject under daylight with each gray level image colored indicating the exact color corresponding to the wavelength at which the image is acquired, (a) 480nm, (b) 500nm, (c) 520nm, (d) 540nm, (e) 560nm, (f) 580nm, (g) 600nm, (h) 620nm, (i) 640nm, (j) 660nm, (k) 680nm, and (l) 700nm.

3.4 Summary

In this chapter, I described the solid foundation of my dissertation work, the successful development of the unique multispectral imaging system so that the spectral narrow-band images can be collected for our theory verification. The hardware of the imaging system includes mainly a video camera, and a liquid crystal tunable filter and a frame grabber. The developed software controls the filters and synchronization for acquisition process. The third effort in the imaging system design is the light source design for different illumination acquisition.

In addition, multiple testing of the components and the whole system was required for acquisition constrains, such as the illuminance changes, aperture tuning, and acquisition time testing. For example, each acquisition time of one face is constrained since faces are non-rigid objects. To ensure registration between bands, we found that the configuration of the acquisition time of less than 10 seconds and 25 bands from 480nm to 720nm, with the increment of 10nm, is a practical solution.

The mobile imaging system is designed and built for the convenience of both indoor and outdoor data acquisition. In the span of one year, we collected the IRIS-M^3 face database which has certain significant characteristics. This is a unique database with registered images in the visible, multispectral and thermal modalities, integrated with spectral distributions of the illuminants employed in acquisition. Eighty-two participants in our database are of different ethnicities, age groups, facial hair characteristics and genders.

4 Multispectral image fusion

To illustrate the advantage of using and fusing MSIs for face recognition, a comparison of multispectral images and conventional images needs to be conducted. At the same time, every advanced accessible recognition engine was developed in the way that the smallest input unit is a two dimensional image. Therefore, conventional two dimensional images can be evaluated directly by these engines. However, the multiple spectral images with three-dimension information can not be the direct input to the engine. Therefore, image fusion on spectral images is necessary and required because it is required for both spectral images and conventional images to be tested by the same recognition engine for a reasonable performance comparison. In a word, the fusion of multispectral images is conducted for the dimension reduction of spectral images so that they can be tested by the existing engines.

After the acquisition of spectral narrow-band images and conventional broad-band images, novel image fusion algorithms are proposed and implemented on spectral images. Physics-based weighted fusion is proposed inspired by the multispectral image acquisition process. From physics point of view, the information of the spectral response of the camera, transmittance of the liquid crystal tunable filter, spectral reflectance of an object and the spectral distribution of the acquisition lighting condition, can be used as weights on different sub-spectral images for fusion. Illumination adjustment algorithm makes use of the ratio between two illuminations, one for probe images and the other for gallery images. A wavelet fusion and decision level fusion are also proposed for comparison. The results of proposed fusion algorithms show improved face recognition performance compared to conventional broad-band images, which provide better face recognition results with up to 78% improvement on conventional visible images under day light.

The remainder of this chapter is organized as follows. Section 4.1 gives the details of the physics-based weighted fusion. Section 4.2 describes illumination adjustment algorithm. Wavelet fusion and rank-based decision level fusion are discussed in section 4.3 and section 4.4. Experimental results are given in section 4.5. Summary is given in section 4.6.

4.1 Physics-based weighted fusion

There are two advantages of multispectral images over conventional images that we took into consideration as our inspiration of utilizing multispectral images for face recognition. First, it is well known that we humans tend to spot easily any color changes in the skin tones. The main obstacle for universal color use in machine vision applications is that the cameras are not able to distinguish changes of surface color from color shifts caused by varying illumination [Li04]. Multispectral images in visible domain can provide a new avenue to separate the color of a subject and the illumination. Secondly, with multispectral images, we have the freedom to emphasize and/or suppress the contribution of images from certain narrow bands. Contrarily, conventional monochromatic and RGB images provide only one- or three-broad-band responses. The spectral sensor responses of a conventional monochromatic camera, a conventional RGB color camera, and a multispectral imaging system are shown in Figures 5(a), (b) and (c), respectively.

The spectral response function of a sensor defines the probability of a photon of a given wavelength being detected by a sensor. The spectral response p_k (x, y) of a conventional monochromatic camera sensor in a certain wavelength range, $\lambda_{\min}$ to $\lambda_{\max}$, can be represented as

$$p(x,y) = \int_{\lambda_{\min}}^{\lambda_{\max}} R(x,y,\lambda)L(x,y,\lambda)S(x,y,\lambda)d\lambda\,, \tag{4.1}$$

The parameters (x, y) indicate the pixel location in the image. R(x, y, λ) is the spectral reflectance of an object, L(x, y, λ) is the spectral distribution of the illumination, and S (x, y, λ) is the spectral response of the camera. The entire possible integration wavelength range can be in the visible spectrum, 400nm to 720nm or even include the infrared spectrum depending on the camera design. To simplify our analysis, (x, y) can be omitted for we assume that the illumination is homogenously distributed over the entire face. In other words, these parameters are constant in the spatial domain for each image. However, conventional monochromatic cameras have difficulties in utilizing this information because spectral power distributions of most light sources have high-dimensional information. On the other hand, multispectral imaging systems can make use of this high dimensional information.

In a multispectral imaging system as shown in Figure 4.2, there are four main factors that determine the intensity values of each sub-spectral image, spectral reflectance of a subject $R(\lambda)$, spectral distribution of the illumination $L(\lambda)$, spectral response of the camera $S(\lambda)$ and the new parameter, comparing to equation 1, the transmittance of the liquid crystal tunable filter $T(\lambda)$. The incident light $L(\lambda)$ is first reflected by the surface of an object. The reflected light $R(\lambda)L(\lambda)$ passes through the LCTF and lens.

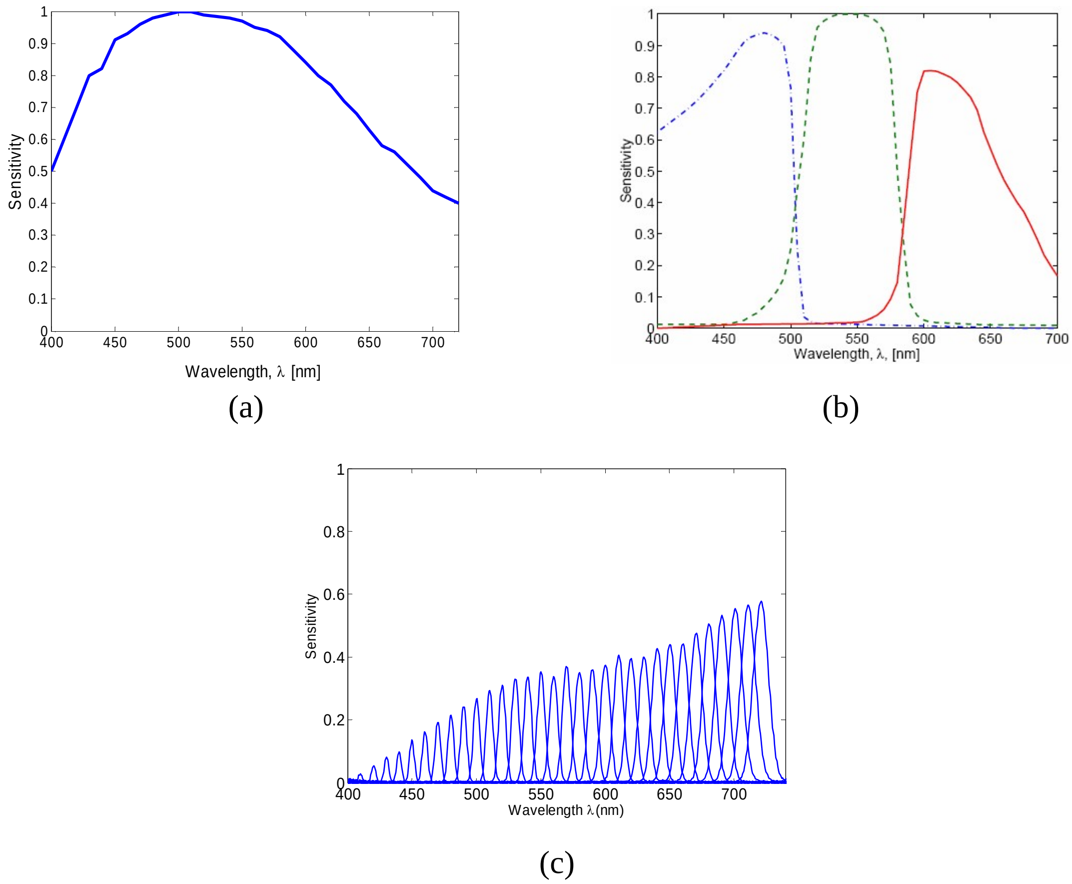

Figure 4.1. The spectral sensor response of (a) a monochromatic imaging system, (b) RGB color camera, and (c) a multispectral imaging system.

The photons get to the CCD chip and hence, the spectral sensor response is created. Therefore, the camera response p_{λ_k} corresponding to band k centered at wavelength λ_k , can be obtained by:

$$p_{\lambda_k} = \int_{\lambda_{k,\min}}^{\lambda_{k,\max}} p(\lambda)d\lambda = \int_{\lambda_{k,\min}}^{\lambda_{k,\max}} R(\lambda)L(\lambda)S(\lambda)T(\lambda)d\lambda \text{ with } k = 1,2,\ldots N_B, \qquad (4.2)$$

where N_B is the total number of spectral bands. Therefore, the camera response is the result of an integration process which can also be calculated in a discrete form as the summation of samples. Because each spectral image is acquired within a very narrow band, we only use one sample of each factor per band. Therefore, the sensor output at wavelength λ_k can be represented as

$$p_{\lambda_k} = R_{\lambda_k} L_{\lambda_k} S_{\lambda_k} T_{\lambda_k} . \qquad (4.3)$$

T_{λ_k} is the spectral transmittance of the LCTF. With the physics limitations of the imaging system, such as the lower transmittance at the lower wavelengths in the LCTF, which was shown in Chapter 3, our multispectral images have different intensity distributions at different wavelengths. Assuming the three factors, *R*, *L*, and *S*, in (3) are uniformly distributed in the spectrum, we can predict that the spectral images would appear to be darker at the shorter wavelengths than the images at the longer wavelengths

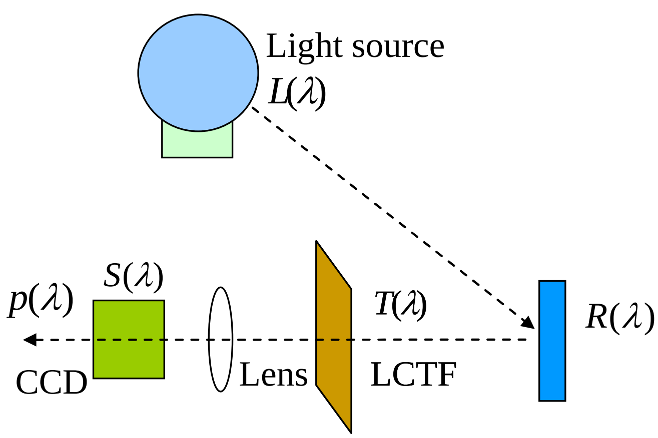

Figure 4.2. The camera response $p(\lambda)$ is the result of integration of all the factors involved, including the spectral distribution of the illumination $L(\lambda)$, reflectance of the subject $R(\lambda)$, the transmittance of LCTF $T(\lambda)$ and the spectral response of the camera $S(\lambda)$.

because of the LCTF's transmittance differences. In practice, each of the factors has a non-uniform distribution across the spectrum. An example of the normalized skin reflectance is shown in Figure 4.3 (a). A monochromatic CCD sensor response and the transmittance of a liquid crystal tunable filter are given in Figure 4.1 (b). Those two factors are the same for different skin color as long as the same imaging equipment is used for data acquisition. The combined spectral characteristics of these three factors, skin reflectance, sensor response, and the transmittance of the LCTF, are plotted in Figure 4.3 (b). The physics information is utilized as weights for the multispectral image fusion and the information includes the transmittance of the LCTF, spectral power distribution of light sources, sensor's spectral response and skin reflectance.

4.2 Illumination adjustment

In physics-based weighted fusion, the weights can be the ratio of the spectral distribution of two different light sources. We call this specific weighted fusion, illumination adjustment since by using this ratio, we can adjust one image acquired under illumination-1 to appear like the image acquired under illumination-2. The details are explained as follows.

We learn that the skin reflectance are smooth and similar, the main difference is in the level not the shape in spectrum [Imai96, Nakai98]. The natural reason for the closeness of skin reflectance is that the skin color appearance for all ethnic groups is formed from three colorants: melanin, carotene, and hemoglobin [Edwards39]. Therefore, it is hard to use the skin reflectance shape for recognition [Martinkauppi02]. An example of the normalized skin reflectance is shown in Figure 4.3 (a). A monochromatic CCD sensor response and the transmittance of a liquid crystal tunable filter are given in Figures 4.1 (a)

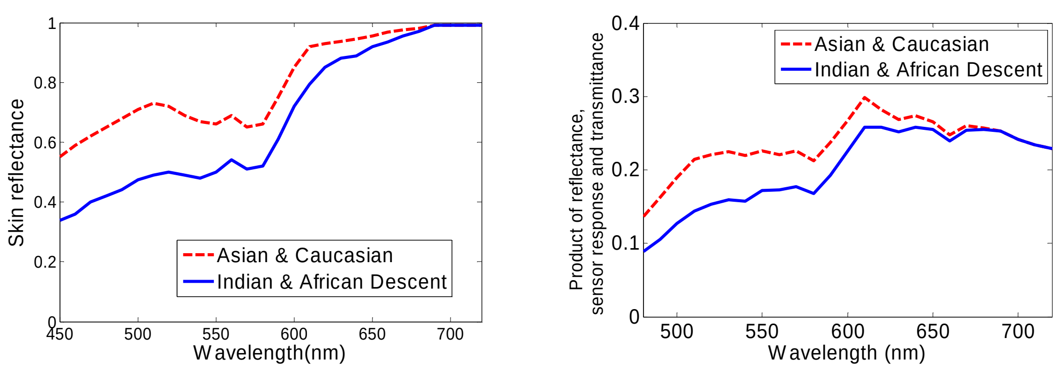

(a) (b)

Figure 4.3. (a) Normalized skin reflectance for different skin colors, and (b) the combined spectral characteristics of three factors, skin reflectance, sensor response, and the transmittance of the LCTF.

and Figure 3.5, respectively. Those two factors are the same for different skin color as long as the same imaging equipment is used for data acquisition. The combined spectral characteristics of the three factors, skin reflectance, sensor response, and the transmittance of the LCTF, are plotted in Figure 4.3 (b). Therefore, given a particular camera, a LCTF and a subject, the product $F_{\lambda_i} = R_{\lambda_i} S_{\lambda_i} T_{\lambda_i}$ remains the same. In this case, the camera response at band λ_i under illumination L_{λ_i} is

$$p_{\lambda_i} = F_{\lambda_i} L_{\lambda_i} . \tag{4.4}$$

Here, the spectral power distributions of different light sources are used to improve face recognition performance. The camera response, p_{1,λ_i}, at band λ_i acquired using a particular illumination, (denoted by L_1), can be represented as

$$p_{1,\lambda_i} = F_{\lambda_i} L_{1,\lambda_i} , \tag{4.5}$$

where L_{1,λ_i} is the spectral power distribution of L_1 at band λ_i. The camera response, p_{2,λ_i}, acquired under another illumination source, L_2, can be represented as

$$p_{2,\lambda_i} = F_{\lambda_i} L_{2,\lambda_i} . \tag{4.6}$$

Comparing (4.5) and (4.6), the spectral image at λ_i under L_1 can be transformed to the corresponding image under L_2 by applying the weight

$$w_{\lambda_i} = L_{2,\lambda_i} \big/ L_{1,\lambda_i} , \tag{4.7}$$

and the corresponding image can be represented as

$$p'_{2,\lambda_i} = p_{1,\lambda_i} w_{\lambda_i} . \tag{4.8}$$

The intensity of the fused image, p'_2, can be represented as

$$p'_2 = \frac{1}{C} \sum_{i=1}^{N} w_{\lambda_i} p_{1,\lambda_i} , \tag{4.9}$$

where $C = \sum_{i=1}^{N} w_{\lambda_i}$. Here, we transform the probe images acquired under a particular illumination to appear as acquired under a different illumination via applying specific weights on each band image and averaging the weighted images.

Different light sources have different spectral properties, For example, halogen light has smooth spectral distribution and has more reddish components than blue components shown in Figure 4.4(a). Daylight affects face recognition the most compared to other light sources because it changes frequently. The spectral distribution of daylight at one time shown in Figure 4.4(b) is smoother than fluorescent light, but spikier than the halogen light. Also it is comprised of more green and blue components than halogen light source. Another type of commonly used light source, fluorescent light, gives out a spiky distribution where the spike locations are decided by the chemical elements in the bulb. In other words, different fluorescent light tubes may show different spectral properties, which is clearly shown in Figure 4.4(c) and (d). The combined spectral behavior of the four factors, spectral response of the camera, transmittance of the LCTF, skin reflectance, and spectral distribution under daylight and halogen light are plotted with different skin tones are given in Figure 4.5.

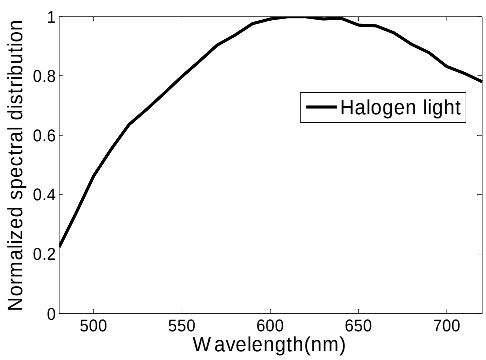

(a)

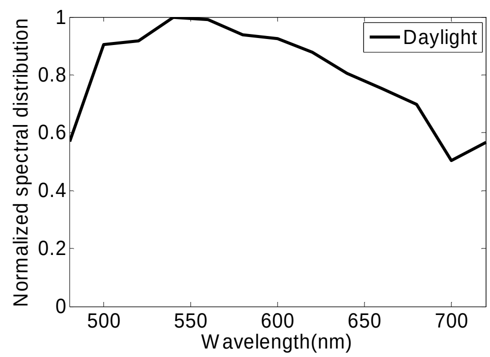

(b)

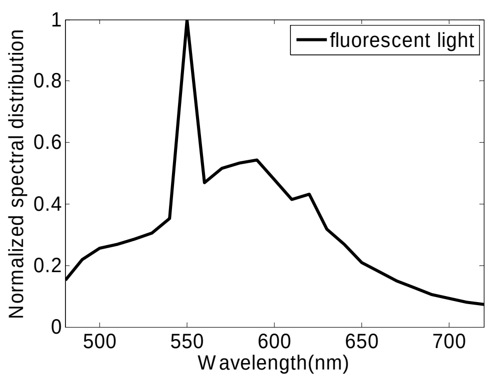

(c)

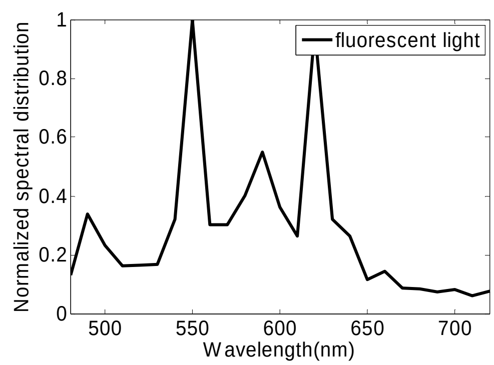

(d)

Figure 4.4. Spectral power distribution of (a) halogen light, (b) day light, (c) fluorescent light and (d) another type of fluorescent light.

4.3 Wavelet fusion

Wavelet based methods have been widely used toward image fusion. Wavelet transform is a data analysis tool that provides a multi-resolution decomposition of an image. The Haar wavelet-based pixel-level data fusion, as described in [Gonzalez04], is used on two set of probes. Given two registered images I_1 and I_2 of the same object in two sets of probes, two dimensional discrete wavelet decomposition is performed on I_1 and I_2, to obtain the wavelet approximation coefficients a_1, a_2 and detail coefficients d_1, d_2. Wavelet approximation and detail coefficients of the fused image, a_f and d_f, are calculated as follows:

$$a_f = W_{a_1} \times a_1 + W_{a_2} \times a_2 \tag{4.10}$$

$$d_f = W_{d_1} \times d_1 + W_{d_2} \times d_2, \tag{4.11}$$

where W_{a_1}, W_{a_2} and W_{d_1}, W_{d_2} are weights determined empirically. The weights are chosen such that $W_{a_1} + W_{a_2} = 1$, $W_{a_1} = W_{d_1}$ and $W_{a_2} = W_{d_2}$. The two-dimensional discrete wavelet inverse transform is then performed to obtain the fused image.

4.4 Rank-based decision level fusion

After studying the pixel level fusion, decision level fusion is also employed on

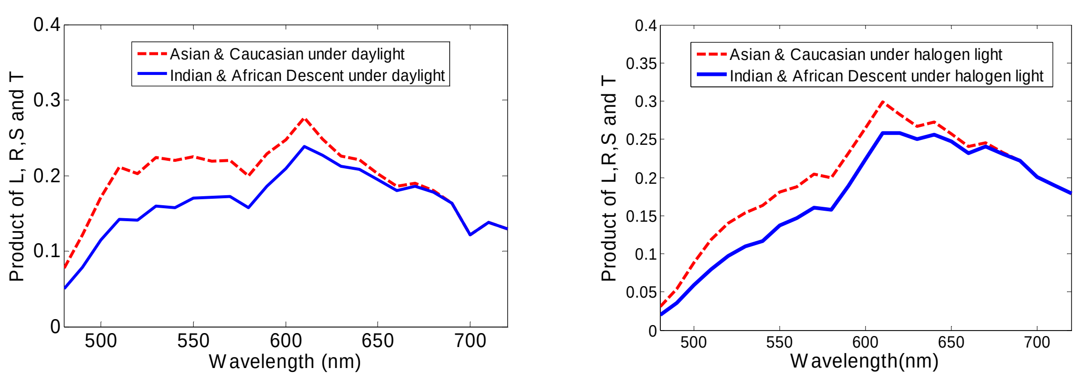

(a) (b)

Figure 4.5. The combined spectral behavior of the four factors, spectral response of the camera, transmittance of the LCTF, skin reflectance, and spectral distribution under (a) daylight, and (b) halogen light.

multispectral images because of its feasibility and robustness to the removal or addition of individual data sources. Methods of decision fusion include majority voting, ranked list combination, AND fusion, OR fusion using the ranks, or the scores generated from the classifiers [Dasarathy94].

Here, we describe a voting decision fusion strategy. First, the rank value of each object *j* in a certain probe set *i* is first obtained. $r_{i,j}$. Objects in the probe set *i*, are compared with gallery images and similarity scores which indicate the similarities between images are calculated. Similarity score are ranked from highest to lowest from 1 to M, which is total number of images in gallery. If object *j* is correctly recognized as *j* with the k^{th} highest similarity score, the rank value of object *j* in probe set *i* is *k*. The lower rank value indicates the higher similarity score and higher tendency to be recognition correctly. Therefore, the lowest rank, denoted as $r_{d,j}$, is then voted for object *j* in probe set *i* as the final decision level rank value. This fusion can be represented as:

$$r_{d,j} = \min\left(r_{1,j}, r_{2,j}, r_{3,j} \ldots, r_{N_F,j}\right), \tag{4.12}$$

where $r_{d,j}$ is the chosen rank value of subject *j*, N_F is the total number of probe sets considered in the decision level fusion. This decision fusion is based on rank values of individuals, and therefore is called rank-based decision level fusion. Eventually, these decisions are cumulated to form the CMC curve of the rank-based decision level fusion.

4.5 Experimental results

Three sets of experiments are investigated in this section to prove that fused MSIs provide better recognition performance than conventional images, especially when the gallery and probes are acquired under different illuminations. Fused images by several proposed algorithms are compared with conventional images by Face-It®, one of the leading commercial face recognition engines. Three illuminants, halogen, fluorescent and daylight are measured and used for experiments.

A numerical measure of the recognition performance is proposed to evaluate and compare the images by different fusion approaches. Often face recognition tests comparing many probe sets with a single gallery result in very similar CMC curves, with the identification rates of different ranks intersecting and crossing over other CMC curves. To make the comparison of various CMC curves, we define a mapping operation projecting the multi-index CMC curve to a single number, CMC measure (CMCM), which is expressed by

$$Q_{CMC} = \sum_{r=1}^{N} \frac{C_r}{N} \cdot \frac{1}{r}, \tag{4.13}$$

where N is the number of gallery and probe images, r represents the rank number, and C_r denotes the number of probe images that can be correctly identified at rank r. $1/r$ can be viewed as a weight, which decreases monotonously as r increases. As a result, rank-one is dominant and contributes the most to the value of CMCM. A better face recognition performance is indicated by a higher CMCM value, which varies between 0 and 1.

FaceIt® developed by Identix is used as the recognition matrix because of its good performance in a vendor test [Phillips00]. FaceIt® calculates similarity scores between one probe and each gallery image. In the identification performance [Phillips00], there is one and only one image in the gallery that is of the same person as the probe; we call this the correct match. If the correct match has the highest similarity score, then the probe is correctly identified and has rank 1. Rank varies from 1 to the size of the gallery. If the correct match has the k^{th} largest similarity score, then the probe has rank k. The identification rate at rank k is the fraction of probes that have rank k or higher. Identification rate is used to compare the performance of the different probes formed from different fusion methods.

4.5.1 Fluorescent gallery, halogen probe

In this set of experiments, fused images by the proposed fusion algorithms, including physics-based weighted fusion (PWF), illumination adjustment (IA), and wavelet fusion (WF), are implemented. Face recognition performances of the above images as different probe sets are compared with images by averaging fusion (AF), PCA fusion (PCAF) and with conventional images. The conventional broad-band images under fluorescent light are used as gallery images. The probe images are acquired under halogen light. The probe sets include conventional broad-band images, and fused spectral images by PWF, IA, WF, AF and PCAF. The CMCM values of different probes are presented in Table 4.1.

We found from CMCM values that fused images by physics-based weighted fusion (Probe 1) and illumination adjustment (Probe 2) using the ratio of the spectral distributions of fluorescent and halogen lights outperform conventional images (Probe 0). Empirically, Probe 3, the multispectral band 640nm also has a higher recognition rate than conventional images. Furthermore, fused images (Probe 4) by wavelet fusion via band 640nm and conventional images have the highest CMCM value of 96.38%. Averaging fusion (Probe 5) and PCA (Probe 6) fusion do not outperform conventional images. CMC plots with the rank value equal and less than 20 are presented in Figure 4.6. Both CMCMs and CMC plots have shown that physics-based weighted fusion (Probe 1), IA (Probe 2), certain single band (Probe 3) and wavelet fusion (Probe 4) outperform conventional images (Probe 0). The visualized sub-spectral images of one subject under halogen light are given in Figure 4.7. For the purpose of visualization, linear stretching is conducted on each of the sub-spectral image. The fused images of the same subject obtained by the proposed methods are also shown in Figure 4.7.

4.5.2 Fluorescent gallery, halogen probe with longer time lapse

In this set of experiments, the recognition performances of different fusion algorithms and conventional images are compared as probes. The time lapses for this experiment are around six months long while those of previous one are around three months. The gallery images are acquired under another type of fluorescent light than for the precious experiment. Conventional broad-band images and fused probe sets from spectral narrow-band images acquired under halogen illumination are the probe sets. CMCMs are given in Table 4.2.

It was observed from Table 4.2 that rank-based decision level fusion (Probe 4) of broad-band and band 640nm images provides a performance of 100% recognition rate. The wavelet fusion (Probe 3) of broad-band and band 640nm gives the second best face recognition performance of 97.1%. Fusion by illumination adjustment (Probe 2) slightly improved the recognition performance 93.8% from conventional broad-band images 93.7%. In addition, averaging and PCA fusion (Probe 5 and Probe 6) of MSIs cannot provide a higher recognition rate than conventional images. The CMC plots with the maximal rank value of 10 are presented in Figure 4.8 and some examples of probe images of one subject were shown in Figure 4.9. The sub-spectral images for each fusion method are shown in Figure 4.7(a-f). There is noticeable appearance difference between the above images. The lighting for the fused images is halogen light and the lighting for the gallery images is fluorescent light in this experiment. Therefore, the fused images visually appear different from the corresponding gallery images. Another reason for the difference in visual appearance is that the gallery images under fluorescent light were acquired six month apart from the probe sets and fused images. The improvement of the recognition rate lies in the facts that multispectral images can separate illumination information from a subject’s reflectance. For example, in physics-based weighted fusion and illumination adjustment fusion, the spectral power distributions of these two lightings are specifically employed to obtain the weights for fusion so that our fused images are adjusted by the illumination-specified weights.

4.5.3 Halogen gallery, daylight probe

We test our proposed fusion algorithms under the most severe changing lighting conditions, outdoor daylight in this set of experiments. Also, a time separation of six months or longer is introduced in this experiment. Experiment 4.5.3 is very close to the practical face recognition situations. Conventional broad-band images and fused probe sets from the spectral narrow-band images acquired under daylight are compared while The corresponding CMCM values of all tested probes are shown in Table 4.3. It is observed that images generated by physics-based weighted fusion, illumination adjustment, wavelet fusion and rank-based decision level fusions (Probe 1 to Probe 4) all

Table 4.1. Images used in gallery and probes and the corresponding CMCM values.

Data set	Gallery	Probe 0	Probe 1	Probe 2
	Fluorescent Broad-band	Halogen Broad-band	Halogen PWF	Halogen IA
CMCM		95.92 %	95.99 %	95.99 %
Data set	**Probe 3**	**Probe 4**	**Probe 5**	**Probe 6**
	Halogen Band 640nm	Halogen WF	Halogen AF	Halogen PCA
CMCM	96.14 %	**96.38 %**	95.92 %	93.79 %

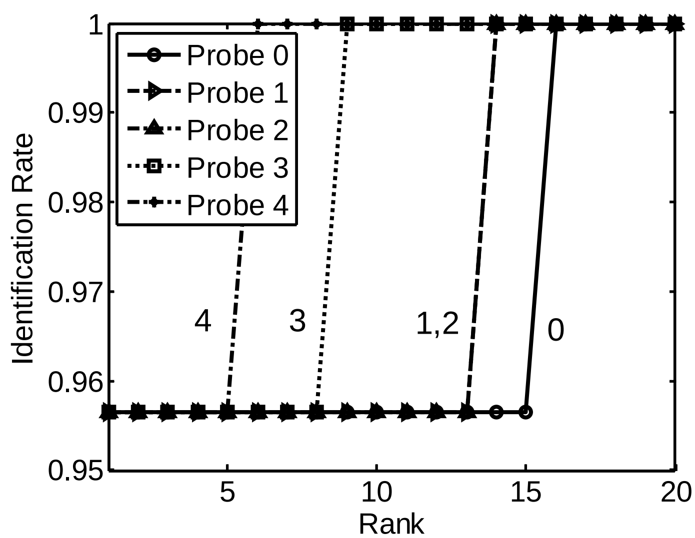

Figure 4.6. CMC plots of probes in Experiment 4.5.1. Physics-based weighted fusion (Probe 1), IA (Probe 2), single band (Probe 3) and wavelet fusion (Probe 4) outperform conventional images (Probe 0).

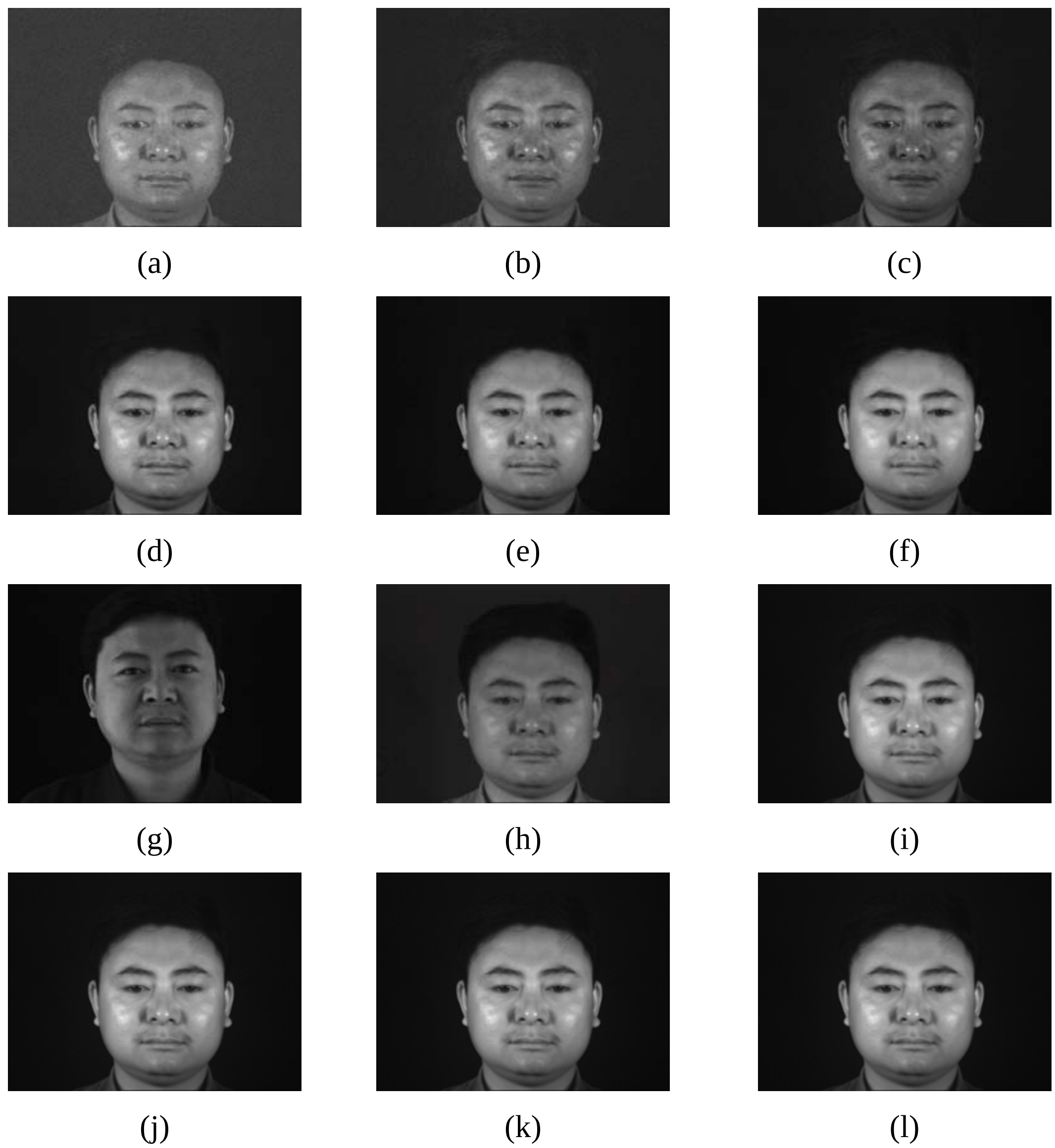

Figure 4.7. Image samples of a subject in Experiment 4.5.1. Sub-spectral image under halogen light at wavelength of (a) 500nm, (b) 540nm, (c) 580nm, (d) 620nm, (e) 660nm, and (f) 720nm. (g) Gallery-monochromatic image under light fluorescent-1, (h) Probe 0-monochrmatic image under halogen light, (i) Probe 1- fused image by physics-based weighted fusion, (g) Probe 2-fused image by illumination adjustment, (k) Probe 3-spectral image at wavelength 640nm, and (l) Probe 4-fused image by wavelet fusion.

Table 4.2. Images used in gallery and probes and the corresponding CMCM values.

Data set	Gallery	Probe 0	Probe 1	Probe 2
	Fluorescent Broad-band	Halogen Broad-band	Halogen PWF	Halogen IA
CMCM		93.7 %	92.4 %	93.8 %
Data set	**Probe 3**	**Probe 4**	**Probe 5**	**Probe 6**
	Halogen WF	Halogen RLDF	Halogen AF	Halogen PCA
CMCM	97.1 %	100 %	91.7 %	90.6 %

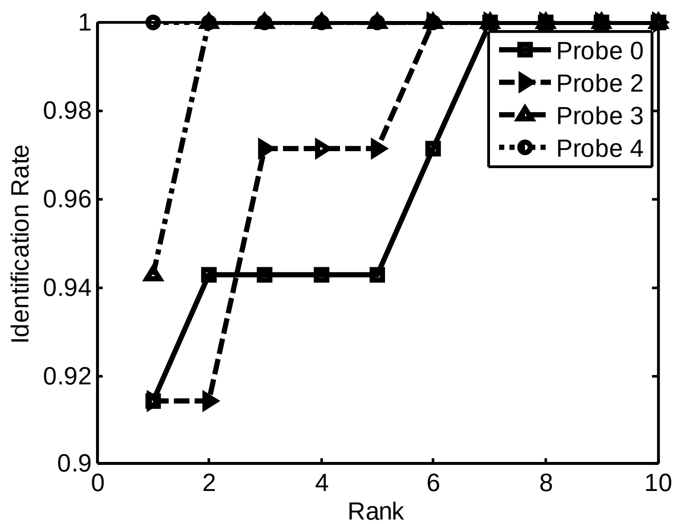

Figure. 4.8. CMC plots of probes in Experiment 4.5.2. Illumination adjustment, wavelet fusion and rank-based decision level fusion (Probe 2, 3 and 4) are more robust to longer time lapse than conventional monochromatic images (Probe 0) and provide better performances.

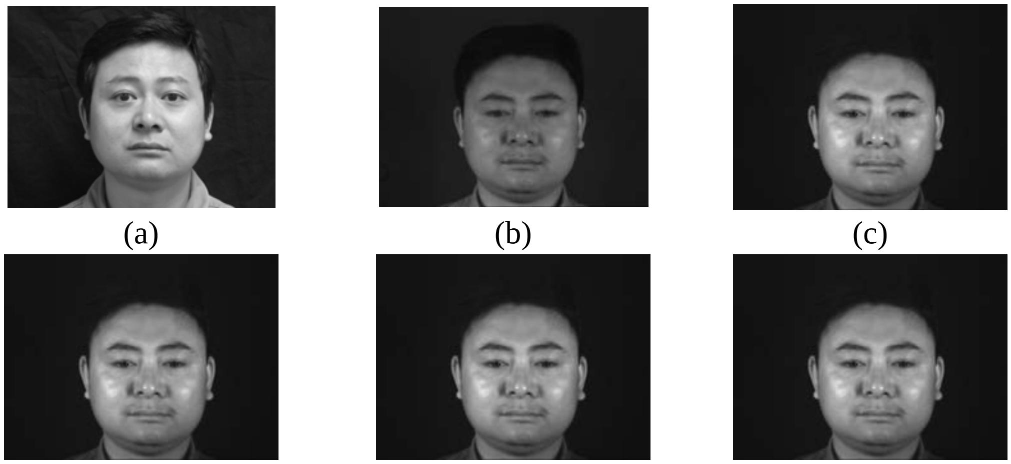

(a) (b) (c)

(d) (e) (f)

Figure 4.9. Image samples of a subject in Experiment 4.5.2. (a) Gallery-monochromatic image under fluorescent light, (b) Probe 0-monochrmatic image under halogen light, (c) Probe 1 - fused image by physics-based weighted fusion, (d) Probe 2-fused image by illumination adjustment, (e) Probe 3-fused image by wavelet fusion, and (f) Probe 6-fused image by PCA.

Table 4.3. Images used in gallery and probes and the corresponding CMCM values.

Data set	**Gallery**	**Probe 0**	**Probe 1**
	Halogen Broad-band	Daylight Broad-band	Daylight PWF
CMCM		53.21 %	58.49 %
Data set	**Probe 2**	**Probe 3**	**Probe 4**
	Daylight IA	Daylight WF	Daylight RDLF
CMCM	59.70 %	64.35 %	83.18 %

provide higher recognition rates than monochromatic images (Probe 0). The wavelet fusion was implemented between spectral band images at 700nm and the corresponding broad-band images. The weights used for weighted fusion are obtained by multiplying the spectral power distribution of the light sources and the transmittance of the LCTF. As shown in Figure 4.10, the identification rate at Rank-one of rank-based decision level fusion (Probe 4) is of 71.43%, while for monochromatic daylight (Probe 0) images the rate is only of 40%. An increase of up to 78% for Rank-one recognition was obtained for outdoor daylight probes by using the rank-based decision level fusion. The weights in physics-based weighted fusion and illumination adjustment fusion are illustrated in Figure 4.11. The visualized sub-spectral images of one subject under daylight and the fused images by the proposed methods are shown in Figure 4.12.

4.6 Summary

Multispectral imaging systems have been proven extraordinarily useful in numerous imaging applications. However, face recognition using narrow-band MSIs in the visible spectrum was unexplored for face related research. We utilize MSIs for face recognition not only because MSIs carry more useful information than conventional images, but also because we can separate the spectral information of illumination from other spectral information.

After the data acquisition, several new image fusion algorithms were proposed for improving recognition performance. To our knowledge, this is the first research that uses and fuses MSIs in the visible spectrum for improving face recognition and that compares fused MSIs images with conventional images by a commercial face recognition engine. Different fusion methods were investigated, including fusion by averaging, PCA, wavelet, physics-based weighted fusion and illumination adjustment. Rank-based decision level fusion was proposed and implemented between certain band images and the corresponding monochromatic images. Face recognition tests were conducted in three experiments with different illuminants for galleries and probe images, respectively. The respective CMC curves were obtained and CMCM values were calculated. From section 4.5.1 and section 4.5.2, we can conclude that with significant illumination differences and large time lapse, illumination adjustment and wavelet fusion are very promising fusion approaches for multispectral face images. They provide a stable and better performance than conventional monochromatic images. Last but not least, outdoor daylight probes with 6 months time lapse between gallery and probes acquisition, in which situation usually a large drop of recognition rate occurs, were studied in section 4.5.3. The most promising improvement in recognition rate was obtained with wavelet fusion and rank-based decision level fusion. In addition, physics-based weighted fusion and illumination adjustment again provide higher recognition rates than conventional monochromatic images in the case of outdoor images involved.

In a word, face images created by fusion of continuous spectral images can improve recognition rates compared to conventional images as probes while the gallery images are acquired under different illumination. Significant improvement of an increase of up to 78% for rank-one recognition was obtained for outdoor probes by using rank-based decision level fusion. Physics-based weighted fusion in most cases provided better recognition rate than conventional images. The fused images by wavelet fusion and illumination adjustment always provided higher recognition rates than conventional images under four different lighting conditions, especially in the case of a large time lapse, which simulates real world scenarios where galleries and probes are often acquired months or years apart.

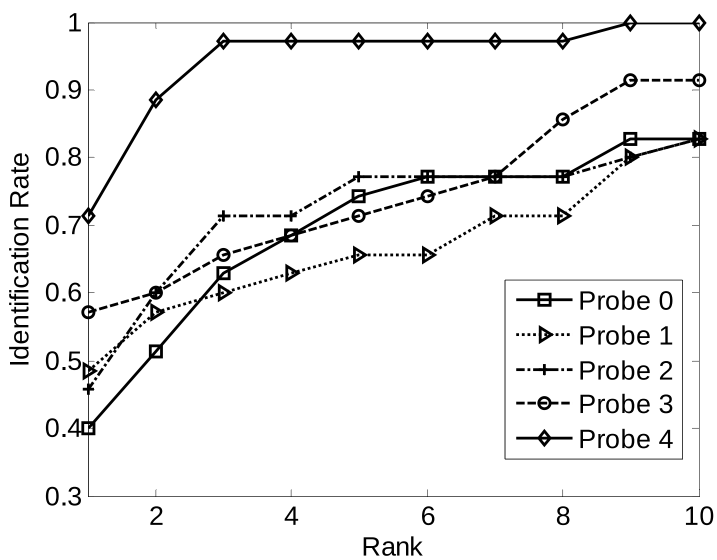

Figure 4.10. The CMC plots of selected probes in Experiment 4.5.3. Physics-based weighted, IA, wavelet and rank-level decision fusions (Probe 1 to Probe 4) all provide higher recognition rates than monochromatic images (Probe 0).

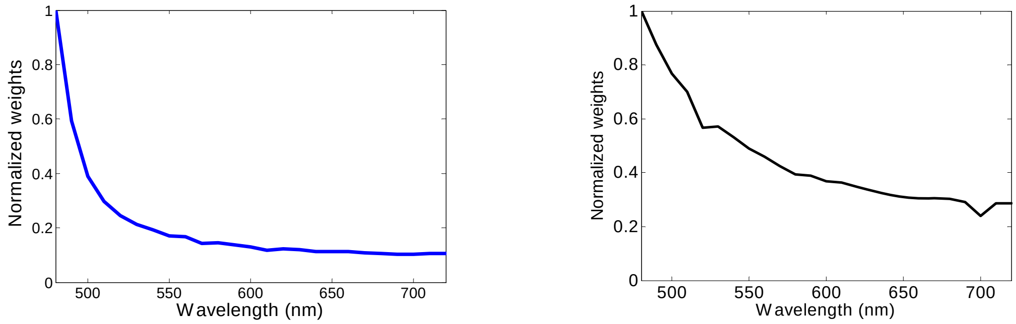

(a) (b)

Figure 4.11. (a) The weights used in physics-based weighted fusion and (b) weights used for illumination adjustment fusion which is the ratio between the spectral power distributions of daylight and halogen light.

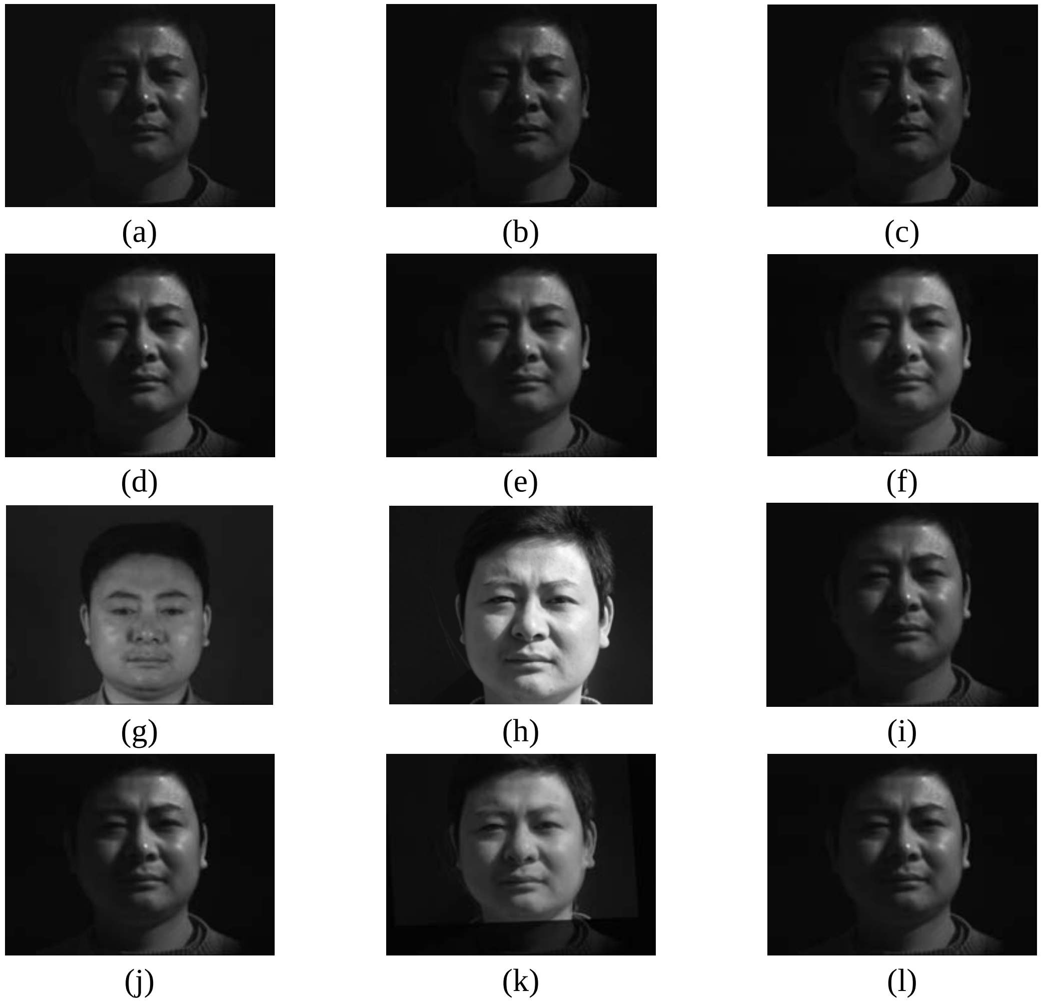

Figure 4.12. Image samples of a subject in Experiment 4.5.3. Sub-spectral image at wavelength of (a) 500nm, (b) 540nm, (c) 580nm, (d) 620nm, (e) 660nm, and (f) 720nm. (g) Gallery-monochromatic image under halogen light, (h) Probe 0-monochrmatic image under daylight, (i) Probe 1-fused image by physics-based weighted fusion, (g) Probe 2-fused image by illumination adjustment, (k) Probe 3-fused image by wavelet fusion under daylight, and (l) fused image by averaging fusion under daylight.

5 Distance-based band selection

Multiple narrow-band spectral images and high dimensional face datasets benefit better discriminations power and enhance face recognition performance. However, such larger amount of image datasets often involves problems in image acquisition, image storage and image processing. Therefore, dimensionality reduction techniques and here, band selection algorithms can be applied to original multispectral images.

In order to achieve an improved recognition performance in comparison with conventional broad-band images, in this chapter a new method that specifies the optimal spectral range for multispectral face images according to given illuminations is proposed and discussed. The novelty of this method lies in the introduction of a distribution separation measure and the selection of the subset bands by ranking these separation values.

The chapter is organized as follows. Section 5.1 introduces the concept of the distance-based band selection (DBS). The significance of distribution of genuine and imposter data sets is given in section 5.2. The proposed technical approach is presented in section 5.3. Section 5.4 discusses the robustness of this proposed method via four experiments. Summary is given in section 5.5.

5.1 Introduction

An important process in multispectral data analysis is the dimensionality reduction which reduces the redundancy of both spectral and spatial information without losing valuable details needed for the object recognition, discrimination and classification. There are two methodologies: feature extraction and feature/band selection. In feature extraction, a new and reduced data set representing the transformed initial information is obtained, whereas in feature selection a subset of relevant data from the original bands is chosen. Compared to feature extraction, feature/band selection methods identify bands which are a subset of the original spectral bands that contains most of the characteristics. Therefore, my focus is in feature selection rather than feature extraction due to the fact that in feature extraction the total amount of information is needed to obtain the new set transformed data. In addition, selecting a subset of relevant bands from the original set allows the process of image acquisition to be reduced to a certain number of bands instead of dealing with the whole amount of data, making simpler the image acquisition and analysis

[Sotoca07].

The idea of distance-based band selection comes from the in-depth understanding the face recognition process and the meaning of the separability between the similarity scores of genuine and imposter sets. The separability or the distance between these two sets for each band of all the observed subjects indicates the recognition performance of the certain band. The larger the distance between these two sets of one band gives a better chance to outperform other bands.

The main contribution is an illumination-specific band selection algorithm that provides a quantitative performance evaluation metric which can rank spectral bands from the top one selection to total number of available bands in visible domain. Users have the freedom to select number of bands. However, it is not true that larger number of bands provide better performance. Kernel density estimation is used to estimate the distributions of the two sets and different distance measures are employed to calculate the separation between the two distributions.

5.2 Genuine and imposter sets

In face recognition process, there are several sequential steps: image preprocessing, feature extraction, similarity score calculation and classification. The feature extraction can be global methods, such as eigenface, and can also be local methods, such as geometry of eyes, noses and other facial features. After features are extracted, each image in probe can be represented by a feature vector or matrix. A comparison between each pair of probe image and gallery image is carried out and a similarity score is obtained which indicates the similarity level of two images. Eventually, the similarity score or the extracted features are inputted to a classifier to obtain the recognition performance. This process is described in Figure 5.1.

In a face recognition comparison, a gallery consists of a set of samples $\{ g_1, \dots g_N \}$. N is the total number of samples in gallery, with one sample per person. When a probe p_j is presented to a system, it is compared with the entire gallery. The comparison between a probe p_j and each gallery biometrics sample g_i produces a similarity score S_{ij}.

Since similarity scores can quantitatively evaluate the similarities between two images under comparison, a larger similarity score indicates more resemblance between the two samples. Our approach starts from the similarity score calculation. Denote S_{ij}^k as the similarity score between the probe image of the i^{th} subject collected at the k^{th} band and the gallery image of the j^{th} subject. The similarity scores in each probe set can be divided into two groups, referred to as the genuine G_k and imposter I_k sets. The genuine and imposter

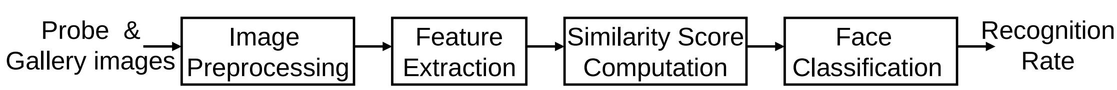

Figure 5.1. General face recognition block diagram.

sets are defined as: $G_k : \{S_{ij}^k, i = j\}$ and $I_k : \{S_{ij}^k, i \neq j\}$, respectively. The genuine set contains the similarity scores with probe and gallery images from the same subject while the imposter set consists of similarity scores with the probe and gallery images from different subjects. Figure 5.2(a) shows some face samples with the similarity scores of the genuine set for some gallery and probe images. The gallery images are acquired under fluorescent light and the probe sets are acquired at wavelength 720nm under halogen light. Figure 5.2(b) gives samples with similarity scores of imposter set of one subject to the other four subjects for the same gallery and probe images. In my work, the similarity scores are obtained in general sense from well-known face recognition engines, Identix's FaceIt® and Cognitec's FaceVACS®. The features involved in the similarity score calculation are unknown to us. However, it can be used as benchmark for my methodology. The histogram of this complete genuine set of the same gallery and probe sets is plotted in Figure 5.3 (a) and the histogram of a complete imposter set of the same probe set is given in Figure 5.3 (b). The histogram illustrates the number of subjects in the whole probe set at a certain similarity score.

Figure 5.4 gives an example and illustrates the similarity score difference between the genuine and imposter sets. As we can see from both image illustration and histogram that the genuine similarity score is higher than the imposter scores for a subject.

For a certain probe set, we assume that a higher similarity score indicates a better match. Higher similarity scores of the genuine set or the distribution in a probability density function towards higher values, means that there are more subjects look relatively more similar to their own faces that others, which leads to a better recognition rate. The same principle works on imposter set. Lower similarity scores of the imposter sets means more subjects look relatively less similar to other subjects which also leads to a better recognition rate. In other words, the distribution of the imposter sets in the probability distribution function is expected to be towards zero for a relative good performance. This idea is illustrated is shown in Figure 5.5. Intuitively, the distance between imposter and genuine sets for a certain probe can specify the recognition performance of the probe set. Ideally, the genuine and imposter sets should cluster at the high and low ends of the score scale, respectively, without overlap so that an appropriate threshold can be derived to completely separate the genuine matches from the imposter ones. In such condition, a perfect 100% recognition rate can be achieved. However, in practical situation, there often times exists overlapped regions between these two sets. Therefore, an important criterion in evaluating the recognition performance is the separation between the distributions of the similarity scores of the genuine and imposter sets.

For a face recognition system using multispectral images, the behavior of the similarity scores from various bands differs substantially to where it results in a varying face recognition rate. Figure 5.6 illustrates the probability density functions (PDFs) of the genuine and imposter sets for bands 480nm and 720nm. The x-axis shows the similarity score values varying from 0 to 3.9 and the y-axis is the estimated probability density. From visual inspection according to the means of the genuine and imposter PDFs, the separation in band 720nm is more conspicuous, which suggests that the probe set collected at band 720nm should produce a higher face recognition rate in comparison with the probe set at band 480nm.

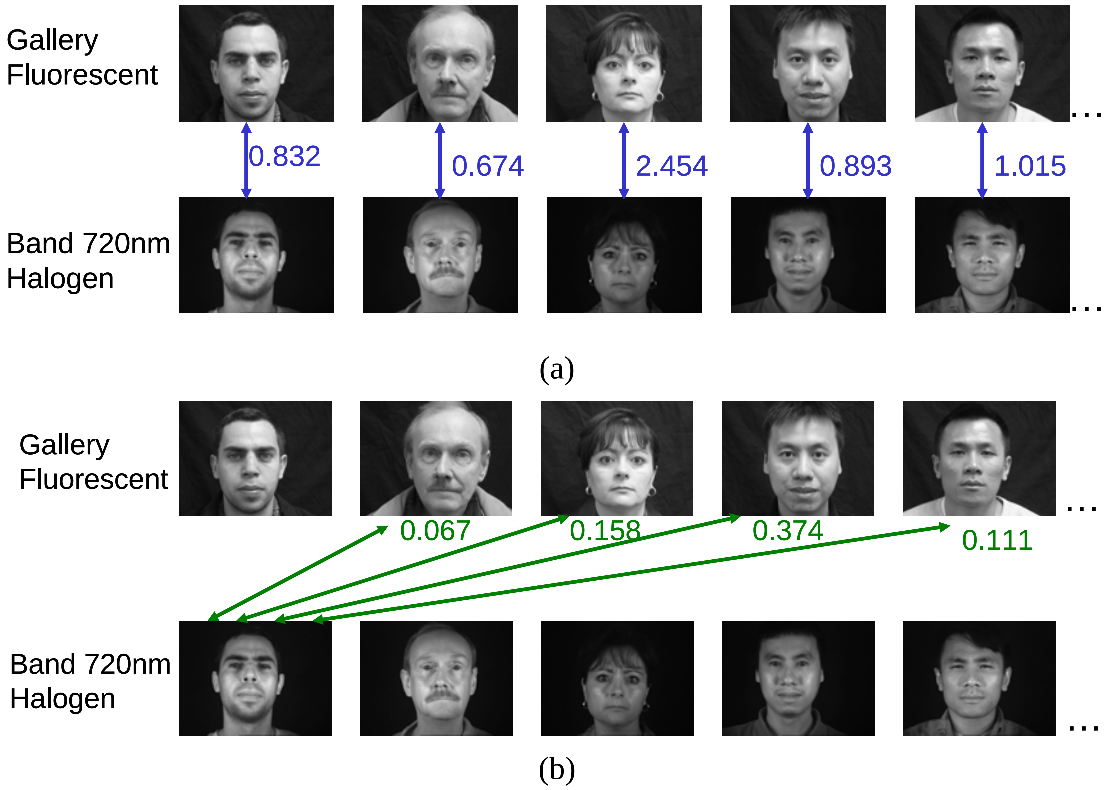

Figure 5.2. (a) Genuine similarity scores of 5 pairs of images in gallery and probe sets. (b) Imposter similarity scores of one subject to other 4 subjects in the same gallery and probe sets.

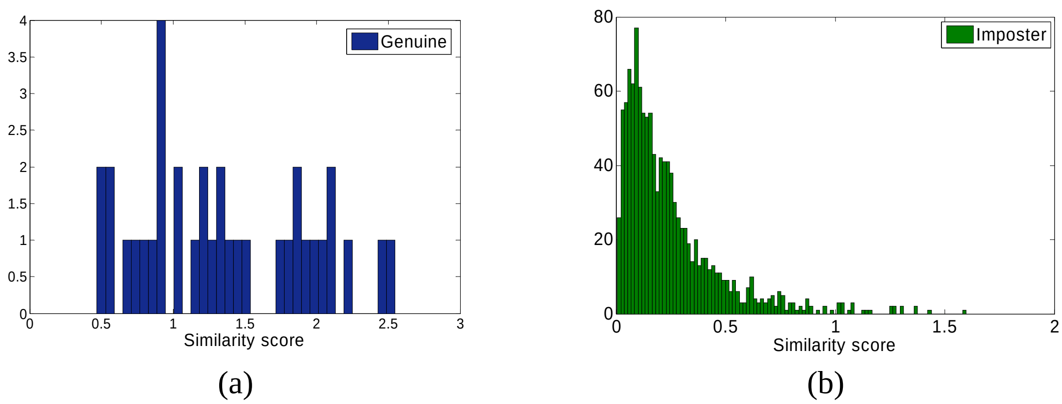

Figure 5.3. Histogram of similarity scores of a (a) genuine and (b) imposter data sets from the same probe set. There are 35 subjects in the probe set. Therefore, there are 35 genuine data points and 1190 imposter data points.

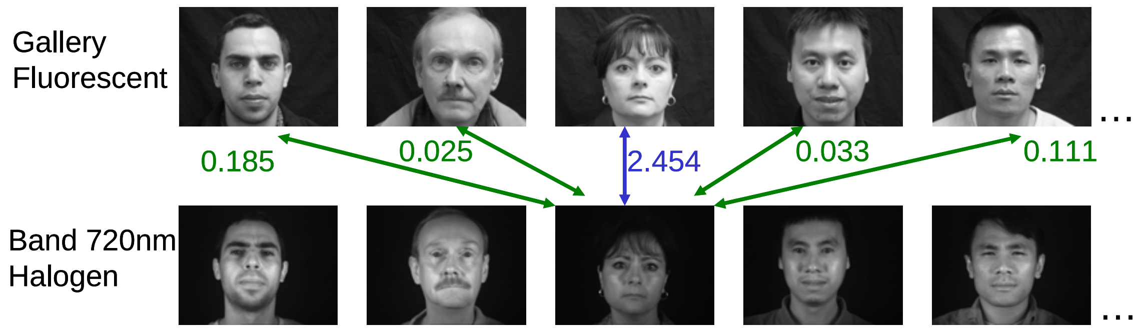

(a)

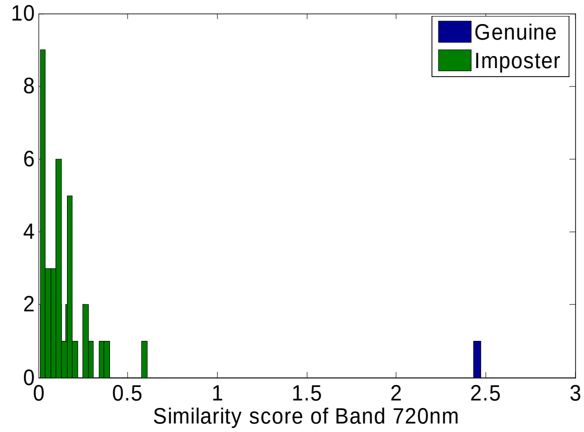

(b)

Figure 5.4. (a) Illustration of one subject's genuine similarity score and imposter similarity scores to other four subjects. (b) Histogram to show the separation between the imposter scores and genuine similarity score for this subject (total 35 subjects).

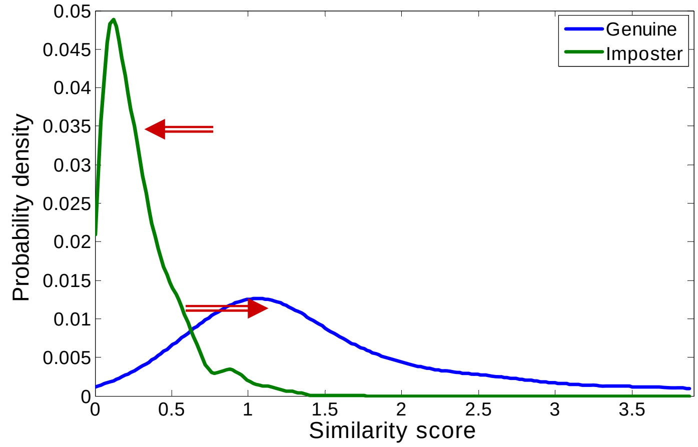

(a)

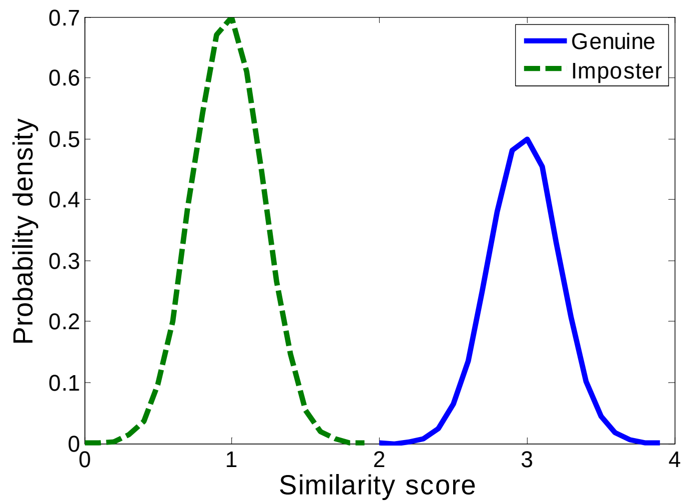

(b)

Figure 5.5. (a) Illustration of the probability mass function of similarity scores of imposter and genuine set of the probe set at 720nm under halogen light with fluorescent for gallery. (b) Ideally, the similarity scores of two sets have completely separated distributions and a perfect 100% recognition rate can be achieved.

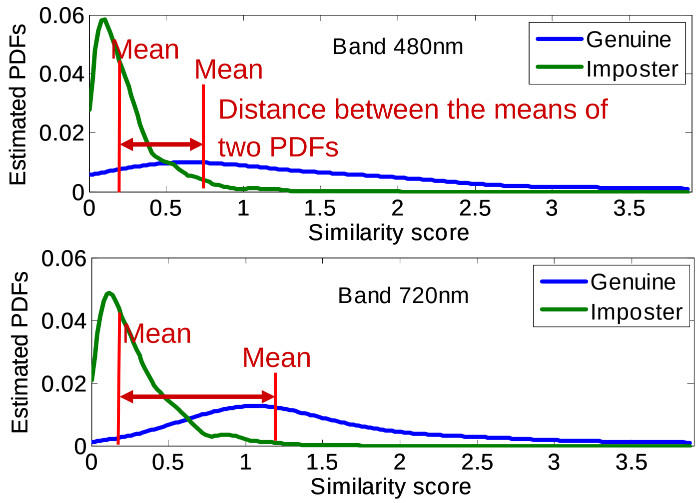

Figure 5.6. Illustration of different separations between the PDFs of the similarity scores from the genuine and imposter sets. More separated PDFs are observed from band 720nm than from band 480nm.

In general, we propose using the separation between the genuine and imposter sets to select the optimal bands given illumination conditions. Therefore, we name this algorithm distance-based band selection. The technical approach of this algorithm is discussed in the following section.

5.3 Technical approach

To obtain the quantity of the separation measure between imposter and genuine sets, we need an accurate estimation of the PDFs of the genuine $\hat{p}_{G,k}(x)$ and imposter $\hat{p}_{I,k}(x)$ sets and a quantified measure J_k to evaluate the separation between them. Recall that the total number of multispectral bands is N_B and that λ_k denotes the central wavelength of the k^{th} band. The complete set of multispectral bands is $B = \{\lambda_k \mid k = 1,\dots,N_B\}$. We want to find an subset $B_{opt} \subset B$ such that $B_{opt} = \{\lambda_k \mid rank(J_k) \le N_{opt}\}$, where N_{opt} is the number of bands to be selected and $rank(J_k)$ returns k' if J_k is the $(k')^{th}$ largest separation measure.

The pipeline of the distance-based band selection mechanism is illustrated in Figure 5.7. Face recognition starts typically with image preprocessing including segmentation and normalization. Afterward, salient features are extracted. Based on the features extracted from pairs of probe and gallery images, similarity scores are computed. Then, spectral band selection is performed as follows: (1) the similarity scores distributions of the genuine and imposter sets are estimated using kernel density functions. (2) Distance measure, Jeffrey divergence, is calculated to quantitatively describe the separation between these two distributions. Step 1 and step 2 are conducted on all the probe sets. (3) The optimal spectral range is selected according to the requirement. Finally, images from the selected bands are fused and fed into a classification engine that outputs the recognition rate.

5.3.1 Probability density function estimation

The discrete data points of the similarity scores of genuine and imposter sets first need to be transformed to continuous functions so that the distance can be measured between each genuine and imposter pair. There are many ways of estimating a distribution out of discrete data points. For parametric density estimation, the specific functional form for the density model is assumed and its parameters are then optimized by fitting the models to the data set, such as Gaussian and Power exponential. The drawback of the parametric density estimation includes that it depends upon one or more parameters and the functional form might not be consistent with the data resulting in a bad model.

On the other hand, non-parametric density estimation determinates the density entirely by the data. Histogram is one of the non-parametric densities. However, it is not a smooth estimation and the results are badly affected by the number of bins and the end points of the bins. Therefore, kernel density estimation is used to obtain the probability density function because the underlying density can be estimated without assuming a particular

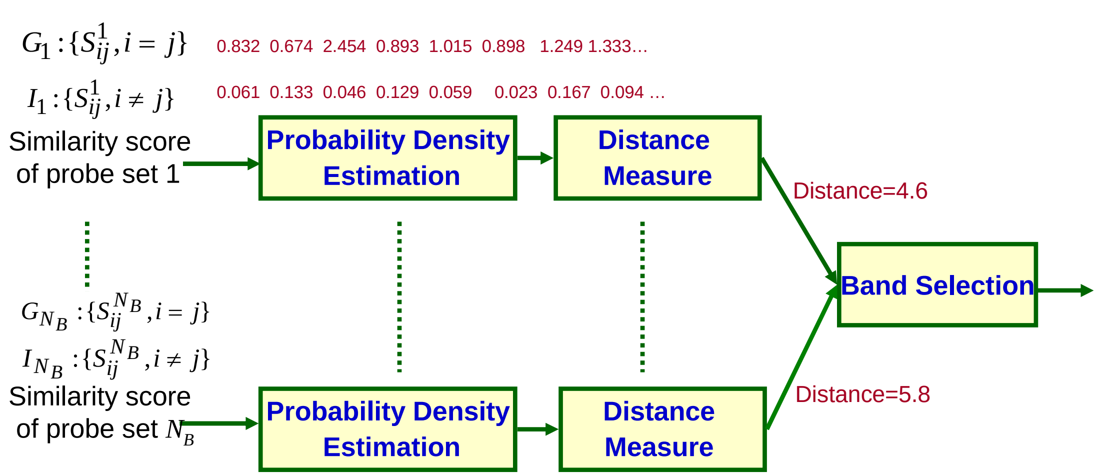

Figure 5.7. Illustration of the algorithm pipeline. The blocks of proposed steps are filled with yellow and the steps are highlighted in blue color.

form or structure of it. Kernel density estimators belong to non-parametric density and it was introduced by [Rosenblatt56, Whittle58, Parzen62]. Formally, kernel estimators smooth out the contribution of each observed data point over a local neighborhood of that data point. The estimated density at any point *x* is given by

$$\hat{p}(x) = \frac{1}{Nh}\sum_{i=1}^{N} K\left(\frac{x - x_i}{h}\right). \tag{5.1}$$

$\int K(t)dt = 1$. Here $K(\bullet)$ denotes the kernel function used for density estimation and *h* is the smoothing parameter. *K* is usually chosen to be a smooth unimodel function with a peak at 0. *N* is the number of data points. Below we show the most common kernel function in Table 5.1.

The illustration of the probability density estimation by kernel density estimation for the similarity scores of the genuine and imposter sets is given in Figure 5.8. From the similarity scores of various subjects in a probe set, the distributions of the genuine and imposter sets, denoted as $\hat{p}_{G,k}(x)$ and $\hat{p}_{I,k}(x)$, can be estimated using kernel density estimation (KDE) [Wasserman05]

$$\hat{p}_{G,k}(x) = \frac{1}{Nh_{G,k}}\sum_{i=1}^{N} K\left(\frac{x - S_{ii}^{k}}{h_{G,k}}\right), \tag{5.3}$$

Table 5.1. Most common used kernel functions

Uniform	$\frac{1}{2};\ (-1 \le t \le 1)$
Triangle	$(1-\lvert t \rvert);\quad (-1 \le t \le 1)$
Gaussian	$\frac{1}{\sqrt{2\pi}}\exp\left(-\frac{1}{2}t^2\right);\ -\infty < t < \infty$
Epanechnikov	$\frac{3}{4}\left(1-t^2\right);\ (-1 \le t \le 1)$
Biweight or Quaritic	$\frac{15}{16}\left(1-t^2\right)^2;\quad (-1 \le t \le 1)$
Triweight	$\frac{35}{32}\left(1-t^2\right)^3;\quad (-1 \le t \le 1)$
Cosine	$\frac{\pi}{4}\cos\left(\frac{\pi}{2}t\right);\ (-1 \le t \le 1)$

and

$$\hat{p}_{I,k}(x) = \frac{1}{N(N-1)h_{I,k}} \sum_{i=1}^{N} \sum_{j=1, j \neq i}^{N} K\left(\frac{x - S_{ij}^{k}}{h_{I,k}} \right). \tag{5.4}$$

$h_{G,k}$ and $h_{I,k}$ are the smoothing parameter for each of the kernel estimation. *N* represents the total number of subjects in probe data sets and also the number of subjects in gallery. Note that in the performance investigation of face identification, the number of samples in probe is equal to the number of samples in gallery.

Note that the choices of the width $h_{G,k} / h_{I,k}$ affect the efficiency of the kernel density estimation. Minimizing the asymptotic mean integrated square error (AMISE) [Mugdadi03] is the most commonly used method of choosing the smoothing parameters in kernel estimation, which is normally denoted as h_{AMISE}. The advantage of AMISE is the fact that it provides a very practical method of bandwidth selection. The disadvantage of it is that if the smoothing parameter is wrong and if the population is not normally distributed, AMISE is not always the optimal solution. The estimated density obtained using h_{AMISE} hides a lot of structure by smoothing away modes. The calculation of h_{AMISE} is given by

$$h_{AMISE} = \left[\frac{\rho(K)}{N \mu(K)^2 \sigma(p')} \right]^{1/3}, \tag{5.6}$$

where $\rho(K) = 2\int_{-\infty}^{\infty} x K(x) K_I(x) dx$, $\mu(K) = \int_{-\infty}^{\infty} x^2 K(x) dx$, and $\sigma(p') = \int_{-\infty}^{\infty} p'(x)^2 dx$ with $K_I(x) = \int_{-\infty}^{x} K(x) dx$.

5.3.2 Optimization of smoothing parameter

The quality of a kernel estimate depends on both of the shape of the kernel and the value of its smoothing parameter/bandwidth. The smoothing parameter controls the smoothness of the density estimate and it determines the trade-off between the bias and variance. It is important to choose the most appropriate as a value that too small or too large is not useful. Small values of smoothing parameter lead to very spiky estimates and the bias in the density estimate is small but the variance is large. While larger smoothing parameter values lead to over-smoothing and the bias in the density estimate is large but the variance is small. This type of tradeoff is a pervasive one, in nearly all kinds of model selection including regression, density estimation, and smoothing.

In this section, a new entropic or information-theoretic measure of complexity called Information Complexity (ICOMP) of [Bozdogan88, Bozdogan00] as a decision rule of kernel estimation is introduced. The development and construction of ICOMP is based on a generalization of the covariance complexity index originally introduced by [Emden71].

Many model-selection procedures (Original AIC [Akaike74]) that take the form of a penalized likelihood (a negative log likelihood plus a penalty term) have been proposed.

ICOMP begins with a matrix of data, number of samples *n* of a particular scenario accumulated over several factors/features of variables *p.* For example, in our study, the spectral bands are the features that are under study and selection. Therefore, the number of features are the number of bands, $p = N_B$. The number of samples *n* is the number of subjects *N*. We are looking for subset of N_B spectral bands which can be most efficiently representative and contain the potential for knowledge discovery. The other way the problem might surface is how less of the huge *N by* N_B matrix is sufficient for making decisions. Traditionally, the decision making heuristically is made by using correlations/similarity measures between variables and choosing variables that have minimum correlation. Instead of penalizing the number of free parameters directly, ICOMP penalizes the covariance complexity of the model. It is defined by

$$ICOMP = -2\log L\left(\hat{\theta}\right) + 2C_1(F^{-1}(\hat{\theta})) \,, \tag{5.7}$$

where $L\left(\hat{\theta}\right)$ is the maximized likelihood function, $\hat{\theta}$ is the maximum likelihood estimate of the parameter vector θ under the model. The C_1 measure for penalizing uncertainty is obtained by maximizing mutual information,

$$C_1\left(\hat{F}^{-1}\left(\hat{\theta}\right)\right) = \frac{s}{2}\log\left[\frac{tr\left(\hat{F}^{-1}\left(\hat{\theta}\right)\right)}{s}\right] - \frac{1}{2}\log\left|\hat{F}^{-1}\left(\hat{\theta}\right)\right|, \tag{5.8}$$

where $s = rank\left(\hat{F}^{-1}\right)$, where here F^{-1} *is* the inverse of the Fisher information matrix (IFIM). |.| refers to the determinant and *tr* refers to the trace of the matrix.

There are many forms of ICOMP for different application purpose. In our case, ICOMP in the form of kernel density estimation is our particular interest because the by this form, the optimal smoothing parameter for kernel estimation can be obtained. Therefore, ICOMP(kernel) considering misspecification is given by [Bozdogan05]

$$\begin{aligned} ICOMP(Kernel)_{Misspec} &= -2\ln L\left(\hat{\theta}\right) + 2C_1\left(\operatorname{cov}\left(\hat{\theta}\right)_{Misspec}\right) \\ &= 2n\ln(n-1) + 2n\ln\left(\hat{h}\right) - 2\sum_{i=1}^{n}\ln\left[\sum_{j\neq i}^{n} K\left(\frac{x_i - x_j}{\hat{h}}\right)\right] + 2C_1\left(Cov\left(\hat{\theta}\right)_{Misspec}\right), \end{aligned} \tag{5.9}$$

where the covariance matrix of $\hat{\theta}$ is

$$Cov\left(\hat{\theta}\right)_{Misspec} = \hat{F}_{\hat{f}}^{-1}\hat{R}\hat{F}_{\hat{f}}^{-1} \,. \tag{5.10}$$

$\hat{F}_{\hat{f}}^{-1}$ are the inverse fisher information estimation $\hat{F}_{\hat{f}}^{-1}$ and $\hat{R}$ is the estimated outer-product form of the Fisher information. The $C_1(\bullet)$ information complexity is defined by

$$C_1\left(Cov(\hat{\theta})_{Mispec}\right) = \frac{s}{2}\ln\left[\frac{tr\left(Cov(\hat{\theta})_{Mispec}\right)}{s}\right] - \frac{1}{2}\ln\left|Cov(\hat{\theta})_{Mispec}\right|, \tag{5.11}$$

where $s = rank\left(Cov(\hat{\theta})_{Mispec}\right)$.

For comparison, AIC for kernel estimation is also given by

$$\begin{aligned} AIC(Kernel) &= -2\ln L(\hat{\theta}) + 2m \\ &= 2n\ln(n-1) + 2n\ln((\hat{h}) - 2\sum_{i=1}^{n}\ln\left[\sum_{j\neq i}^{n} K\left(\frac{x_i - x_j}{\hat{h}}\right)\right] + 2(3) \end{aligned}. \tag{5.12}$$

ICOMP has the following advantages. First, it allows the measurement of dependency between the random variables. Secondly, it establishes and provides a trade-off between the fit and the interaction of the parameter estimates and the interaction of the residuals of a model via the measure of complexity of their respective covariance. Third, ICOMP remove from the researcher any need to consider the parameter dimension explicitly. Since the bias in AIC is approximated by the number of parameters which is constant and has no variability, and forth, ICOMP provides a more judicious penalty term than AIC, or AIC-type criteria to balance the overfitting and underfitting risks of a model. Last but not least, ICOMP has the form for misspecification, which is very useful for the data that is not guaranteed in Gaussian distribution.

To illustrate the difference between the estimation results by both AMISE and proposed ICOMP methods, the estimated smoothing parameters by both AMISE and ICOMP optimization for each wavelength from 480nm to 720nm at 20nm increment are presented for both genuine and imposter sets from an outdoor dataset in Figure 5.9. The selected parameters *h*, for some wavelengths are different and some have the same values. For example, for band 480nm, ICOMP (red lines) selected a smaller bandwidth for genuine set than AMISE(black lines) , which means ICOMP preserves more details and obtains less smooth estimation than AMISE. This is clearly illustrated in Figure 5.10 (a) and (b) by the blue lines which indicate genuine sets. On the other hands, ICOMP selected a bigger smoothing parameter for imposter set than AMISE from Figure 5.9(b). Therefore, the estimated PDFs of the imposter sets (green lines) in Figure 5.10 by AMISE is under-fitted compared to the ICOMP method.

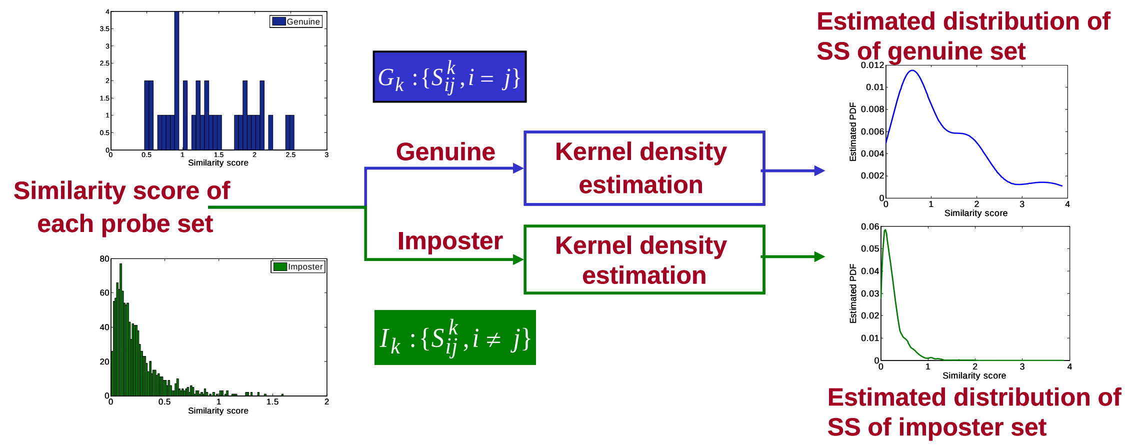

Figure 5.8. Illustration of the probability density estimation by kernel density estimation from discrete similarity scores of a certain probe set.

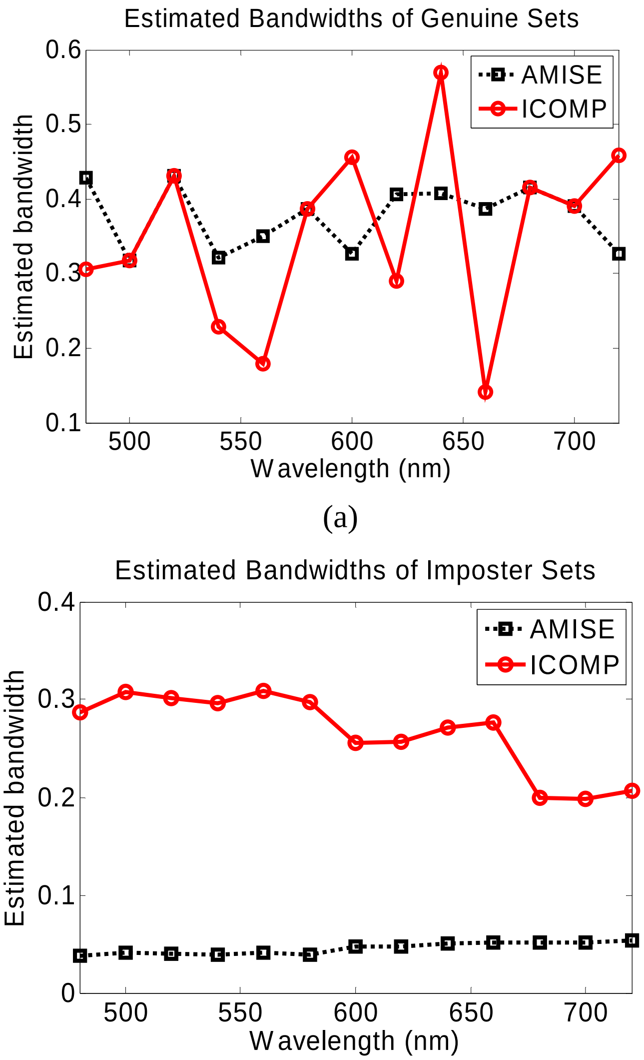

(a)

(b)

Figure 5.9. Estimated smoothing parameters by AMISE and ICOMP of (a) genuine sets and (b) imposter sets. The similarity scores are obtained from the following image sets: gallery under halogen and probes under daylight.

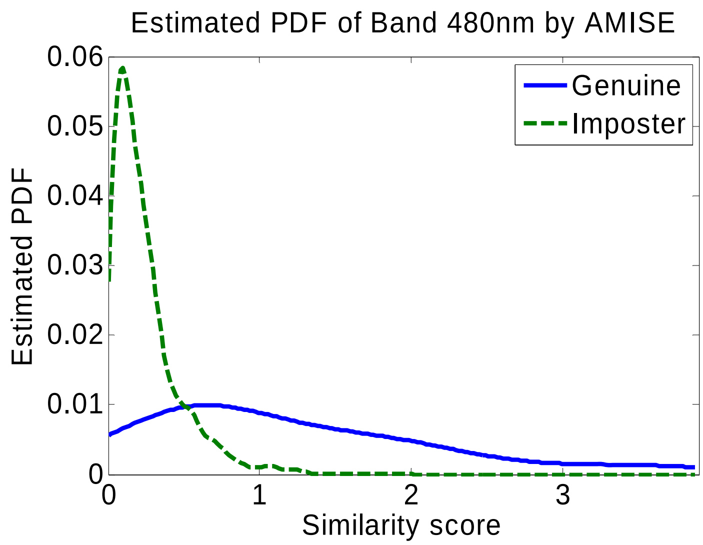

(a)

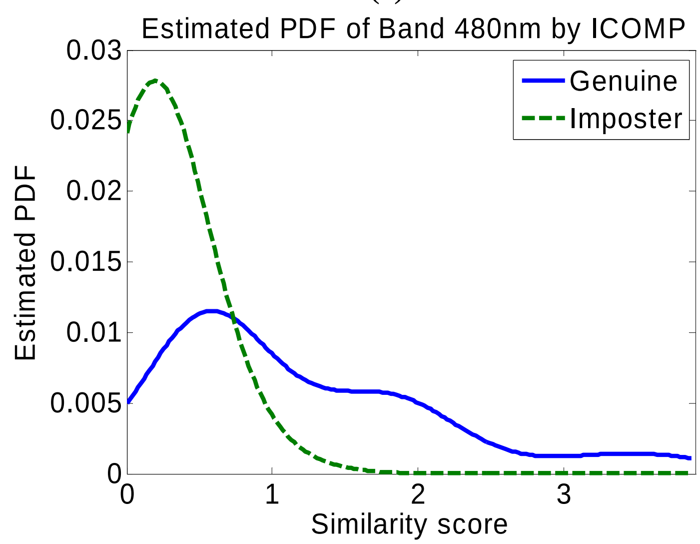

(b)

Figure 5.10. (a) Estimated PDFs by AMISE of genuine and imposter sets at band 480nm, and (b) the estimated PDFs by ICOMP of the same genuine and imposter sets at band 480nm.

5.3.3 Probabilistic distance measure

Once the PDFs of the similarity scores from genuine and imposter sets are estimated, the remaining question is how to describe the distance between the two PDFs. Probabilistic distance measures (or probabilistic distance in short) (PDM) is used here to measure the similarity between the genuine and imposter sets. Probabilistic distance measures have been used in many research areas such as probability and statistics, pattern recognition, information theory, communication and so on. In pattern recognition, pattern separability is usually evaluated using probabilistic distance measures, such as Chernoff or Bhattacharyya distances because they provide bounds for probability of error. In information theory, mutual information, a special case of Kullback-Leibler (KL) divergence or relative entropy is a fundamental quantity related to channel capacity [Zhou06]**.** Let Ω denote the space of interest. Consider a two-class problem and suppose that class 1 has the density $p_1(x)$ and class 2, $p_2(x)$, both defined on R^d. Table 5.2 [Zhou06] defines a list of probabilistic distance measures often found in the literature. The above listed distances have the following relationships [Zhou06].

(1) The Bhattacharyya distance is a special case of the Chernoff distance with $\alpha_1 = \alpha_2 = 1/2$

(2) The Matusita distance, is related to the Bhattacharyya distance as following

$$J_T = \{2[1 - \exp(-J_B)]\}^{1/2}$$

(3) The relationship between Kullback-Leibler divergence (KL) and Jeffrey divergence (symmetric version of KL) is that

$$J_D(p_1, p_2) = J_R(p_1 \| p_2) + J_R(p_2 \| p_1)$$

(4) The Kolmogorov distance is a special case of the Lissack-Fu distance with $\alpha_1 = 1$.

5.3.4 Band selection

Total number of multispectral bands is N_B and that λ_k denotes the central wavelength of the k^{th} band. The complete set of multispectral bands is $B = \{\lambda_k \mid k = 1, ..., N_B\}$. The spectral selection goal is find a subset $B_{opt} \subset B$ such that $B_{opt} = \{\lambda_k \mid rank(J_k) \le N_{opt}\}$, where N_{opt} is the number of bands to be selected and $rank(J_k)$ returns k' if J_k is the $(k')^{th}$ largest separation measure.

As a summary of the technical approach, the flow chart of the distance-based algorithm is given in Figure 5.11.

5.4 Experimental results

In this section, we study the proposed distance measure results via variety of choices of kernels, smoothing parameter, and distance measures. Four experiments are designed to

Table 5.2. List of probabilistic distance and their definitions, where $0 < \alpha_1, \alpha_2 < 1$, $\alpha_1 + \alpha_2 = 1$, and π_1 and π_2 are prior probabilities of the classes 1 and 2, respectively.

Distance Type	Definition
Bhattacharyya distance[Bhattacharyya43]	$J_B(p_1, p_2) = -\log\left\{\int_X [p_1(x)p_2(x)]^{1/2} dx\right\}$
Chernoff distance [Chernoff52]	$J_c(p_1, p_2) = -\log\left\{\int_X p_1^{\alpha_2}(x)p_2^{\alpha_1}(x)dx\right\}$
KL divergence [Cover91] [Rubner00]	$J_{KL}(p_1 \parallel p_2) = \int_X \hat{p}_1(x)\log\frac{\hat{p}_1(x)}{\hat{p}_2(x)}dx$
Jeffrey divergence/ Symmetric KL divergence [Cover91] [Kullback97]	$J_J = \int [p_1(x) - p_2(x)]\log\frac{p_1(x)}{p_2(x)}dx$
Matusita distance [Matusita55]	$J_T(p_1, p_2) = \left\{\int_X \left[\sqrt{p_1(x)} - \sqrt{p_1(x)}\right]^2 dx\right\}^{1/2}$
Patrick-Fisher distance [Patrick69]	$J_P(p_1, p_2) = \left\{\int_X [p_1(x)\pi_1 - p_2(x)\pi_2]^2 dx\right\}^{1/2}$
Lissack-Fu distance[Lissack76]	$J_L = \int_X \lvert p_1(x)\pi_1 - p_2(x)\pi_2\rvert^{\alpha_1}[p_1(x)\pi_1 + p_2(x)\pi_2]^{\alpha_2} dx$
Kolmgorov distance [Adhikara59]	$J_K(p_1, p_2) = \int_X \lvert p_1(x)\pi_1 - p_2(x)\pi_2\rvert dx$

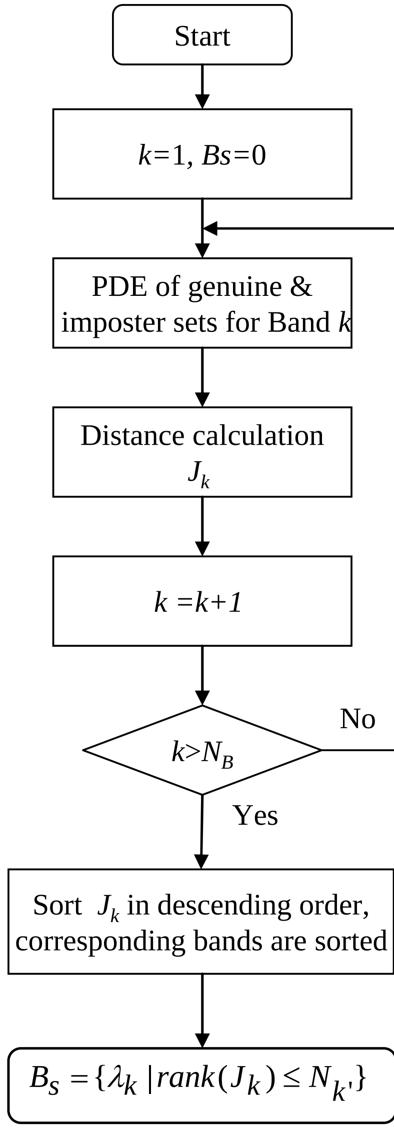

Figure 5.11. The flow chart of the distance-based band selection algorithm.

test the robustness of this method. The distance values of each and every band probe set of 35 samples are obtained and then normalized to [0, 1] for comparison purpose. Suppose D_K is a vector that contains the distance measure values of all the available bands. The normalization is given by

$$ND_k = \frac{D_k}{\max(D_k)}\,. \tag{5.13}$$

5.4.1 Fluorescent gallery, halogen probe

In this experiment, the spectral bands of multispectral face images under halogen light is selected via proposed algorithm while gallery images are under another indoor lighting, fluorescent light. There are 25 sets of probe images are involved in the selection. They are sub-spectral narrow-band images between wavelength 480nm and 720nm with increment of 10nm.

First, we investigate the ranking results via various distance measures of 25 bands with the same kernel and the same smoothing parameter. In Figure 5.12(a), the normalized probability distance by four different distance measures are given with Gaussian kernel and smoothing parameter obtained by AMISE. Even though the distances show various values at certain wavelength, the trends and ranking results from largest distance values to smallest distance values are clearly similar. For example, the top one band is 610 or 620nm for all the tested kernels and distance measures. The distances at lower wavelengths are smaller than those from 600nm which means the separation between the imposter and genuine sets at lower wavelengths are not as large as the separation at 600nm. In Figure 5.12(b), we see the similar ranking results by cosine kernel with Gaussian kernel. Secondly, ranking results via distance measures for different kernels also show similar or same ranking results, which are demonstrated in Figure 5.12 (a) and (b).

Thirdly, the ranking of bands via different smoothing parameters also have similar results. For example, probability distance values of four different distance measures via optimization of smoothing parameters by ICOMP are shown in Figure 5.13 (a) and (b). Therefore, it is concluded that the ranking results of bands are very robust to each and every free parameters, including kernel types, smoothing parameter and distance measures. Since the ranking of the normalized distances for different wavelengths via different kernels and distance measures are the same or very similar, only the top three bands are given in the Table 5.3 - 5.5, each of which shows the selected bands with corresponding distance measures, kernel types and via AMISE, AIC and ICOMP, separately. Three distance measures out of four, that is 75% of all these combinations, selected (610, 630, 640) for the top three bands. Minority selected (610, 620, 640). The recognition rate for (610, 630, 640) and (610, 620, 640) are the same at 97.17%.

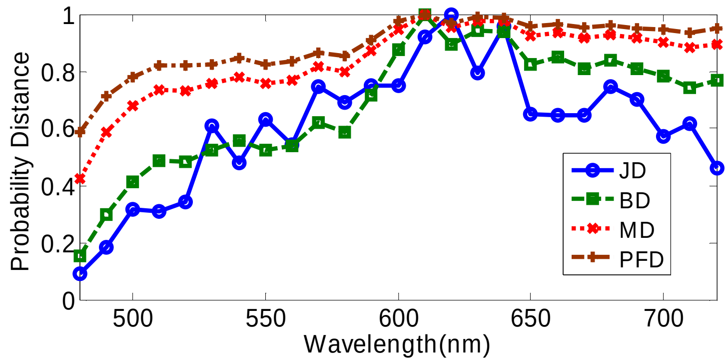

(a)

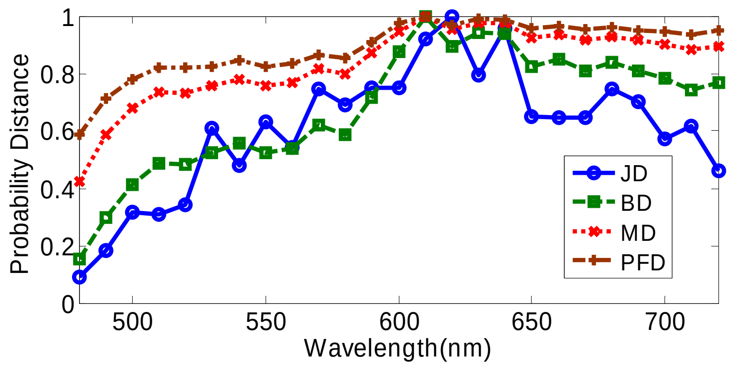

(b)

Figure 5.12. Normalized probability distances along visible spectrum by four different distance measures, Jeffery divergence, Bhattacharyya distance, Matusita distance, Patrick-Fisher distance, are given with (a) Gaussian kernel and (b) Cosine kernel and smoothing parameter obtained by AMISE.

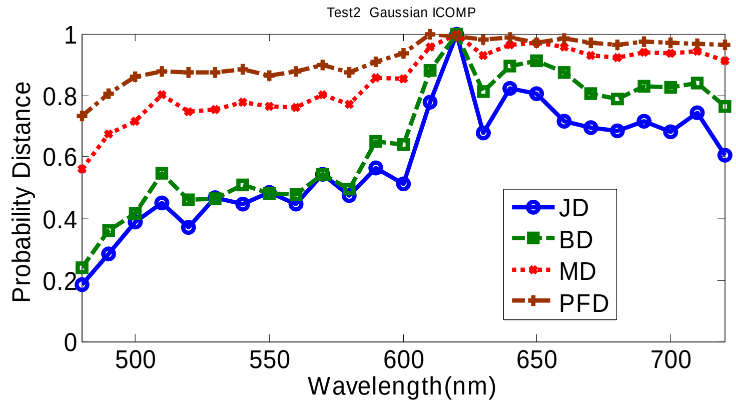

(a)

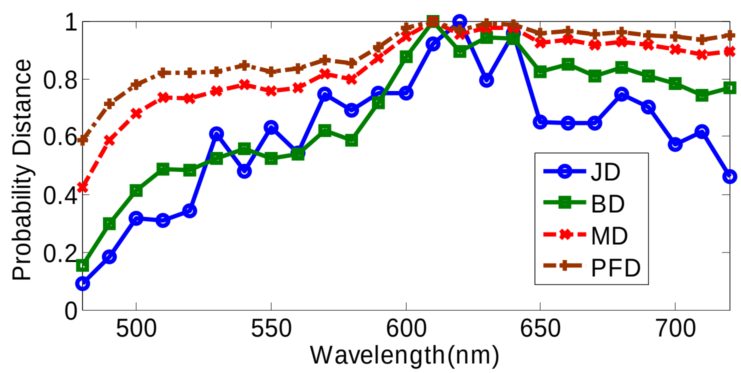

(b)

Figure 5.13. Normalized probability distances along visible spectrum by four different distance measures, Jeffery divergence, Bhattacharyya distance, Matusita distance, Patrick-Fisher distance, are given with (a) Gaussian kernel and (b) Cosine kernel and smoothing parameter obtained by ICOMP.

Table 5.3. The top three bands selected by different distance measures with four different kernels with the smoothing parameter defined by AMISE method in experiment 5.4.1.

	Gaussian Kernel	Triangle Kernel	Epanechnikov Kernel	Cosine Kernel
Jeffrey Divergence	610 620 640	610 620 640	610 620 640	610 620 640
Bhattacharyya Distance	610 630 640	610 630 640	610 630 640	610 630 640
Matusita Distance	610 630 640	610 630 640	610 630 640	610 630 640
Patrick-Fisher Distance	610 630 640	610 630 640	610 630 640	610 630 640

Table 5.4. The top three bands selected by different distance measures with four different kernels with the smoothing parameter obtained by AIC in experiment 5.4.1.

	Gaussian Kernel	Triangle Kernel	Epanechnikov Kernel	Cosine Kernel
Jeffrey Divergence	610 620 640	610 620 640	610 620 640	610 620 640
Bhattacharyya Distance	610 630 640	610 630 640	610 630 640	610 630 640
Matusita Distance	610 630 640	610 630 640	610 630 640	610 630 640
Patrick-Fisher Distance	610 630 640	610 630 640	610 630 640	610 630 640

Table 5.5. The top three bands selected by different distance measures with four different kernels with the smoothing parameter optimized by ICOMP in experiment 5.4.1.

	Gaussian Kernel	Triangle Kernel	Epanechnikov Kernel	Cosine Kernel
Jeffrey Divergence	610 620 640	610 620 640	610 620 640	610 620 640
Bhattacharyya Distance	610 630 640	610 630 640	610 630 640	610 630 640
Matusita Distance	620 630 640	610 630 640	610 630 640	610 630 640
Patrick-Fisher Distance	610 620 640	610 630 640	610 630 640	610 630 640

5.4.2 Daylight gallery, halogen probe

In this experiment, gallery images are acquired under daylight and probes are acquired under halogen light. The top three bands of multispectral face images in the range of 480nm to 720nm under halogen light are selected via four different distance measures.

The ranking results from four different kernels with smoothing parameters defined by AMISE, AIC and ICOMP are given in Table 5.6, 5.7 and 5.8. 78% of all the combinations selected the top three bands (600, 610, 620).

The minority selected results are also studied and compared and we found majority results are the best approach in the case of difference in results. For example, one of the minority results is (510, 530, 570) via AMISE method and Gaussian kernel. The fused images from (510, 530, 570) provides worse performance (60%) than that (62.86%) of fusion of (600, 610, 620) from recognition engine results.

5.4.3 Fluorescent gallery, daylight probe

In this experiment, the most challenging lighting condition, daylight, is investigated for probe sets. To simulate practical face recognition, stable indoor fluorescent light is used for gallery images while all the probes are acquired under varying daylight. The spectral range is selected among 13 sets of narrow-band spectral images from wavelength 480nm to 720nm with the increment of 20nm.

Because the ranked bands via our distance-based band selection are the very similar with different kernels, smoothing parameters and distance measures, only the top three ranked bands via four different distance measures and four different kernels with smoothing parameters defined by AMISE, AIC and ICOMP are given in Table 5.9 to 5.11. 100% of all the listed combination of parameters selected the same three bands (640, 680, 720).

5.4.4 Halogen gallery, daylight probe

In this experiment, halogen light is used for gallery images and outdoor daylight images are used as probes. The spectral range is selected among 13 sets of narrow-band spectral images from wavelength 480nm to 720nm with the increment of 20nm.

The band with largest distance measure is 720nm. The second largest distance is for 660nm. The top three bands of multispectral face images are selected via four different distance measures and four different kernels with smoothing parameters defined by AMISE, AIC and ICOMP in Table 5.12-14. The majority votes on the top three bands are (660, 700, 720) and the fusion of these three bands are 48.57%. The minority votes are at (640, 660, 720) and the fusion results on these three bands are 42.86%. Again, we found the majority results are better than the minority.

Table 5.6. The top three bands selected by different distance measures with four different kernels with the smoothing parameter optimized by AMISE in experiment 5.4.2.

	Gaussian Kernel	Triangle Kernel	Epanechnikov Kernel	Cosine Kernel
Jeffrey Divergence	510 530 570	600 610 620	600 610 620	600 610 620
Bhattacharyya Distance	600 620 630	600 610 620	600 610 620	600 610 620
Matusita Distance	600 620 630	600 610 620	600 610 620	600 610 620
Patrick-Fisher Distance	600 620 630	600 610 620	600 610 620	600 610 620

Table 5.7. The top three bands selected by different distance measures with four different kernels with the smoothing parameter optimized by AIC in experiment 5.4.2.

	Gaussian Kernel	Triangle Kernel	Epanechnikov Kernel	Cosine Kernel
Jeffrey Divergence	510 530 570	600 610 620	600 610 620	600 610 620
Bhattacharyya Distance	600 620 630	600 610 620	600 610 620	600 610 620
Matusita Distance	600 620 630	600 610 620	600 610 620	600 610 620
Patrick-Fisher Distance	600 620 630	600 610 620	600 610 620	600 610 620

Table 5.8. The top three bands selected by different distance measures with four different kernels with the smoothing parameter optimized by ICOMP in experiment 5.4.2.

	Gaussian Kernel	Triangle Kernel	Epanechnikov Kernel	Cosine Kernel
Jeffrey Divergence	600 610 620	600 610 620	600 610 620	600 610 620
Bhattacharyya Distance	600 610 620	600 610 620	600 610 620	600 610 620
Matusita Distance	600 610 620	600 610 620	600 610 620	600 610 620
Patrick-Fisher Distance	600 610 620	600 610 620	600 610 620	600 610 620

Table 5.9. The top three bands selected by different distance measures with four different kernels with the smoothing parameter optimized by AMISE in experiment 5.4.3.

	Gaussian Kernel	Triangle Kernel	Epanechnikov Kernel	Cosine Kernel
Jeffrey Divergence	640 680 720	640 680 720	640 680 720	640 680 720
Bhattacharyya Distance	640 680 720	640 680 720	640 680 720	640 680 720
Matusita Distance	640 680 720	640 680 720	640 680 720	640 680 720
Patrick-Fisher Distance	640 680 720	640 680 720	640 680 720	640 680 720

Table 5.10. The top three bands selected by different distance measures with four different kernels with the smoothing parameter optimized by AIC in experiment 5.4.3.

	Gaussian Kernel	Triangle Kernel	Epanechnikov Kernel	Cosine Kernel
Jeffrey Divergence	640 680 720	640 680 720	640 680 720	640 680 720
Bhattacharyya Distance	640 680 720	640 680 720	640 680 720	640 680 720
Matusita Distance	640 680 720	640 680 720	640 680 720	640 680 720
Patrick-Fisher Distance	640 680 720	640 680 720	640 680 720	640 680 720

Table 5.11. The top three bands selected by different distance measures with four different kernels with the smoothing parameter optimized by ICOMP in experiment 5.4.3.

	Gaussian Kernel	Triangle Kernel	Epanechnikov Kernel	Cosine Kernel
Jeffrey Divergence	640 680 720	640 680 720	640 680 720	640 680 720
Bhattacharyya Distance	640 680 720	640 680 720	640 680 720	640 680 720
Matusita Distance	640 680 720	640 680 720	640 680 720	640 680 720
Patrick-Fisher Distance	640 680 720	640 680 720	640 680 720	640 680 720

Table 5.12. The top three bands selected by different distance measures with four different kernels with the smoothing parameter optimized by AMISE in experiment 5.4.4.

	Gaussian Kernel	Triangle Kernel	Epanechnikov Kernel	Cosine Kernel
Jeffrey Divergence	640 660 720	660 700 720	660 700 720	660 700 720
Bhattacharyya Distance	640 660 720	660 700 720	660 700 720	660 700 720
Matusita Distance	640 660 720	660 700 720	660 700 720	660 700 720
Patrick-Fisher Distance	640 660 720	660 700 720	660 700 720	660 700 720

Table 5.13. The top three bands selected by different distance measures with four different kernels with the smoothing parameter optimized by AIC in experiment 5.4.4.

	Gaussian Kernel	Triangle Kernel	Epanechnikov Kernel	Cosine Kernel
Jeffrey Divergence	640 660 720	660 700 720	660 700 720	660 700 720
Bhattacharyya Distance	640 660 720	660 700 720	660 700 720	660 700 720
Matusita Distance	640 660 720	660 700 720	660 700 720	660 700 720
Patrick-Fisher Distance	640 660 720	660 700 720	660 700 720	660 700 720

Table 5.14. The top three bands selected by different distance measures with four different kernels with the smoothing parameter optimized by ICOMP in experiment 5.4.4.

	Gaussian Kernel	Triangle Kernel	Epanechnikov Kernel	Cosine Kernel
Jeffrey Divergence	640 660 720	660 700 720	660 700 720	660 700 720
Bhattacharyya Distance	640 660 720	660 700 720	660 700 720	660 700 720
Matusita Distance	640 660 720	660 700 720	660 700 720	660 700 720
Patrick-Fisher Distance	640 660 720	660 700 720	660 700 720	660 700 720

5.5 Summary

Distance-based band selection method was proposed for multispectral face recognition. This method provided a new quantitative performance evaluation metric of each band and ranked the bands according to the face recognition performance. It is comprised of three main steps, kernel density estimation, distance measure and band selection via ranking in descending order. In kernel estimation, the smoothing parameter is optimized by information complexity criterion. From four experiments, we conclude that the majority selection results are most accurate. Table 5.15 gives the majority voted on the top one, two, and three ranked bands. From real data in four experiments, it is observed that ranked bands or candidates have an extremely stable selection results even with different kernels and distance measures. This observation proved the robustness of distance-based band selection. The performance comparison with conventional images will be presented in Chapter 6.

Table 5.15. The top three ranked bands in four experiments.

Experiment	Illumination		Top 1 choice	Top 2 choice	Top 3 choices
	Gallery	Probe			
1	Fluorescent	Halogen	610	610, 640	610 640 630
2	Daylight	Halogen	610	610, 620	610 620 600
3	Fluorescent	Daylight	720	720, 680	720 680 640
4	Halogen	Daylight	720	720, 660	720 660 700

6 Complexity-guided distance-based band selection

In previous chapter, all available bands are ranked in a descending order as the band selection candidates in distance-based band selection. However, the optimal number of selected bands has not been decided yet. In this chapter, a new automatic band selection method which employs a powerful selection criterion to find the optimal number of bands based on the already ranked bands, named complexity-guided distance-based band selection (CDBS) is proposed and described. It employs information complexity in the fashion of multivariate kernel estimation. This method provides a practical and efficient spectral band selection for improving face recognition performance under illumination variations.

The motivation of the new algorithm is given in section 6.1 and the proposed technical approach is described in section 6.2. Experimental results from both simulated data and real data for verification of proposed band selection approaches are presented in section 6.3. Summary is given in section 6.4.

6.1 Motivations

In distance-based band selection algorithm, the distance between the genuine and imposter sets for each studied band/wavelength is calculated and ranked. According to the characteristics of the distance, the band/wavelength with the largest distance has a better chance to outperform other bands and also conventional images as long as using the same recognition engine. The experimental results have shown that distance-based band selection method is very stable in terms of the three main free parameters, including distance measure, smoothing parameter, and kernel types in kernel estimation. Therefore, the ranked bands by distance measure are selected candidates with a high confidence. However, the question of how many bands are sufficient for face recognition performance evaluation has not been answered. Therefore, the effort in this chapter is to answer the question that how many spectral band images are sufficient for improved face recognition other than all the available bands.

With the same gallery images, different band probe sets have the different genuine similarity scores. It is reasonable and intuitive to assume that similar distributions of the genuine sets of different probes give the similar image information and therefore similar recognition rates shall be obtained from the corresponding probes. For example, if the estimated genuine distribution of band *k*, $\hat{p}_{G,k}(x)$, has the similar distribution with band *k*+1, $\hat{p}_{G,k+1}(x)$, band *k* and band *k+1* must have very similar recognition performance by the same recognition engine. Therefore, one of these two bands is the redundancy information and should be dropped out without loosing useful information. Therefore, considering this high correlation and similarity between neighbor bands is the best way of reducing redundancy. Figure 6.1 gives an illustration of the distributions of genuine sets of seven band images under daylight given the illuminations for gallery and probes. The distribution of Band 720nm shows more similarity to that of Band 680nm than that of band 480nm. Therefore, from band correlation and redundancy point of view, selection results should be (480, 720) rather than (680, 720). On the other hand, with the distance measure results as another factor in mind, shown in Figure 6.1 (b), band (680, 720) with the black and yellow circle highlighted should be our choices. Therefore, we are facing the trade-off between the distance measure results which can select very close bands and the correlation between bands which brings the tendency of selecting the bands are further away.

The proposed solution of calculating the balance between the dependency among neighbor bands and the ranked distance measure is a complexity measuring tool. Information complexity (ICOMP) is brought into our attention again for its most advanced and accurate model selection power.

Let the total number of multispectral bands be N_B and λ_k denote the central wavelength of the k^{th} band. The complete set of multispectral bands is $B = \{\lambda_k \mid k = 1,..., N_B\}$. The proposed method automatically finds an optimal subset $B_{opt} \subset B$ such that the fused images from B_{opt} can outperform conventional broad-band images.

6.2 Technical approach

Our goal is to search for the least number of bands which contain least information redundancy and to find smallest subset that can sufficiently represent the whole stack of spectral images. Continuing the work on distance-based band selection, a model selection

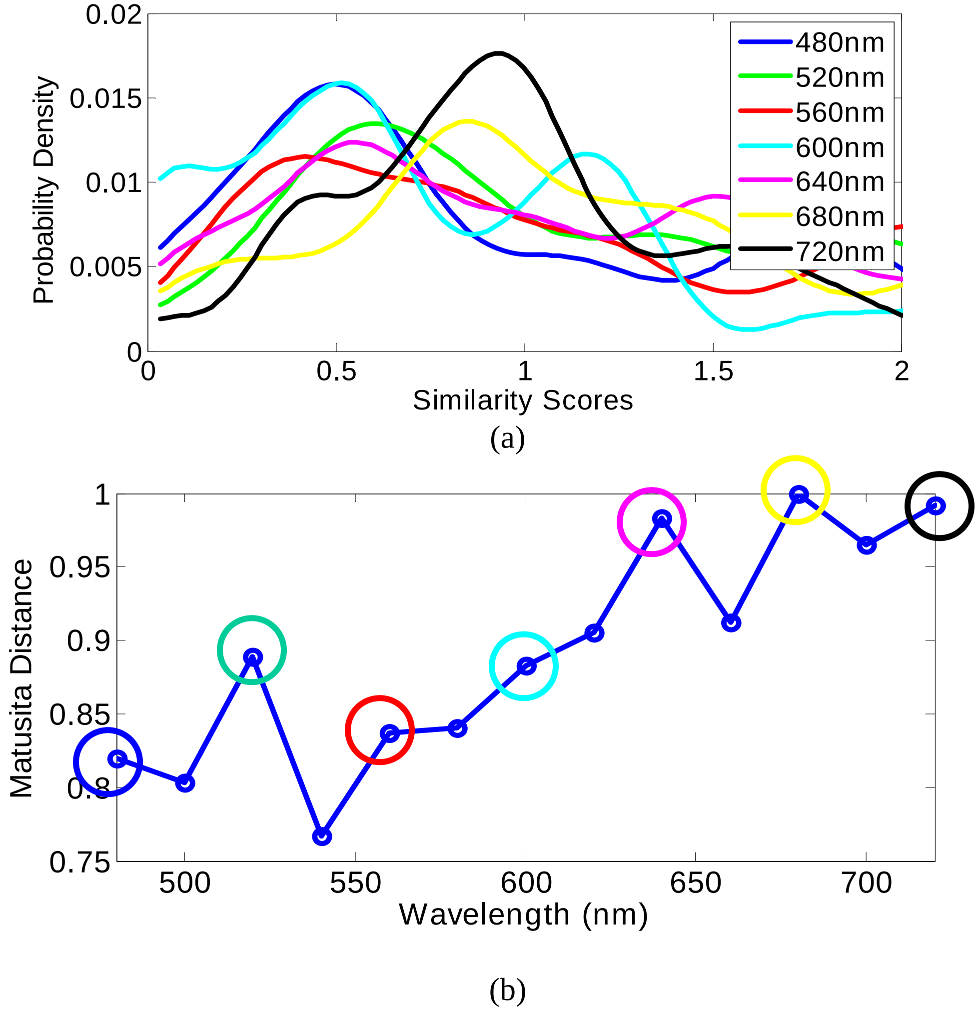

Figure 6.1. (a) The similarity scores of seven bands in one set of experiments (Gallery, fluorescent light, Probes, daylight) (b). The distance measure results by ICOMP estimation and Cosine kernel.

criterion by complexity calculation is the key to our new method.

In this section, the proposed algorithm is first described in block diagram and flow chart in section 6.2.1. Since the first three steps are the same to distance-based band selection algorithm, we only emphasize the criterion calculation in section 6.2.2.

6.2.1 Block diagram

The block diagram of the complexity-guided distance-based band selection is given in Figure 6.2. The flow chart of this algorithm is given in Figure 6.3. First, the similarity scores of genuine and imposter sets of each probe set are estimated. Second, the distance measure is conducted on these two distributions. Thirdly, all the narrow-band probe sets are ranked in a descending order. Last but not least, the criterion is calculated to choose the optimal number of bands.

6.2.2 Criterion calculation

The criterion calculation is carried out in the format of the multivariate model selection of Information Complexity (ICOMP) with penalty on covariance between bands. In this format, we have considered both distance ranking results which indicate the recognition performance and the dependency/correlation among the bands. The main process is the multivariate kernel estimation on the similarity scores of the ranked bands.

Consider a p-dimensional random vector $\mathbf{x} = (\mathbf{x}_1, \cdots, \mathbf{x}_p)'$ and there are total of n observations. Then, the i^{th} observation of each of the p random variables in the vector $\mathbf{x}_i$

$$\mathbf{x}_i = \begin{bmatrix} x_{i1} \\ \vdots \\ x_{in} \end{bmatrix}, \tag{6.1}$$

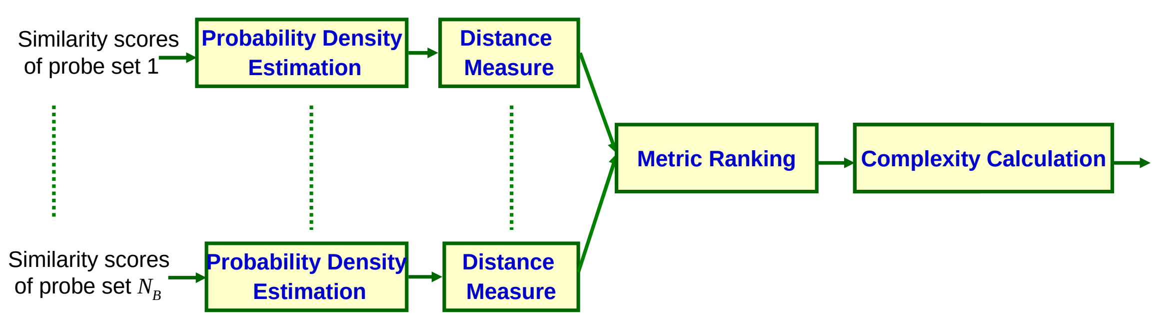

Figure 6.2. Block diagram of complexity guided distance-based band selection.

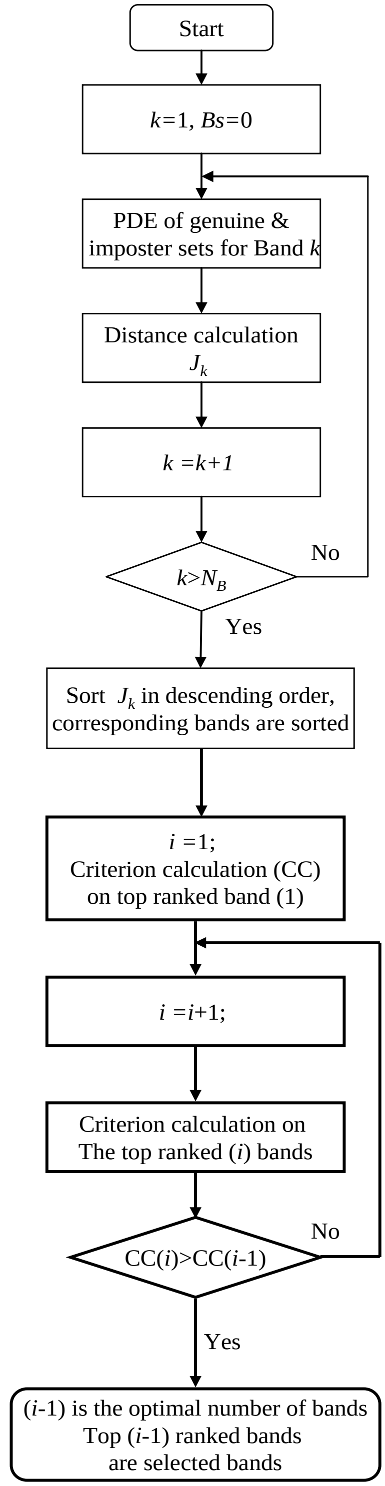

Figure 6.3. Flow-chart of the complexity-guided distance-based band selection algorithm.

where $i=1,\ldots,n$. x_{ij} is the i^{th} observation of the random variable $\mathbf{x}_j$. The goal is to estimate the probability density of $\mathbf{x} = (\mathbf{x}_1,\cdots,\mathbf{x}_p)'$, which is the joint probability density function of the random variables

$$f(\mathbf{x}) = f(\mathbf{x}_1,\cdots,\mathbf{x}_p). \tag{6.2}$$

The general form of the kernel estimator of $f(\mathbf{x})$ [Wang93] is

$$\hat{f}_H(\mathbf{x}) = \frac{1}{n}\sum_{i=1}^{n}\mathbf{K}_H(\mathbf{x}-\mathbf{x}_i), \tag{6.3}$$

where $\boldsymbol{K}$(.) is a multivariate kernel density function, and H is a symmetric positive definite p x p matrix known as the bandwidth/smoothing parameter matrix. The sample point estimator has superior performance relative to kernel density estimators in which the variable bandwidth is associated with the center of the kernel $\mathbf{x}$. From 6.3, we have

$$\hat{f}_H(\mathbf{x}) = \frac{1}{n(2\pi)^{(p/2)}}\sum_{i=1}^{n}|H_i|^{-1/2}\mathbf{K}\left\{(\mathbf{x}-\mathbf{x}_i)' H_i^{-1}(\mathbf{x}-\mathbf{x}_i)\right\}. \tag{6.4}$$

The bandwidth matrix can be restricted to a class of positive definite diagonal matrices, and then the corresponding kernel function is known as a product kernel

$$\hat{f}(x) = \frac{1}{n}\sum_{i=1}^{n}\left\{\prod_{j=1}^{p}\frac{1}{h_j}\mathbf{K}\left(\frac{x_j - x_{ij}}{h_j}\right)\right\}. \tag{6.5}$$

For example, in the bivariate case, the representation of the KDE $\hat{f}(x_1, x_2)$, depends, in general on the 2 by 2 diagonal bandwidth matrix

$$H = \begin{bmatrix} h_1^2 & 0 \\ 0 & h_2^2 \end{bmatrix}, \tag{6.6}$$

and it is given by

$$\hat{f}(x_1, x_2) = \frac{1}{n}\sum_{i=1}^{n}\frac{1}{h_1}\frac{1}{h_2}\mathbf{K}\left(\frac{x_1 - X_{i1}}{h_1}\right)\mathbf{K}\left(\frac{x_2 - X_{i2}}{h_2}\right), \tag{6.7}$$

where h_1 and h_2 are the window widths in the X_1 and X_2 directions.

For the multivariate kernel density estimator, AMISE is given by

$$H_{AMISE} = \frac{1}{4}\mu_2^2(\mathbf{K})\int\left[tr\left\{H'\mathbf{H}_g(x)H\right\}\right]^2 dx + \frac{1}{n\det(H)}\|\mathbf{K}\|_2^2, \tag{6.8}$$

where H=bandwidth matrix, $\mu_2^2(\mathbf{K})$=the 2nd moment of **K,** $\mathbf{H}_g$ =Hessian matrix, and $\|\mathbf{K}\|_2^2$ =p-dimensional squared L^2-norm of **K**, *i.e.*, $\int\{\mathbf{K}(x)\}^2 dx$.

The simplest case, H and Σ are considered to be diagonal matrices

$$H = diag(h_1,\cdots,h_p) \text{ and } \Sigma = diag(\sigma_1^2,\cdots\sigma_p^2), \tag{6.9}$$

and this leads to

$$\hat{h}_j^* = \left(\frac{4}{p+2}\right)^{1/(p+4)} n^{-1/(p+4)}\hat{\sigma}_j, \tag{6.10}$$

for $j = 1,\cdots,p$ where $\hat{\sigma}_j = C_1(\hat{\Sigma}) = \left(\frac{p}{2}\right)\log\left[tr(\hat{\Sigma})/p\right] - \frac{1}{2}\log\left[\det(\hat{\Sigma})\right]$. $\hat{\sigma}_j$ is the entropic complexity of the estimated covariance matrix and where p is the rank of $\hat{\Sigma}$.

Estimating of bandwidth h_j^* using ICOMP can be presented by

$$ICOMP = -2\log L(x_1,\cdots,x_n \mid H) + 2C_{1F}(\hat{\Sigma}), \tag{6.11}$$

where

$$C_{1F}(\hat{\Sigma}) = \frac{s}{4}\frac{C_F(\hat{\Sigma})}{\left(\frac{tr(\hat{\Sigma})}{s}\right)^2}, \tag{6.12}$$

is the second order equivalent measure of complexity to the original $C_1(\bullet)$ measure and

$$\log L(x_1,\cdots,x_n \mid H) = \sum_{i=1}^{n}\log\hat{f}_{H,(-i)}(x_i), \tag{6.13}$$

where $\hat{f}_{H,(-i)}$ is the leave-one-out estimator

$$\hat{f}_{H,(-i)}(x_i) = \frac{1}{n-1}\sum_{\substack{i=1 \\ j\neq 1}}^{n}|H|^{-1/2}\mathbf{K}\left\{H^{-1/2}(\mathbf{x}_i - \mathbf{x}_j)\right\}. \tag{6.14}$$

Since it is hard to visualize a high dimensional kernel density function, a 2-D kernel density function is plotted as an illustration in Figure 6.4. The 2-D information comes from the genuine sets of the band 480nm and band 500nm under daylight. X-axis and Y-axis are the similarity scores for both bands and the Z-axis is the estimated PDF by multivariate kernel form of ICOMP.

In complexity-guided distance-based band selection, the well-ranked bands are automatically selected by model selection criterion, ICOMP, in the format of multivariate kernel estimation. Comparing to the distance-based band selection, this algorithm employed model selection criterion to automatically determine the optimal number of bands with the penalty of the covariance among different bands. The selection result is a trade-off between the two factors, the dependency among bands and the individual performance of each band ranked by the distance measure. In a word, the new automatic band selection method can provide a smart stop criterion provided with the top ranked bands in previous chapter.

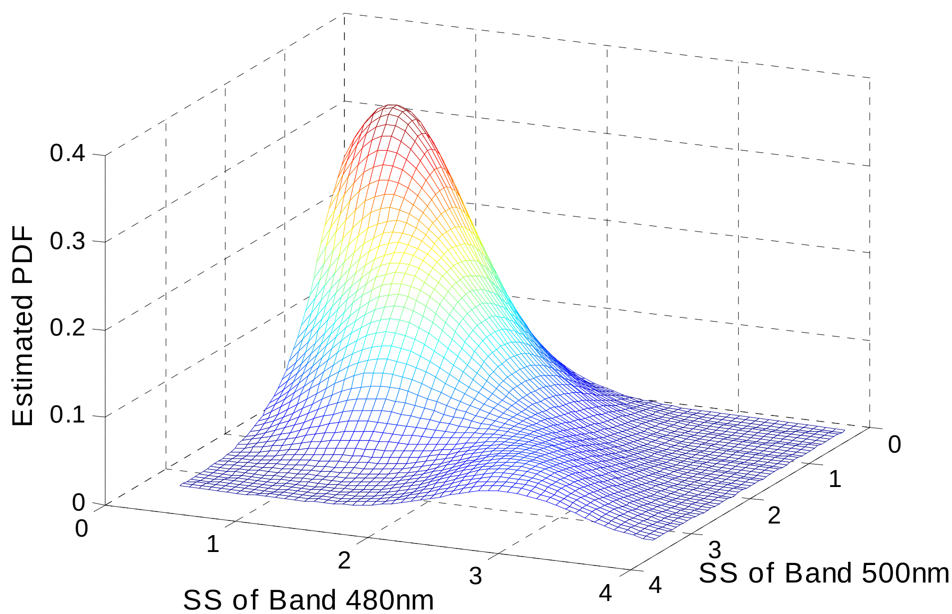

Figure 6.4. Illustration of 2-D kernel density function (from the genuine sets at band 480nm and 500nm, respectively, under daylight).

6.3 Experimental results

In this section, we use both simulated data and real data to verify our proposed band selection algorithms. Section 6.3.1 and 6.3.2 are the experiments using simulated data. Two independent random data sets with 500 data points, which can present the similarity scores of genuine and imposter sets respectively, are created first. We design 25 such pair of random data sets to represent the narrow-band probe sets. Therefore, the distance-based band selection and complexity-guided distance-based band selection algorithms are conducted these data and the distance measure results and criterion values are obtained. The band selection results are eventually given which verifies the accuracy of our methods.

Four experiments are designed to investigate the recognition performances of fused images from selected band/bands and conventional images from section 6.3.3 to section 6.3.6. In real world, face images are normally acquired under different lighting conditions and compared with the database images. It is reasonable and important to study the situation that the illuminations for gallery and probe images are different. Therefore, the experiments are designed according to different acquisition illuminations for gallery and probe images.

From the results of chapter 5, we learnt that different distance measures or kernels did not affect the band ranking results. Therefore, Matusita distance measure with cosine kernel with optimal smoothing parameter is used for the following experiments without any preference.

In real data experiments, similarity scores are obtained via two well-known recognition engines, Identix's FaceIt® and Cognitec's FaceVACS®. The distance values of each and every band probe set of 35 samples are obtained and then normalized to [0, 1] for comparison purpose. Before the selection of spectral ranges, a polynomial smoothing is conducted to reduce the undesired disturbances from noisy data. In addition, it becomes easier to observe the embedded trend with the smoothed data.

The spectral ranges are finally selected and the corresponding narrow-band images are fused by Haar-wavelet fusion. Wavelet based methods have been widely used toward image fusion. The Haar wavelet-based pixel-level fusion, as described in [Gonzalez04], is applied. Given the registered narrow-band images from the selected spectral range, two-dimensional discrete wavelet decomposition is performed on each image to obtain the wavelet approximation coefficients and detail coefficients. The coefficients in inverse wavelet transform for fused image are obtained by choosing the maximum among each type of coefficients. The two-dimensional discrete wavelet inverse transform is then performed to construct the fused image. The numerical measure, CMCM, is used to evaluate the recognition performance and is explained in Chapter 4.

6.3.1 Simulated data with low correlation

In this section and 6.3.2, we test our band selection algorithms via simulated data. First, we study the band selection results while there are multiple peaks. In this case, our algorithm should select the top ranked bands with relatively large distances values. For example, we are given a set of distance values as in Figure 6.5. The corresponding criterion values by ICOMP from selected only one band to all 25 bands are given in figure 6.6. As we can see, ICOMP automatically chooses three bands and they are (720, 630, 550). They are the local peaks as we expected without the band 710nm or 700nm even thought those two bands have higher distance value than band 550nm and 630nm. This selection results have shown that our algorithm smartly selected the bands and decides the number of bands with consideration of both distance values and also the correlation between the bands. Since correlation is one of the most mattering factors which affects the selection results, the covariance matrix of partial bands are presented in Figure 6.7.

Another example with four local peaks in distance measure is given in Figure 6.8. The optimal selected number is four and they are (530, 650, 710, 590). The corresponding criterion values by ICOMP are given in Figure 6.9. Our algorithms selected the top 4 ranked bands and these four bands given the minimal ICOMP value. The covariance among the bands is presented in Figure 6.10. From these two examples, it is concluded that the complexity-guided distance-based band selection can provide not only the selected bands but also the optimal number of bands.

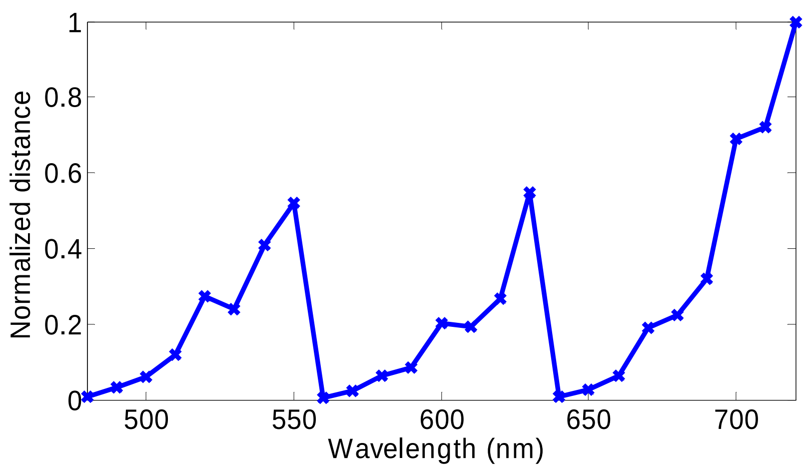

Figure 6.5. Normalized distance measure values for 25 bands with three local peaks.

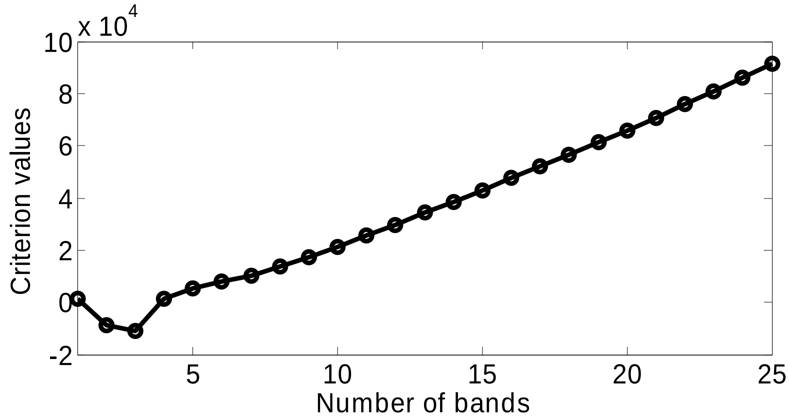

Figure 6.6. Criterion values calculated by ICOMP for different number of bands with 3 bands having the minimal value.

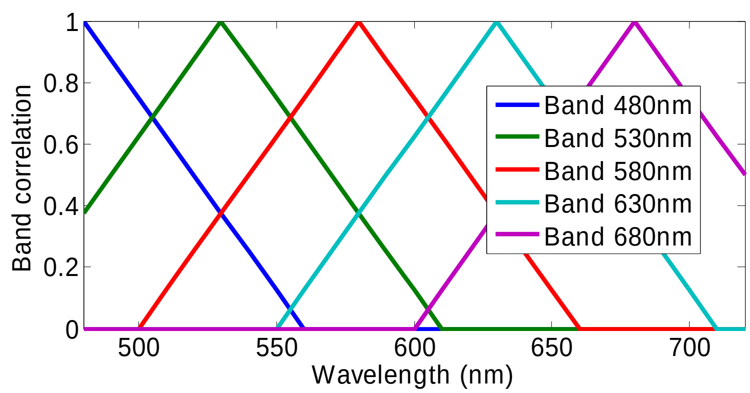

Figure 6.7. Covariance matrix of bands (480, 530, 580, 630, 680) (480nm in blue line, band 530nm in green, 580nm in red, 630nm in cyan and 680nm in purple).

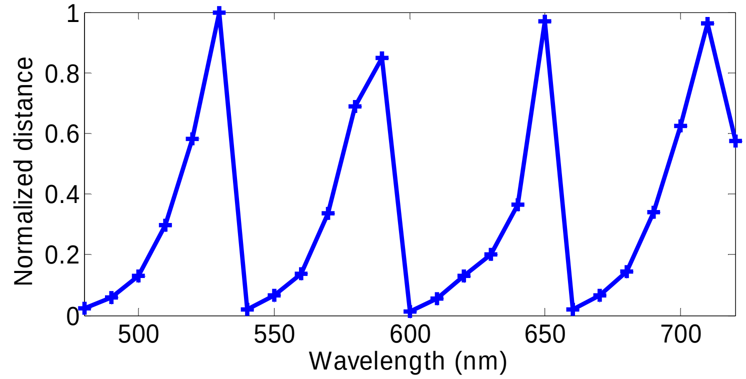

Figure 6.8. Normalized distance measure values for 25 bands with four local peaks.

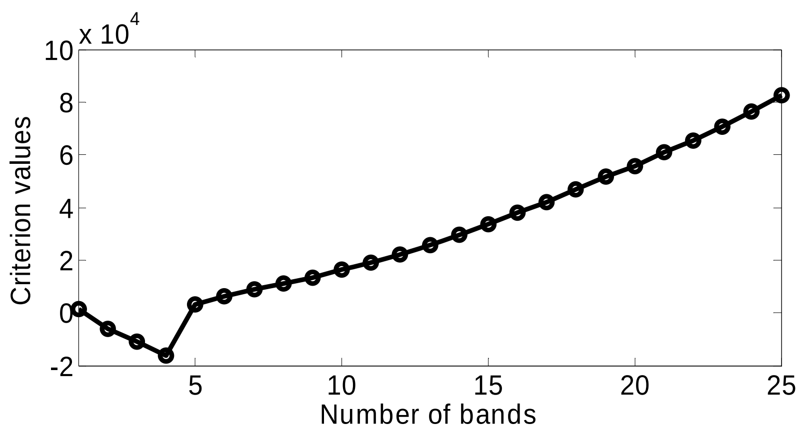

Figure 6.9. Criterion values calculated by ICOMP from different number of bands with 4 as the selected number.

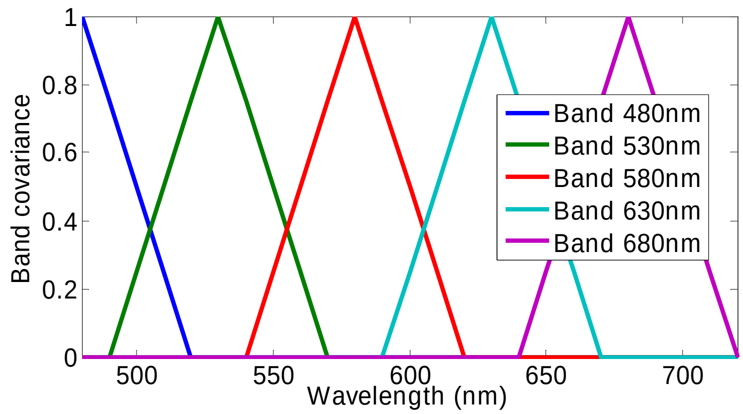

Figure 6.10. Covariance matrix of bands (480, 530, 580, 630, 680) (480nm in blue line, band 530nm in green, 580nm in red, 630nm in cyan and 680nm in purple).

6.3.2 Simulated data with high correlation

From previous section, we can see that complexity-guided distance-based band selection algorithm selected the local peaks. However, is it always true that the local peaks are our solutions and the number of peaks is our optimal number of bands? Our answer is that it is not always true. The fact is that the selection results by our algorithm are the trade-off between the covariance among bands and the ranked band candidates. It could select the neighbor bands or very further apart bands. The correlation plays an important role in the selection and the effect is given as follows. Figure 6.11 shows an independent example of the distance measure values from 25 bands, and the corresponding criterion calculations are given in Figure 6.12. This time, CDBS selected only two bands (710, 530) instead of four local peaks. This happens because the correlations of between the peak band (710) and the relatively closer peaks are highly correlated so that the closer peaks are treated as redundancy. The result is also the outcome of the relative distance measure values of among all the bands at local peaks. The correlation is given in Figure 6.13 and we can see that each band is correlated to all the neighbors except the farthest band.

Another example is given in the Figure 6. 14-15. Ranked bands are (530, 590, 710, 650, 520, 580, 700, 720, 540, 640, 500, 630, 690, 570, 620, 560, 680, 550, 490, 610, 670, 600, 540,660, 480). This time, only one band is automatically selected (530) because of the high correlation which is given in Figure 6.13.

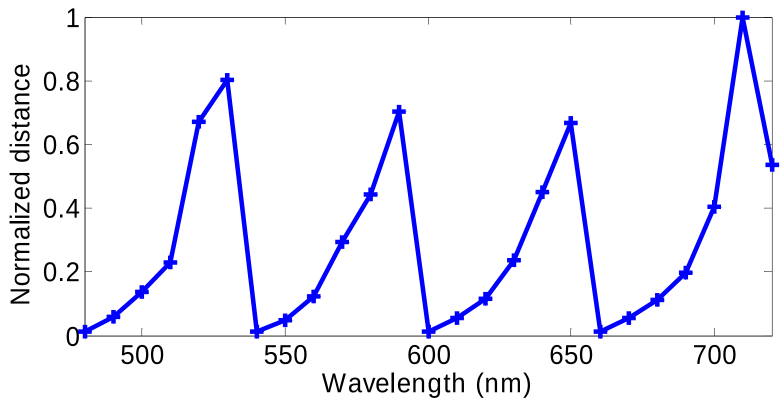

Figure 6.11. Normalized distance for 25 bands.

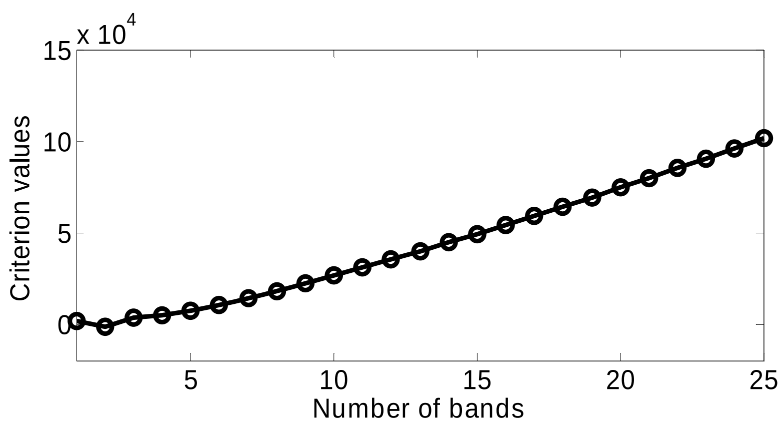

Figure 6.12. Criterion values by ICOMP for different number of selected bands.

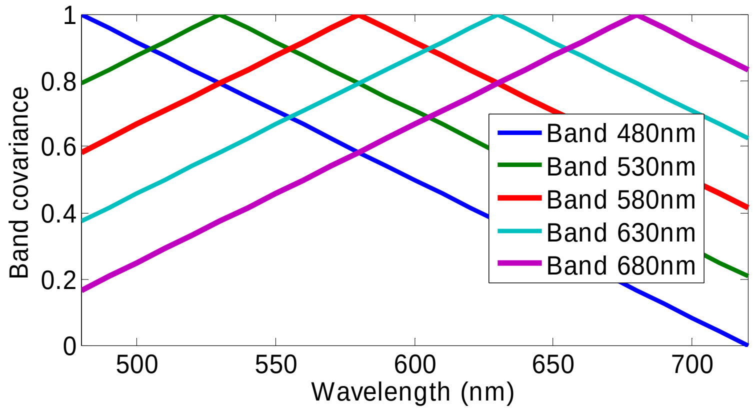

Figure 6.13. Covariance matrix of bands (480, 530, 580, 630, 680) (480nm in blue line, band 530nm in green, 580nm in red, 630nm in cyan and 680nm in purple).

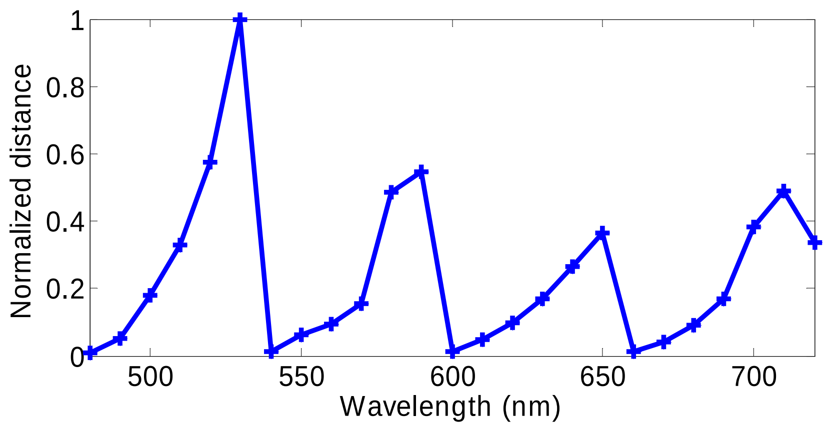

Figure 6.14. Normalized distance for 25 bands of four peaks.

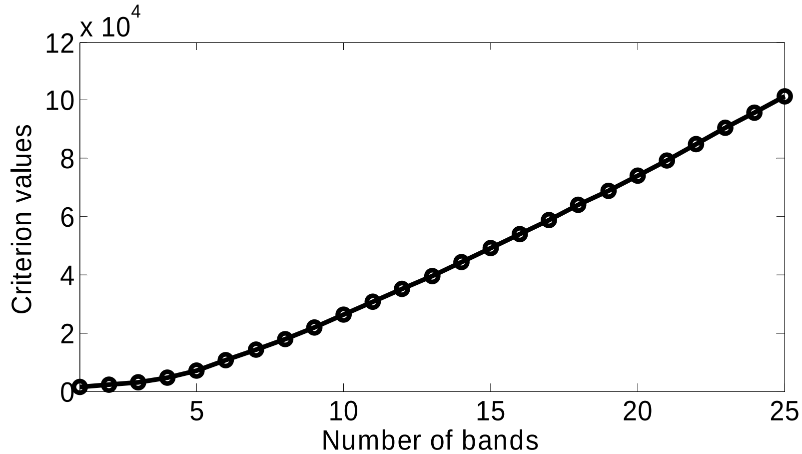

Figure 6.15. Criterion values by ICOMP for different number of selected bands.

6.3.3 Fluorescent gallery, halogen probe

In this experiment, the optimal spectral bands of multispectral face images under halogen light is selected via proposed algorithm while gallery images are under another indoor lighting, fluorescent light. There are 25 sets of probe images are involved in the selection. They are sub-spectral narrow-band images between wavelength 480nm and 720nm with increment of 10nm.

Matusita distance measure via cosine kernel and ICOMP is shown in Figure 6.16. The results using Identix are indicated by triangle and Cognitec by stars. Note that even though there is performance difference between the two tested engines, the ranking tendency is similar by these two engines, which verifies the generality of our proposed algorithms. Therefore, without repetition, only the rank-one and CMC results by FaceIt® are given in the following discussions.

The ranked bands in a descending order by DBS are (610, 630, 640, 620, 600, 660, 680, 650, 690, 670, 700, 720, 710, 590, 570, 580, 540, 560, 550, 530, 510, 520, 500, 490, 480). The criterion values via ICOMP calculation of each possible number of selected bands are given in Figure 6.17. The corresponding 25 criterion values are (0.0641, 0.1324, 0.3201, 0.5462, 0.7617, 1.0309, 1.3340, 1.6482, 1.9712, 2.3149, 2.6462, 2.9902, 3.3548, 3.6980, 4.0514, 4.4137, 4.7556, 5.1311, 5.5102, 5.8803, 6.2585, 6.6543, 7.0320, 7.4232, 7.7887) x 10^3 for each number of bands, respectively. This algorithm picked one band only, which is indicated by the lowest criterion value. This means the number of selected bands should be one and this band is 610nm.

To prove that the selection results is accurate, face recognition performances including the rank-one recognition rate and CMCM values of band (610), (610, 640) and (610, 630, 640) are tested and given in Figure 6.18 and Figure 6.19 with also those of the conventional broad-band images. The reason for only one band selected lies in the fact that the correlation among all the bands are relatively very high as given in Figure 6.20. The images via single selected band outperform the conventional broad-band monochromatic images by relatively 9.7% ((97.14-88.56)/88.56 x100%=9.7%) of rank-one rate and by 4.5% ((98.57-94.28)/94.28 x100%=4.5%) of CMCM values.

One subject record used in this experiment is shown in Figure 6.21. The sub-spectral images under halogen light at wavelength 580nm, 620nm, 660nm, and 700nm are shown in Figures 6.21(a)-(d). Conventional broad-band image, fused image via two bands: 610nm and 640nm and fused image via three bands: 610nm, 630nm, and 640nm are also given in Figures 6.21 (e)-(g).

One of the standard measures of band similarity is normalized correlation [Duda01]. This measure is not sensitive to local mismatches since it is based on a global statistical match. The mathematical description of the normalized correlation measure is the correlation coefficient. After selecting the first least correlated band based on all adjacent bands, the subsequent bands are chosen as the least correlated band based on all adjacent bands [Bajcsy04]. This type of ranking is based on mathematical analysis of [Jia94] where spectrally adjacent blocked bands are represented in a selected subset. By this correlation-based band selection method, for each subject, the selected and ranked bands are different from other subjects. For example, for subject A, the top three bands are (480, 660, 490). For subject B, the top three bands are (480, 690, 570). The only common band for all studied subjects if 480nm. Therefore, the recognition rate of 480nm is given in Table 6.1 for comparison.

Another commonly used existing band selection algorithm is entropy-based band selection [Bajcsy04]. The bands with higher entropy have more information than those with lower entropy. Therefore, we obtained the entropy values for every available band image for each subject and they are given in Figure 6.22. The top candidates from entropy-based algorithm are (720, 710, 700). The recognition performance by entropy-based band selection is also obtained for comparison in Table 6.1. Our proposed band selection algorithms outperform not only the conventional images, but also correlation-based band selection and entropy-based band selection algorithms.

6.3.4 Daylight gallery, halogen probe

In this experiment, 25 probe sets from narrow-band spectral images are acquired under halogen light while the gallery images are acquired under daylight.

Normalized distances of 25 probe sets shown in Figure 6.23 are ranked in a descending order as (610, 620, 600, 650, 630, 680, 660, 670, 690, 650, 590, 700, 570, 580, 720, 530, 560, 710, 510, 540, 550, 520, 490, 500, 480). Criterion values with the increasing number of bands are given in Figure 6.24. CDBS selects band (610) as the optimal subset.

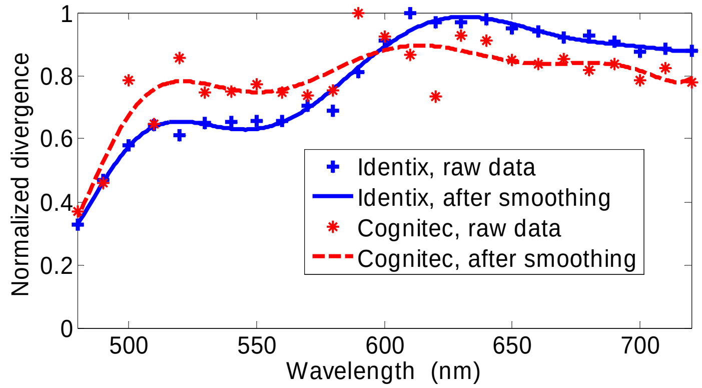

Figure 6.16. Normalized distance measure result of 25 probe sets, including sub-spectral narrow-band images from 480nm to 720 with the increment of 10nm under halogen light while the gallery images are acquired under fluorescent light. The ranking of bands in a descending order as (610, 640, 660, 680, 720, 570, 540, 510, 630, 620, 600, 650, 690, 670, 700, 710, 590, 580, 560, 550, 530, 520, 500, 490, 480).

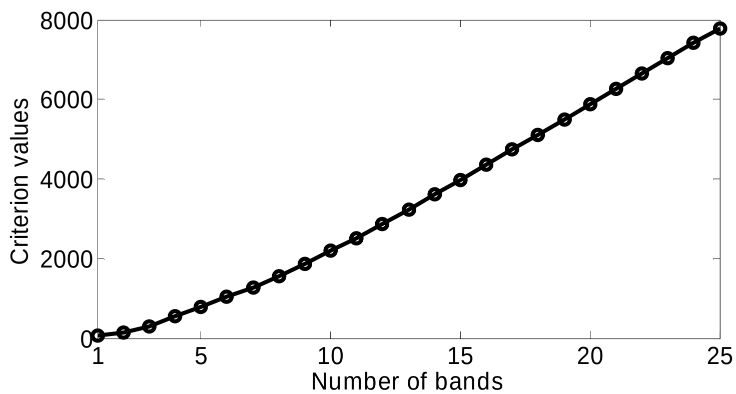

Figure 6.17. Criterion values calculated by ICOMP for different number of bands ranging from 1 to 25. The top one band (610nm) is selected with the minimal criterion value.

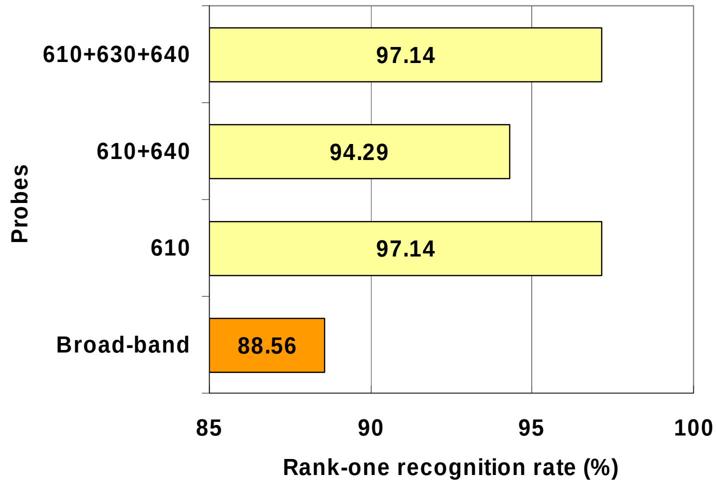

Figure 6.18. Rank-one recognition rate of different probe sets, including conventional broad-band images, single sub-spectral images at 610nm, fused images from selected two bands (610, 640) and selected three bands (610, 630, 640).

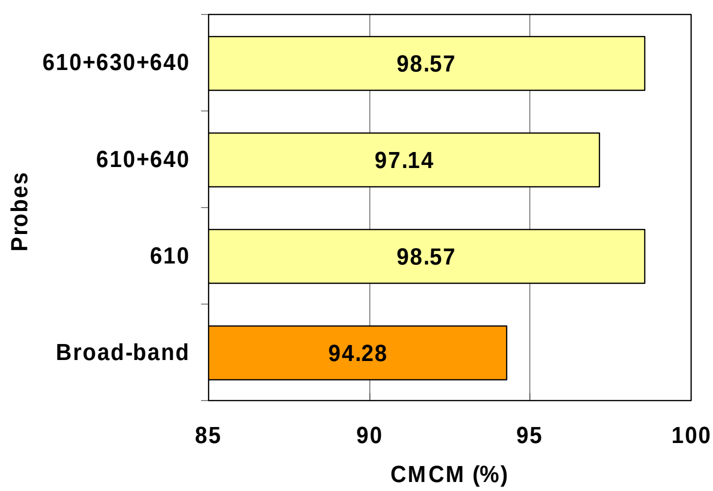

Figure 6.19. CMCM values of different probe sets, including conventional broad-band images, single sub-spectral images at 610nm, fused images from selected two bands (610, 640) and selected three bands (610, 630, 640).

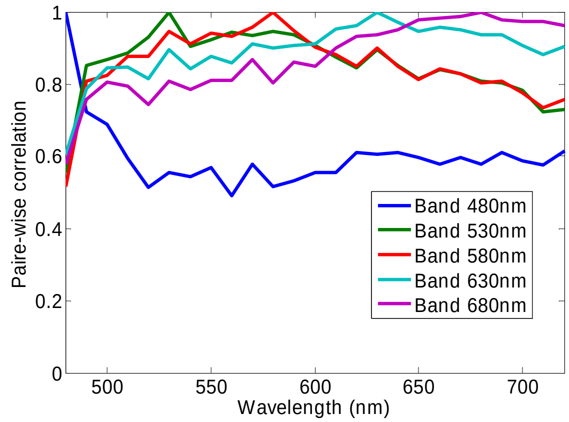

Figure 6.20. Illustration of covariance matrix for band 480nm, 530nm, 580nm, 630nm and 680nm.

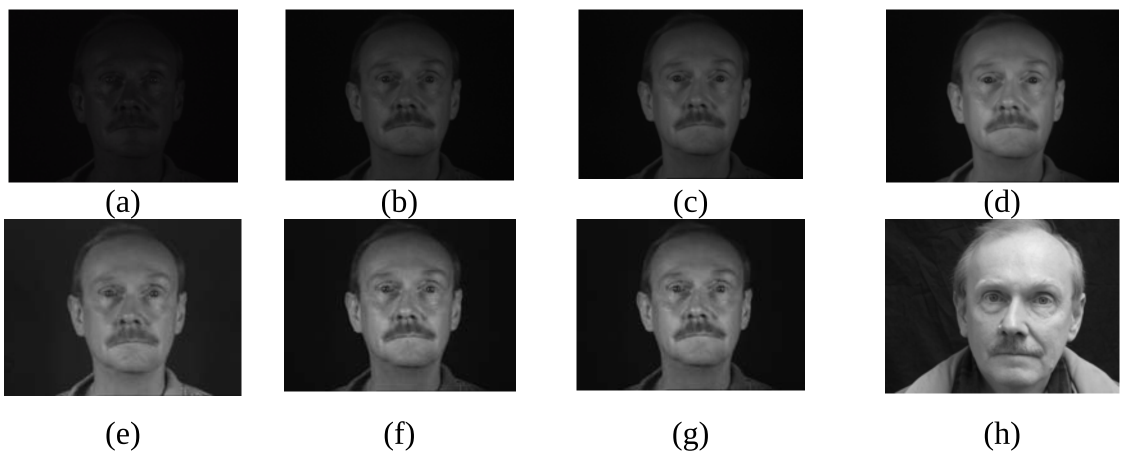

Figure 6.21. (a-d) Sub-spectral images under halogen light at wavelength 580nm, 620nm, 660nm, and 700nm. (e) Conventional broad-band image under halogen light as the comparison. (f) Fused image via two bands: 610nm and 640nm. (g) Fused image via three bands: 610nm, 630nm, and 640nm. (h) Gallery image: conventional broad-band image under fluorescent light.

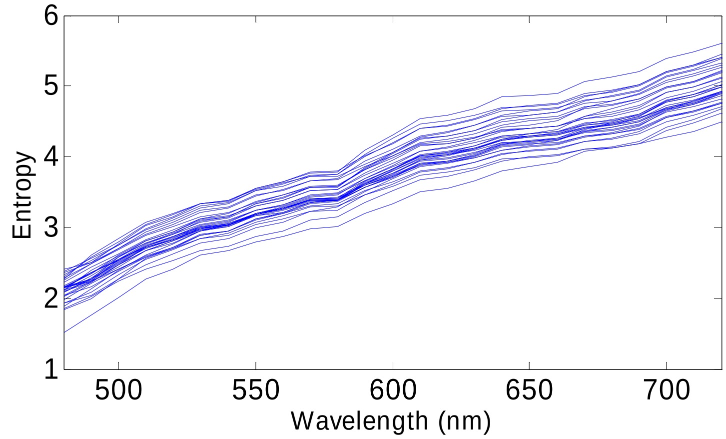

Figure 6.22. Entropy values of 25 band images of 35 subjects under halogen light. Each subject is presented by a blue line.

Table 6.1. Rank-one recognition rates from proposed band selection algorithm, entropy-based band selection algorithm.

Probes	Conventional broad-band image	Correlation-based band selection	Proposed band selection	Entropy-based band selection		
Bands		480	610	720	720 710	720 710 700
Rank-one (%)	88.56	51.43	**97.14**	82.86	85.71	82.86

Figure 6.25 demonstrates the rank-one recognition rate of various probes including single sub-spectral band (610), conventional broad-band, and fused images from two bands (610, 620) and three bands (610, 620, 600). Figure 6.26 gives the CMCM performance of the corresponding probe sets. As expected, the correlations among all the bands are relatively high as given in Figure 6.27. The images via single selected band outperform the conventional broad-band monochromatic images by an increase of 15% in rake-one rate and 5.5% in CMCM values. Normally we would not expect the fusion of two or three bands outperform the single band while ICOMP values indicate one band is sufficient. However, in this set of experiments, an unusual data situation is employed: the gallery images are the outdoor side illuminated faces so that varying shadows on different sample which cause the insecurity in similarity score values. Hence it affects our band selection results. Therefore, the fusion of the top two bands achieves an even better performance than conventional broad-band images by an increase of 20% in rake-one rate and 6.7% in CMCM values. Another reason of the better performance in the fusion of two or three bands is that fusion of two neighbor bands may not increase the useful information but decreases the noise compared to one band so that it provides a better result. One data record used in this experiment is shown in Figure 6.28.

Note that the images from adjacent bands are correlated. In multispectral image fusion, more bands do not guarantee a better performance or more useful information. On the contrary, it may even deteriorate the results. For instance, with the given lighting condition in experiment 6.3.4, the fusion of bands 610nm and 620nm provides a better recognition rate than the fusion of three bands 610nm, 620nm, and 630nm. Time lapse between gallery and probe acquisitions is more than six months in this experiment, which is very close to practical face recognition situation. We found that with different gallery illumination in experiment 6.3.3 and experiment 6.3.4, the same optimal spectral range is selected while the probe images are acquired under the same illuminant, halogen light.

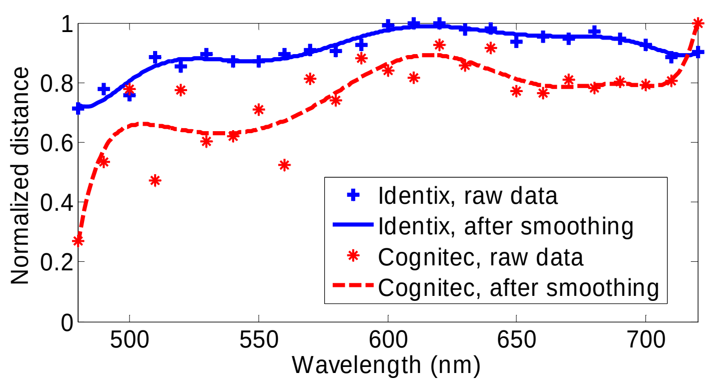

Figure 6.23. Normalized distance of 25 probes including sub-spectral narrow-band images from 480nm to 720nm with the increment of 10nm under halogen light while the gallery images are acquired under daylight.

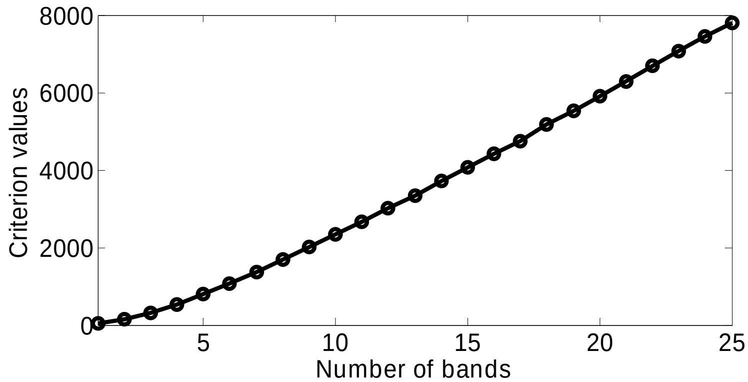

Figure 6.24. Criterion values calculated by ICOMP for different number of bands ranging from 1 to 25 and the top one band (610) with the minimal value.

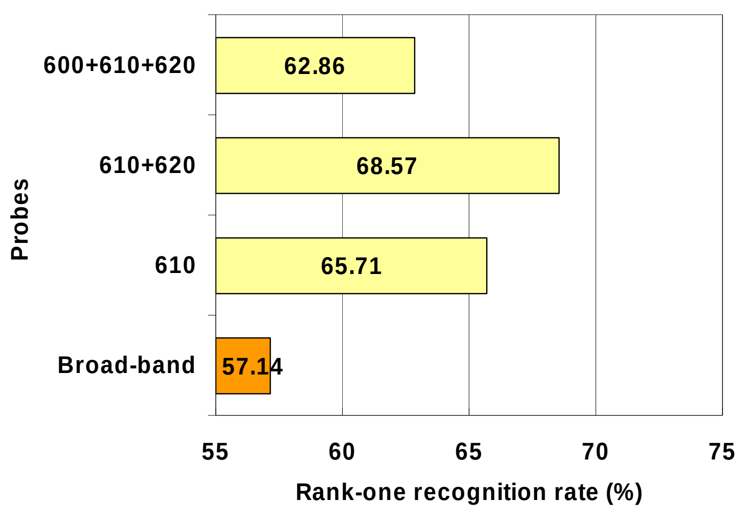

Figure 6.25. Rank-one recognition rates of different probe sets, including conventional broad-band images, single sub-spectral images (610), and fused images from (610, 620) and (610, 620, 600).

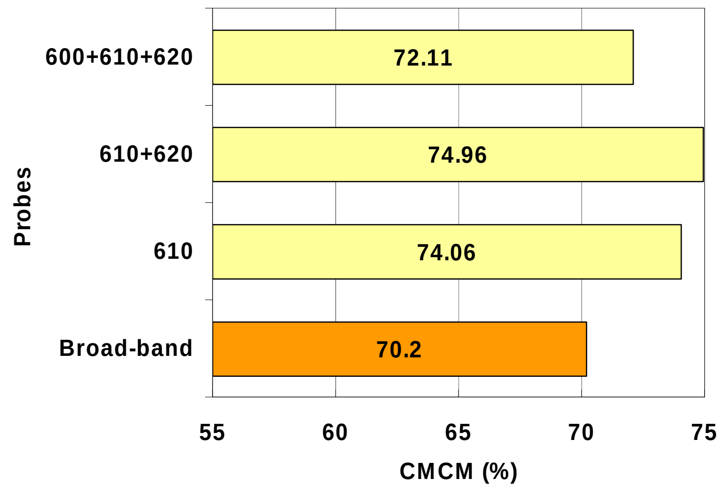

Figure 6.26. CMCM values of different probe sets, including conventional broad-band images, single sub-spectral images (610), and fused images from (610, 620) and (610, 620, 600).

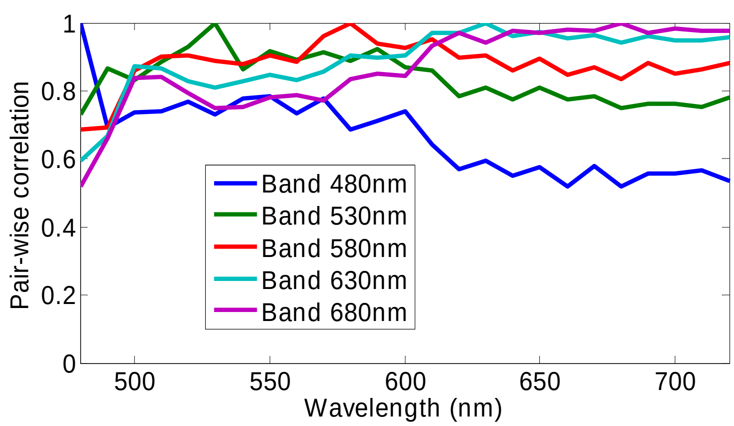

Figure 6.27. Illustration of the pair-wise correlation for band 480nm, 530nm, 580nm, 630nm and 680nm.

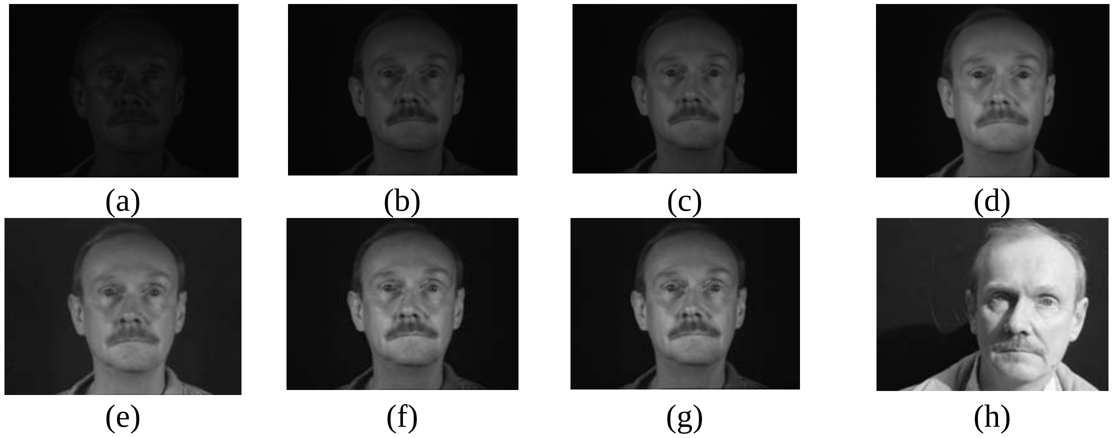

Figure 6.28. (a-d) Sub-spectral images under halogen light at wavelength 580nm, 620nm, 660nm, and 700nm. (e) Conventional broad-band image under halogen light as the comparison. (f) Fused image via two bands: 610nm and 620nm. (g) Fused image via three bands, 610nm, 620nm, and 630nm. (h) Gallery image: conventional broad-band image under daylight.

We also compared the performance between our proposed algorithms to those of entropy-based band selection and correlation-based band selection. The entropy of MSIs under halogen light has been illustrated in Figure 6.22 and the top three bands selected by entropy-based band selection are (720, 710, 700). The common band selected by correlation-based band selection is 480nm.

6.3.5 Fluorescent gallery, daylight probe

In this experiment, the most challenging lighting condition, daylight, is investigated for probe sets. To simulate practical face recognition, stable indoor fluorescent light is used for gallery images while all the probes are acquired under varying daylight. The spectral range is selected among 13 sets of narrow-band spectral images from wavelength 480nm to 720nm with the increment of 20nm.

13 narrow-band spectral image probe sets are ranked by distance-based band selection in a descending order as (720, 680, 640, 700, 660, 640, 520, 600, 560, 500, 580, 480, 540). The distances are given in Figure 6.29. ICOMP values of ((0.0723, 0.1387, 0.2815, 0.4981, 0.7046, 0.9467, 1.2102, 1.4804, 1.7454, 2.0437, 2.3304, 2.6559, 2.9870) x 10^3) with the increasing number of bands are given in Figure 6.30. In this experiment, our selection result is again one band (720). Figure 6.31 demonstrates the rank-one recognition rate of various probes including single sub-spectral band (720), conventional broad-band, and fused images from two (720, 680) and the top three bands (640, 680, 720). Figure 6.32 gives the CMCM performance of the corresponding probe sets. As expected, the correlations among all the bands are relatively very high as given in Figure 6.33. We found that probes from a single band 720nm and the fused images of two and three bands outperform the conventional broad band images by 3% in rank-one rate and 3.4% in CMCM values. In parallel, Figure 6.34 depicts one data record used in this experiment.

Table 6.2. Rank-one recognition rates from proposed band selection algorithm and the entropy-based band selection algorithm.

Probes	Conventional broad-band image	Correlation-based band selection	Proposed band selection	Entropy-based band selection		
Bands		480	610	720	720 710	720 710 700
Rank-one (%)	57.14	45.71	**65.71**	45.71	51.42	45.71

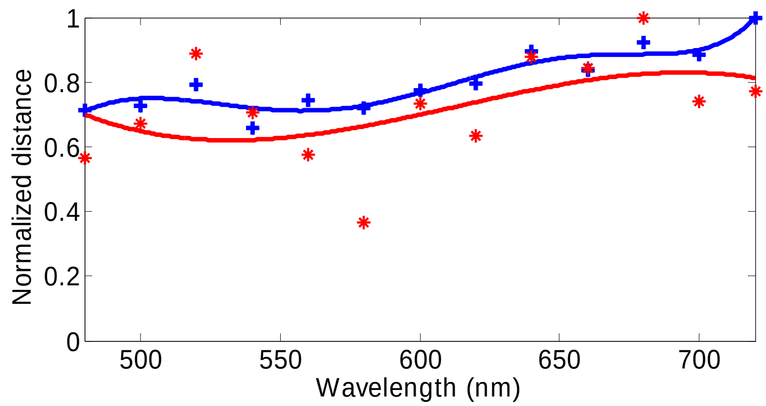

Figure 6.29. Normalized divergence of 13 probes including sub-spectral narrow-band images from 480nm to 720nm with the increment of 20nm under varying daylight while the gallery images are acquired under fluorescent light.

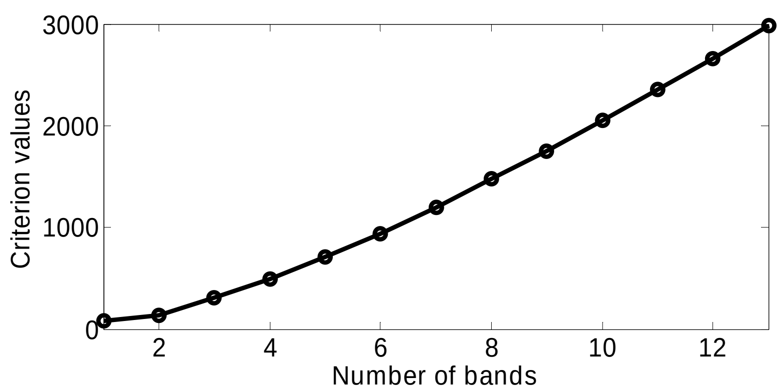

Figure 6.30. Criterion values calculated by ICOMP for different number of bands ranging from 1 to 13 and the top one band (720nm) with the minimal value.

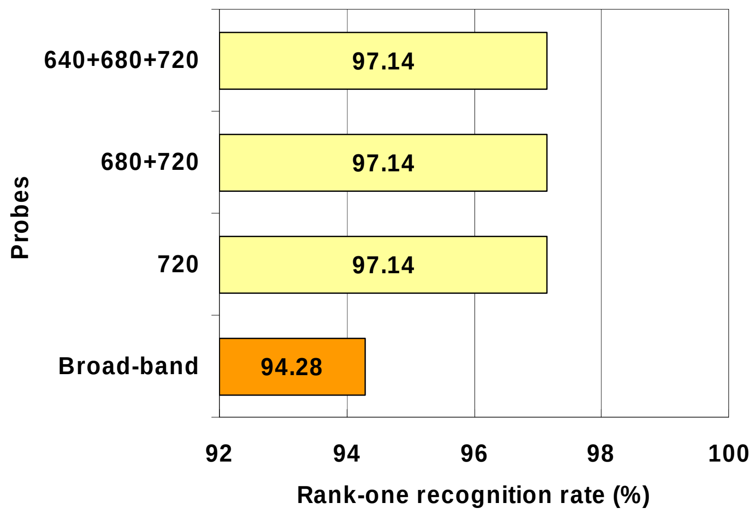

Figure 6.31. Rank-one recognition rates of various probes, including broad-band monochromatic image, narrow-band images of 720nm and fused images from bands (680 720) and (640, 680, 720).

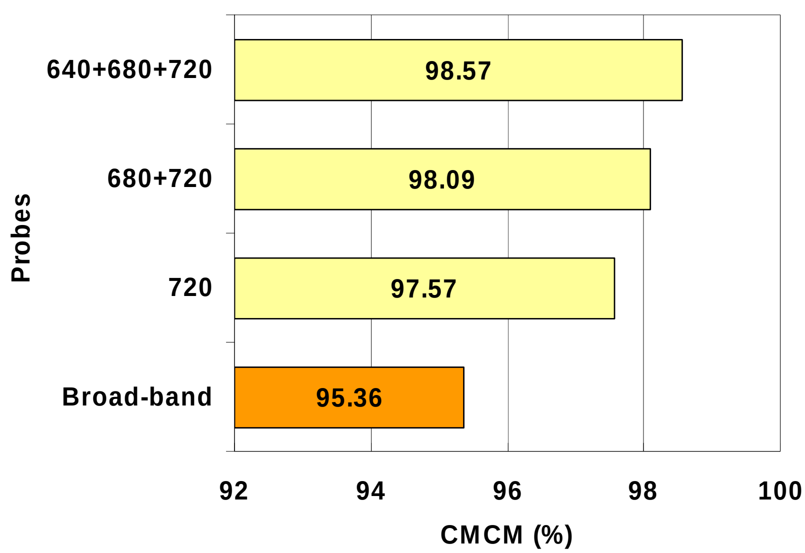

Figure 6.32. CMCM values of various probes, including broad-band monochromatic image, narrow-band images of 720nm and fused images from bands (680 720) and (640, 680, 720).

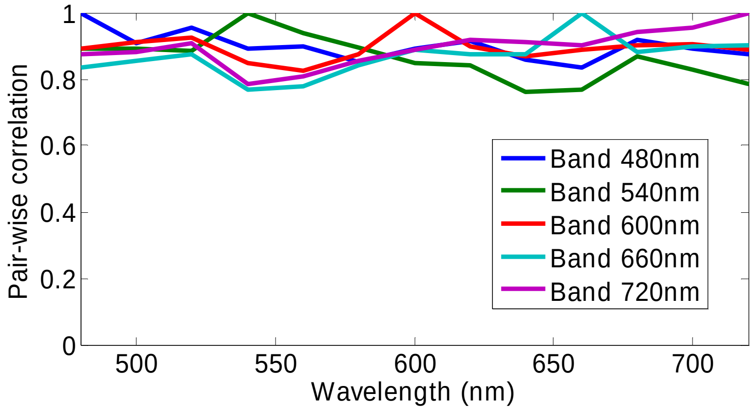

Figure 6.33. Illustration of the pair-wise correlation for band 480nm, 540nm, 600nm, 660nm and 720nm.

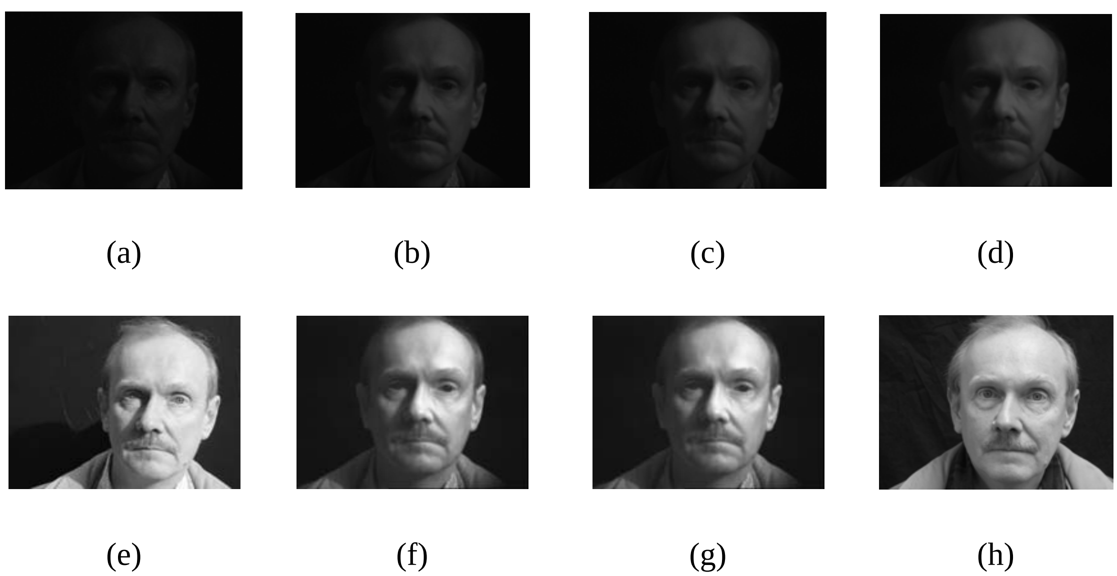

Figure 6.34. (a-d) Sub-spectral images under daylight at wavelength 580nm, 620nm, 660nm, and 700nm. (e) Conventional broad-band image under daylight as the comparison. (f) Fused image via two bands (680, 720). (g) Fused image via three bands (640, 680, 720). (h) Gallery image: conventional broad-band image under fluorescent light.

We also compared the performance between our proposed algorithms to those of entropy-based band selection and correlation-based band selection. The entropy of MSIs under daylight is illustrated in Figure 6.35 and we can see that the top two bands selected by entropy-based band selection is (700, 720). The common band selected by correlation-based band selection is 480nm.

6.3.6 Halogen gallery, daylight probe

In this experiment, halogen light is used for gallery images while all the probes are acquired under varying daylight. There are 13 sets of narrow-band spectral images from wavelength 480nm to 720nm with the increment of 20nm.

Normalized distances of 13 narrow-band spectral image probe sets ranked in a descending order are (720, 660, 700 680, 620, 640, 600, 560, 580, 540, 520, 500, 480) which is shown in Figure 6.36. ICOMP values for different number of bands are given in Figure 6.37. Our algorithm selected band (720). In Figure 6.38 and Figure 6.39, the rank-one recognition rate and CMCM values of various probes including single sub-spectral band (720), conventional broad-band, and fused images from two (720, 660) and three bands (660, 700, 720) are illustrated. We found that probes from a single band 720nm outperform the conventional broad band images by 11.8% in rank-one rate and 13.1% in CMCM values. The covariance matrix among bands is given in Figure 6.40. Figure 6.41 depicts one data record used in this experiment.

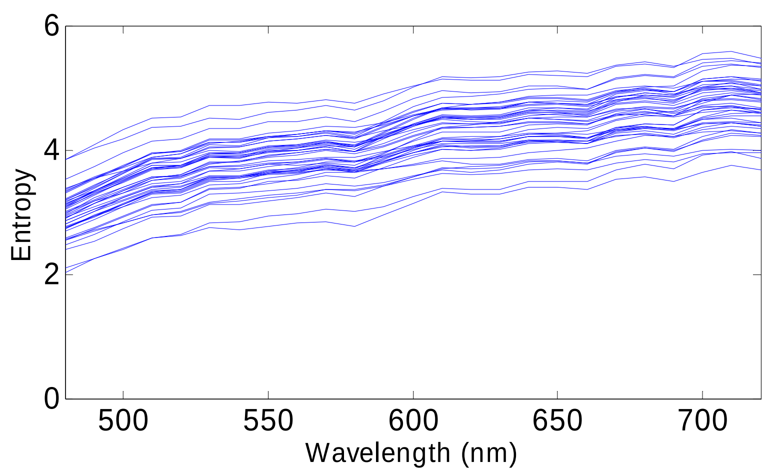

Figure 6.35. Entropy values of 13 band images of 35 subjects under halogen light. Each subject is presented by a blue line.

Table 6.3. Rank-one recognition rates from proposed band selection algorithm and the entropy-based band selection algorithm.

Probes	Conventional broad-band image	Correlation-based band selection	Proposed band selection	Entropy-based band selection	
Bands		480	720	700	700 720
Rank-one (%)	94.28	71.43	**97.14**	91.43	91.43

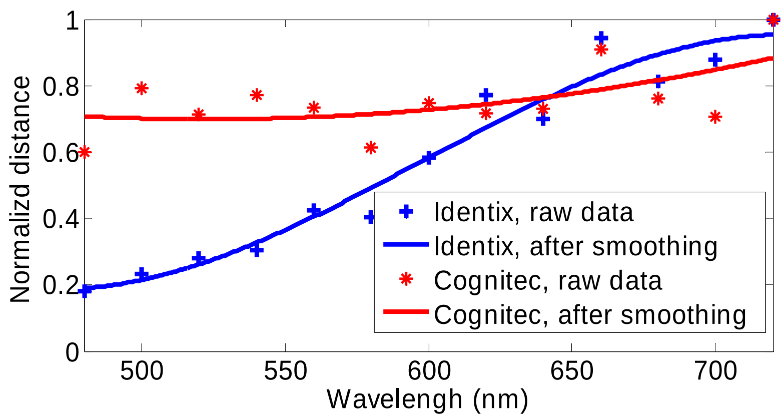

Figure 6.36. Normalized divergence of 13 probes including sub-spectral narrow-band images from 480nm to 720nm with the increment of 20nm under varying daylight while the gallery images are acquired under fluorescent light.

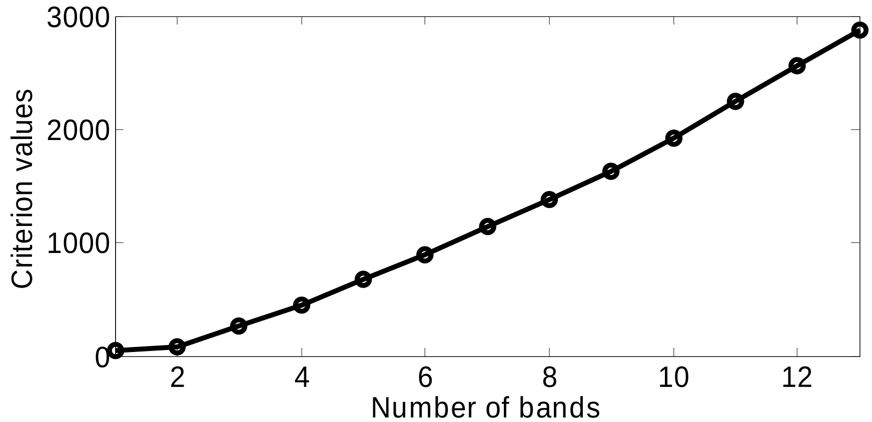

Figure 6.37. Criterion values calculated by ICOMP for different number of bands ranging from 1 to 13 and the top one band (720nm) with the minimal value.

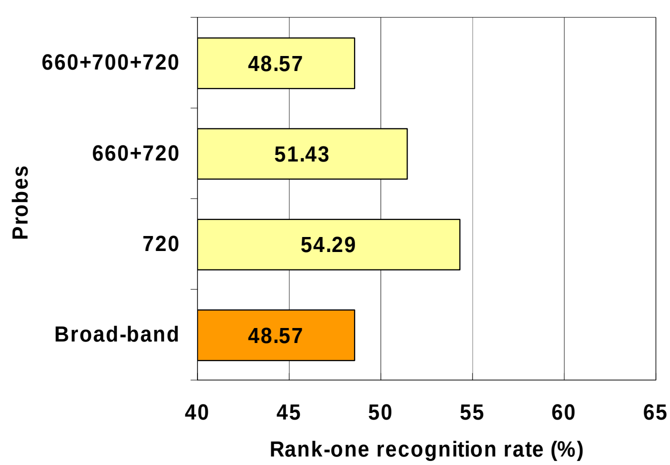

Figure 6.38. Rank-one recognition rates of various probes, including monochromatic conventional broad-band image, narrow-band images of 720nm and fused images from band (660, 720) and (660 700 720).

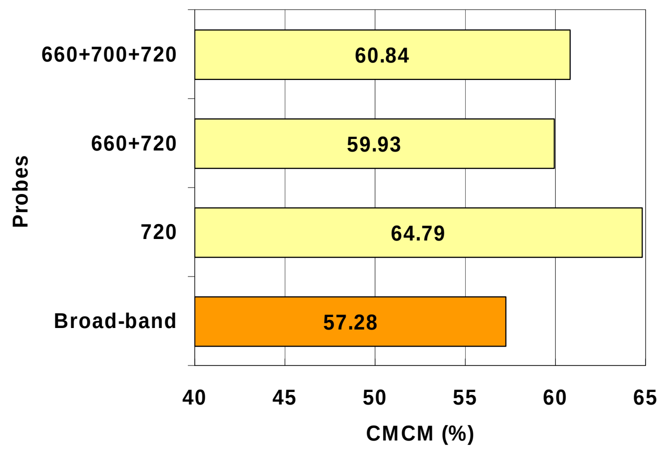

Figure 6.39. CMCM values of various probes, including broad-band monochromatic image, narrow-band images of 720nm and fused images from bands (680 720) and (640, 680, 720).

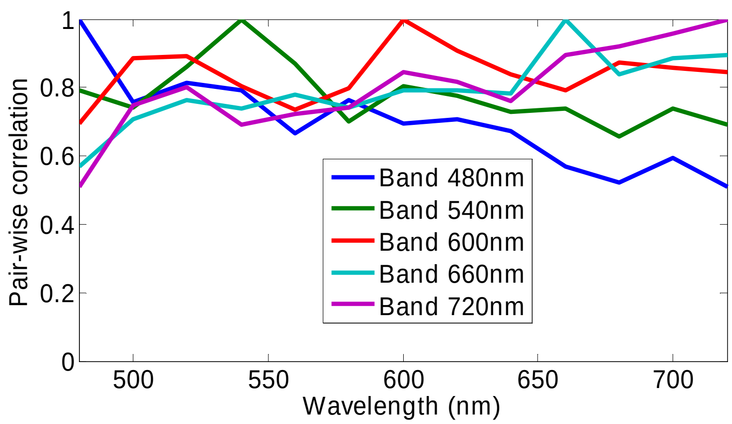

Figure 6.40. Illustration of the pair-wise correlation for band 480nm, 540nm, 600nm, 660nm and 720nm.

We also compared the performance between our proposed algorithms to those of entropy-based band selection and correlation-based band selection. The entropy of MSIs under daylight is illustrated in Figure 6.35 and we can see that the top two bands selected by entropy-based band selection is (700, 720). The common band selected by correlation-based band selection is 480nm. Our proposed band selection algorithm provides the best performance compared to conventional images, fused images by correlation-based or entropy-based band selection algorithms.

6.4 Summary

To verify our proposed distance-based band selection and complexity-guided distance-based band selection algorithms, we categorized our experimental results into two groups. The first group of experimental results came from simulated data and the second group obtained the band selection results from real data.

In the first group of experiments, random data sets which can represent the similarity scores of genuine and imposter sets of each band are created with pre-defined correlations among them. Our algorithm selected the bands with relatively largest distances and the

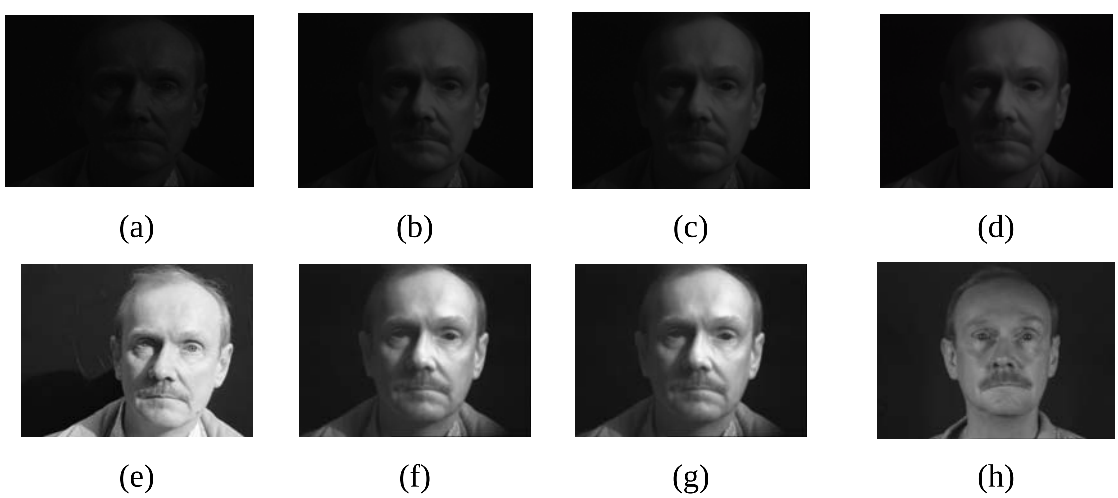

Figure 6.41. (a-d) Sub-spectral images under daylight at wavelength 580nm, 620nm, 660nm, and 720nm. (e) Conventional broad-band image under daylight as the comparison. (f) Fused image via two bands (660, 720) (g) Fused image via three bands (660, 700, 720). (h) Gallery image: conventional broad-band image under halogen light.

most independent bands with relatively low correlation simultaneously. As we expected, while the correlations among bands are very high, even though there are several local peaks from the distance measures, one band or less bands than the total number of peaks with the highest distance value is selected. This verified the effectiveness of our band selection algorithm.

Because real data has very high correlation among different bands, single band rather than multi-narrow bands is selected for face recognition system. Our selection results are verified by four independent experiments with different illumination for gallery and probes. We summarize experimental results from real data in Table 6.5. It is observed that while the probes are under halogen light, the optimal spectral band is the same (band 610nm) with various illumination for gallery images even with different gallery lighting. For outdoor daylight probe images, band 720nm is the optimal band solution with either fluorescent or halogen for gallery images.

The recognition performance under varying outdoor daylight has been the one of the most difficult task for face recognition research society. From the table, a noticeable recognition improvement of 3 to 13% has been achieved considering the severe changes caused by illumination variation.

Our experimental results demonstrate that face recognition rate from the selected bands can be substantially improved over that of the conventional broad-band images for both indoor and outdoor environments. The selected bands are verified to outperform the conventional broad-band images by up to 15% based on a variety of experiments using two well-recognized face recognition engines. We also compared our proposed selection algorithm with entropy-based band selection and correlation-based band selection. Both of the compared algorithms did not outperform the conventional images or our proposed algorithms. There are other information-based band selection algorithms in the literature. However, these algorithms need a spectral signature or ground truth to do the band selection which in our case, the ground truth is not available.

In addition, our algorithm is able to consistently locate the optimal bands with no prior knowledge of the imaging system's configuration and the characteristics of the illumination. The observation that single band or the fused images based on band ranking provides better recognition rate than broad-band images can be explained as follows. The beneficial facial information including spectral information carried in a broad-band image has been compromised by the imaging (integration) process. On the other hand, the spectral information which contributes most to face recognition has been utilized and emphasized by our method so that our method can improve the recognition performance. In other words, the most beneficial information for face recognition is specifically picked out towards improved face recognition performance.

Different pre-processing and feature selection methods may produce different results. In our experiments to illustrate the performance difference, similarity scores are obtained via two well-known recognition engines, Identix's FaceIt® and Cognitec's FaceVACS®. These two recognition engines explore different pre-processing, feature selection, and recognition methods. However, from our experimental results, we could see that despite of the existence of performance difference, the optimal bands selected via these two engines are similar. This verifies the effectiveness of our algorithm. Our algorithm is general enough to incorporate systems based on different pre-processing and feature selection methods.

Variation in illumination dramatically degrades face recognition performance. We proposed using narrow-band sub-spectral images instead of conventional broad-band images to improve recognition performance. A simplified multispectral face imaging system can be achieved based on this work and it can be practically used for a customized sensor associated with given illuminations to benefit the security system based on face recognition.

Table 6.4. Rank-one recognition rates comparison.

Probes	Conventional Broad-band image	Correlation-based band selection	Proposed band selection	Entropy-based band selection	
Bands		480	720	700	700 720
Rank-one (%)	48.57	31.43	**54.29**	51.43	51.43

Table 6.5. Summary of experiments from real data on selected bands and corresponding performance improvement.

Experiment	Illumination		Optimal bands (nm)	Improvement	
	Gallery	Probe		Rank-one (%)	CMCM (%)
1	Fluorescent	Halogen	610	9.7	4.5
2	Daylight	Halogen	610	15	5.5
3	Fluorescent	Daylight	720	3	3.4
4	Halogen	Daylight	720	11.8	13.1

7 Conclusions

In this dissertation, three key issues are addressed in an automatic multispectral face recognition system: database imaging system, image fusion and band selection for information redundancy. The face imaging system in visible spectrum was designed for both multispectral narrow-band images and conventional broad-band images acquisition and for further study in new algorithms towards performance comparison via the same most advanced face recognition engine.

Proposed image fusion algorithms were proved to outperform the conventional images via several experiments. Distance-based band selection algorithm was implemented with different parameters in kernel estimation and distance measures. The results demonstrated a stable band ranking results for band selection and robustness to the changes of parameters. Furthermore, an improved version of distance-based band selection which can automatically decide the number of bands, complexity-guided distance-based band selection, was fully developed. From both simulated data and real data in 6 sets of experiments, the effectiveness and accuracy of the proposed algorithms have been illustrated by comparing to conventional images and state of the art.

In previous chapters, a practical and efficient multispectral face imaging system was developed, the theoretical framework was derived, and the effectiveness of the proposed methods are demonstrated via extensive experiments and comparisons with existing imaging system and algorithms. In this chapter, this dissertation is concluded with a brief summary of the contributions in section 7.1 and the discussion of the directions for future research in section 7.2.

7.1 Summary of contributions

A multispectral face recognition system and the corresponding new image processing approaches were proposed for improving the automatic face recognition system performance for the condition of severe illumination changes. A practical imaging system was built and tested. Corresponding fusion algorithms for face recognition and the information redundancy process of band selection algorithms were verified via several set of experiments. The key contributions of this research are the followings.

Image fusion: Four image fusion algorithms were proposed and compared with conventional images via several real data sets under varying illuminations. Physics-based weighted fusion and illumination adjustment fusion which utilized the physics parameters of the narrow-band imaging system provide better recognition rate than conventional images and the PCA fusion. Wavelet fusion and rank-based decision level fusion outperforms the conventional images by up to78% while the illumination is the most severe outdoor daylight.

Distance-based band selection: The novelty of this method lies in the introduction of a quantitative performance evaluation metric which calculates the distribution separation and the selection of the optimal bands by ranking these separation values. A noticeable property of this method is the robustness to changes of each of the free parameters in the algorithm, such as different kernels, different smoothing parameters and various distance measures. From experiments, the top one, two or three ranked bands are proved to outperform the conventional images and state of the art.

Complexity-guided distance-based band selection: This algorithm is an automatic band selection algorithm which balances the band selection results between the performance metric and the dependency among bands to achieve high performance and least redundancy. The balance is carried out by the employment of information complexity as selection criterion on the quantitative performance evaluation metric. The optimal number of bands can be automatically determined without any prior request. The selected bands have been proved with effectiveness from experiments of both simulated data and real data with different illumination conditions. The selected bands outperform the conventional images by up to 15%. A simple and practical multispectral face imaging system can be customized and it will benefit the security system based on biometric recognition.

For each of these contributions, we have presented both quantitative and quality comparisons to demonstrate their strength and analyze their limitations. The multispectral imaging system and corresponding database was developed and established in [Chang06a]. Image fusion algorithms are presented in [Chang06b, Chang06c]. A journal version of both imaging system and image fusion is accepted in [Chang08c]. Distance-based band selection was published in [Chang08a, Chang08b]. The complete work on the distance-based band selection is under second round review [Chang08d]. The work regarding complexity-guided distance-based band selection is under preparing for submission to a journal.

7.2 Directions for future research

The ideas and concepts in this dissertation offer interesting avenues for future research in improving face recognition performance for security. Since this is the first work on narrow-band face recognition in visible spectrum, there are many promising directions and the following areas are particularly important for the following reasons.

7.2.1 Broader spectrum range

In my research, the visible spectrum is our focus which is roughly between 400 and 750nm, and is a relatively narrow range in the whole spectrum. From our experiments and results, we found that the band information in such narrow range has very high correlation and hence, one band is enough for the purpose of better face recognition performance. However, it is may not be the case for a broader range spectrum. In standard hyperspectral image acquisition, the range can spread from 300nm to 2200nm or even more so that there are multiple numbers of bands can be selected for different recognition or detection purposes. In face recognition, there has not been any research done in such broad range with very narrow-band spectral images. Many researchers have considered the broad-band images in blue green and red with one or two band in near infrared or in near infrared [Pan03]. However, narrow-band spectral images in both visible and near infrared or even ultraviolet can be considered together. In our experiments from simulated data, it can be observed that the optimal number of bands is determined by both dependency between bands and the distance values which indicates the recognition performance directly. In other words, in a broader range of spectrum within and beyond the visible spectrum, the number of selected bands with relatively large distance values can be multiple and various according to the correlation among them.

7.2.2 Image fusion

In this work, image fusion for spectral images has been discussed in depth, especially for all the bands available. We utilized the physics properties of the imaging system to achieve up to 78% recognition performance improvement in rank-one values. However, these fusion algorithms can not be used after band selection because the physics properties in the spectral domain contributed to improvement can only work while the number of bands contributing to fusion is plenty. Therefore, after our band selection, the scheme of fusion needs to be changed.

Different fusion algorithms affect the fused image results and further effects the performance. In our work, Harr wavelet fusion is conducted for the performance comparison after band selection, which is a very simple wavelet fusion algorithm without studying the coefficient values. Additional image fusion algorithms, with different wavelet or schemes definitely are the very next valuable research on the selected band images to achieve a better performance.

7.2.3 Image enhancement

One of the main barriers to our performance improvement is the image quality due to the hardware physics constraint, such as camera and the filter. For example, the video camera has a fixed focus length and can not adapt different wavelength tuning in our case. Therefore, the acquired spectral images have different level of blurring caused by the changes of wavelength passed through the narrow filters.

One solution is the hardware solution, which involves in the more advanced and expensive camera that can automatically change focus according to the wavelength. It also involves the study of calibration of the camera with the tuning the wavelength. This solution is both financial and temporal costly.

A better solution than hardware solution is using image sharpness algorithms to improve either the single band images or the fused images. For example, in the following experiment, gallery images were acquired under halogen light and probe under daylight. Four probe sets are compared in rank-one values in Table 7.1. Images from an unsharp masking via a laplacian filter conducted on fused images from (660, 720) gained 11.43% improvement than the fused images and wavelet sharpness gained 8.57%. Other enhancement or sharpness methods should also be investigated for the potential performance improvement.

In addition to above mentioned research directions for identification application, false alarm rate can also be investigated as another performance statistic. The false alarm rate provides performance when a probe is not of someone in the gallery. The variance of performance statistics using receiver operating characteristics (ROC) can also be studied for performance evaluation.

Performance evaluation methods of face recognition system include not only face identification but also verification (or authentication). Face identification is the main focus in this dissertation. In other words, the face recognition performance in my work is evaluated statistically among a large group of people and the individual verification performance has not been investigated. The optimal solutions in identification may not give the best results for verification. For example, the selected 610nm is the optimal wavelength for identification performance statistically under halogen light. However, 610nm may not be the optimal wavelength for some certain individual in this group. Therefore, for verification or authentication application, band selection methods should be modified and new approaches for single subject with multispectral narrow-band images can be another future research direction.

Table 7.1. Rank-one recognition rate comparison among broad-band images, fused images, and the enhanced fused images.

Images	Probe0	Probe 1	Probe 2	Probe 3
	Broad-band Conventional	Fused images of (660,720)	Unsharp masking	Wavelet sharpness
Rank-one (%)	48.57	51.43	62.86	60.00

Bibliography

[Abidi04] B. Abidi, S. Huq, and M. Abidi, “Fusion of visual, thermal, and range as a solution to illumination and pose restrictions in face recognition,” in *IEEE Carnahan Conf. Security Technology*, 2004, pp. 325-330.

[Adhikara56] B. Adhikara and D. Joshi, “Distance discrimination et resume exhaustif,” *Publs. Inst. Statistics*, vol. 5, pp. 57-74, 1956.

[Adini97] Y. Adini, Y. Moses, and S. Ullman, “Face recognition: the problem of compensating for changes in illumination direction,” *IEEE trans. on Pattern Analysis and Machine Intelligence*, vol. 19, no. 7, pp. 721-732. 1997.

[Akaike74] H. Akaike, “A new look at the statistical model identification,” *IEEE Transactions on Automatic Control*, vol. 19, no. 6, pp. 716-723, 1974.

[Alfano95] B. Alfano and J. Mag, “Multiparametric display of spin-echo data from MR studies of brain,” *Resonance Imaging*, vol. 51, pp. 217-225, 1995.

[Angelopoulou01a] E. Angelopoulou, “Understanding the color of human skin,” in *Proc. SPIE*, vol. 4299, 2001, pp. 243-251.

[Angelopoulou01b] E. Angelopoulou, E. M. Rana, and D. Kostas, “Multispectral skin color modeling,” in *IEEE conference on Computer Vision and Pattern Recognition (CVPR) 2001*. IEEE Computer Society Press, 2001. pp. 635-642.

[Bailly-Bailliere03] E. Bailly-Bailliere, S. Bengio, F. Bimbot, M. Hamouz, J. Kittler, J. Mariethoz, J. Matas, K. Messer, V. Popovici, F. Poree, B. Ruiz, and J. P. Thiran, “The BANCA database and evaluation protocol,” in *Proc. of Audio- and Video-Based Biometric Person Authentication*, 2003, pp. 625-638.

[Bajcsy04] P. Bajcsy and P. Groves, “Methodology for hyperspectral band selection,” *Journal Photogram. Eng. Remote Sens*, vol. 70, pp. 793-802, 2004.

[Bartlett01] Bartlett, M.: Face Image Analysis by Unsupervised Learning. Kluwer Academic Publisher (2001).

[Basri2003] R. Basri and D. W. Jacobs, “Lambertian reflectance and linear subspaces,” *IEEE Trans. Pattern Anal. Mach. Intell*, vol. 25, no. 2, pp. 218-233, 2003.

[Bassett97] E. M. Bassett and S. S. Shen, “Information theory-based band selection for multispectral systems,” in *Proc. SPIE*, vol. 3118, 1997, pp. 28-35.

[Bebis06] G. Bebis, A. Gyaourova, S. Singh, and I. Pavlidis, “Face recognition by fusing thermal infrared and visible imagery,” *Image and Vision Computing*, vol. 24, pp. 727-742, 2006.

[Belhumeur97] P. N. Belhumeur, J. P. Hespanha, and D. J. Kriegman, “Eigenfaces vs. fisherfaces recognition using class specific linear projection,” *IEEE Trans. Pattern Anal. Mach. Intell*, vol. 19, no. 7, pp. 711-720, 1997.

[Belhumeur98] P. N. Belhumeur and D. J. Kriegman, “What is the set of images of an object under all possible illumination conditions,” *Int. J. Comput. Vis*, vol. 28, no. 3, pp. 245-260, 1998.

[Bhattacharyya43] A. Bhattacharyya, “On a Measure of Divergence between Two Statistical Populations Defined by Their Probability Distributions,” *Bull. Calcutta Math. Soc.*, vol. 35, pp. 99-109, 1943.

[Bichsel95] M. Bichsel, "Illumination invariant object recognition," in *Proc. of the International Conference on Image Processing*, vol. 3, 1995, pp. 620-623.

[Blackburn01] D. Blackburn, J. M. Bone, and P. J. Phillips, "FRVT 2000 evaluation report," *Technical Report*, Available: http://www.frvt.org, 2001.

[Blome05] D. Bolme, M. Teixeira, R. Beveridge, and B. Draper, "The CSU Face Identification Evaluation System: Its purpose, features, and structure,", *MVA*, vol. 16, no. 2, February 2005, pp. 128-138.

[Bozdogan00] H. Bozdogan, "Akaike's information criterion and recent developments in information complexity," *Journal of Mathematical Psychology*, vol. 44, pp. 62-91, 2000.

[Bozdogan86] H. Bozdogan, "Multi-sample cluster analysis as an alternative to multiple comparison procedures," *Bulletin of Informatics and Cybernetics*, vol. 1-2, pp. 95-129, 1986.

[Bozdogan87] H. Bozdogan, "Model selection and akaike's information criterion," *Psychometrika*, vol. 53, no.3, pp. 345-370, 1987.

[Bruce02] L. Bruce, C. Koger, and J. Li, "Dimensionality reduction of hyperspectral data using discrete wavelet transform feature extraction," *IEEE Transactions on Geoscience and Remote Sensing*, vol. 40, no. 10, pp. 2331-2338, 2002.

[Brusco03] M. J. Brusco, "An enhanced branch-and-bound algorithm for a partitioning problem." Br J Math Stat Psychol, vol. 56, pp. 83-92, 2003.

[Bruzzonne95] L. Bruzzonne, S. S. B, and F. Roli, "An extension to multiclass cases of the jeffreys-matusita distance," *IEEE Transactions on Geoscience and Remote Sensing*, vol. 33, pp. 1318-1321, 1995.

[Bruzzone95] L. Bruzzonne, F. Roli, and S. B. Serpico, "An extension of the Jeffreys–Matusita distance to multiclass cases for feature selection," *IEEE Trans. Geosci. Remote Sens*, vol. 33, no. 6, pp. 1318-1321, 1995.

[Burnham02] K. P. Burnham and D. R. Anderson, *Model selection and multi-model inference*, Springer-Verlag, 2002.

[Carper90] W. J. Carper, T. M. Lillesand, and R. W. Kiefer, "The use of intensity-hue-saturation transformations for merging SPOT panchromatic and multi-spectral image data," *Photogrammetric Engineering & Remote Sensing*, vol. 56, no. 4, pp. 459-467, 1990.

[Chang06a] H. Chang, H. Harishwaran, M. Yi, A. Koschan, B. Abidi, and M. Abidi, "An indoor and outdoor, Multimodal, Multispectral and Multi-illuminant database for face recognition," *IEEE proc. CVPR2006*, *workshop on multi-model biometrics*, 2006, pp. 54-61.

[Chang06b] H. Chang, M. Yi, H. Harishwaran, A. Koschan, B. Abidi, and M. Abidi, "Multispectral face data fusion for indoor, outdoor authentication," *Biometrics Symposium*, 2006.

[Chang06c] H. Chang, A. Koschan, B. Abidi, and M. Abidi, "Physics-based fusion of multispectral data for improved face recognition," *IEEE proc. ICPR2006*, vol. III, 2006, pp. 1083-1086.

[Chang06d] C. Chang and S. Wang, "Constrained band selection for hyperspectral imagery," *Geoscience and Remote Sensing, IEEE Transactions*, vol. 44, pp. 1575-1585, 2006.

[Chang08a] H. Chang, C.-H. Won, S.G. Kong, A. Koschan, and M. Abidi, "Multispectral visible and infrared imaging for face recognition," accepted *Proc. IEEE Conference on Computer Vision and Pattern*

Recognition CVPR 2008, Fifth IEEE International Workshop on Object Tracking and Classification Beyond the Visible Spectrum (OTCBVS), 2008.

[Chang08b] H. Chang, Y. Yao, A. Koschan, B. Abidi, and M. Abidi, “Spectral range selection for improving face recognition under varying illuminations,” accepted *IEEE proc. ICIP* 2008.

[Chang08c] H. Chang, A. Koschan, B. Abidi, and M. Abidi, “Fusing visible continuous spectral images for face recognition under indoor and outdoor illuminations,” *Machine Vision and Applications*, 2008.

[Chang08d] H. Chang, Y. Yao, A. Koschan, B. Abidi, and M. Abidi, “Improving face recognition via narrow-band spectral range selection using Jeffrey divergence,” submitted to *IEEE Trans. on Information Forensics and Security*.

[Chang99] C. I. Chang, Q. Du, T. S. Sun, and M. L. G. Althouse, “A joint band prioritization and band decorrelation approach to band selection for hyperspectral image classification,” *IEEE Trans. Geosci. Remote Sens*, vol. 37, no. 6, pp. 2631-2641, 1999.

[Chatzis99] V. Chatzis, A.G. Bors, and I. Pitas, “Multimodal decision-level fusion for person authentication,” *IEEE Trans. Syst. Man Cybern. Part A*, vol. 29, no. 6, pp. 674-680, 1999.

[Chavez89] P. S. Jr. Chavez and A. Y. Kwarteng, “Extracting spectral contrast in landsat thematic mapper image data using selective principal component analysis,” *Photogrammetric Engineering & Remote Sensing*, vol. 55, no. 3, pp. 339-348, 1989.

[Chavez90] P. S. Jr. Chavez, S. C. sides, and J. A. Anderson, “Comparison of three different methods to merge multiresolution and multispectral data: landsat TM and SPOT panchromatic,” *Photogrammetric Engineering & Remote Sensing*, vol. 57, no. 3, pp. 295-303, 1990.

[Chellappa95] R. Chellappa, C. Wilson, and S. Sirohey, “Human and machine recognition of aces: A survey,” in *Proc. IEEE*, vol. 83, no. 5, 1995, pp. 705-740.

[Chen06] W. Chen, M. J. Er, and S. Wu, “Illumination compensation and normalization for robust face recognition using discrete cosine transform in logarithm domain,” *IEEE Trans. on Systems, Man and Cybernetics, Part B*, vol. 36, pp. 458-466, 2006.

[Chernoff52] H. Chernoff, “A Measure of Asymptotic Efficiency of Tests for a Hypothesis Based on a Sum of Observations,” *Annals of Math. Statistics*, vol. 23, pp. 493-507, 1952.

[Civco89] D. L. Civco, “Topographic normalization of landsat thematic mapper digital imagery,” *Photogrammetric Engineering & Remote Sensing*, vol. 55, no. 9, pp. 1303-1309, 1989.

[Clement85] C. D. Clement, *Gray’s Anatomy of the Human Body*, 13th ed, Williams & Wilkins, 1985.

[Cootes98] T. F. Cootes, G. J. Edwards, and C. J. Taylor, “Active appearance models,” in *Proc. European Conference on Computer Vision*, vol. 2, 1998, pp. 484-498.

[Cover91] T.M. Cover and J.A. Thomas, *Elements of Information Theory*. Wiley, 1991.

[Devijver82] P. Devijver and J. Kittler, Pattern Recognition: A statistical Approach, Prentice Hall, 1982.

[Denzler02] J. Denzler and C. M. Brown, "Information theoretic sensor data selection for active object recognition and state estimation,” *IEEE Transactions on Pattern Analysis and Machine Intelligence*, vol. 24, no. 2, pp. 145-157, 2002.

[Drew92] M. S. Drew and B.V. Funt, “Natural metamers,” *Computer Vision and Image Understanding*, vol. 56, no. 2, pp. 139-151, 1992.

[Du03] H. Du, H. Qi, X. Wang, R. Ramanath, and W. E. Snyder, “Band selection using independent component analysis for hyperspectral image processing,” in *Applied Imagery Pattern Recognition Workshop, 2003. Proc. 32nd*, 2003, pp. 93-98.

[Du07] Q. Du and H. Yang, “Unsupervised band selection for hyperspectral image analysis,” in *Proc. IEEE International Symposium of Geoscience and Remote Sensing Symposium,* pp. 282-285, 2007.

[Duran74] B. S. Duran and P. Odell, *Cluster analysis – a survey*, Springer-Verlag, New York, 1974.

[El-ghazawi01] T. El-ghazawi, S. Kaewpijit, and J. Le Moigne, “Parallel and adaptive reduction of hyperspectral data to intrinsic dimensionality,” in *Proc. 3rd IEEE International Conference on Cluster Computing CLUSTER*, 2001, pp. 102-109.

[Emden71] V. Emden, “An analysis of complexity,” *Mathematical Centre Tracts*, vol. 35, 1971.

[Fairchild01] Mark D. Fairchild, Mitchell R. Rosen, and Garrett M. Johnson, “Spectral and Metameric Color Imaging,” *Technical Report*, Munsell Color Science Laboratory, Aug. 2001.

[Farag02] A. A. Farag, R.M. Mohamed, and H. Mahdi, “Experiments in image classification and data fusion,” in *Proc. of 5th International Conference on Information Fusion*, vol. 1, 2002, pp. 299-308.

[Feris00] R. S. Feris, T. E. de Campos and R.M. Cesar Junior, “Detection and tracking of facial features in video sequences”, *Lecture Notes in Artificial Intelligence*, 2000, 1793(4), pp. 127-135.

[Flynn03] P. J. Flynn, K. W. Bowyer, and P. J. Phillips, “Assessment of time dependency in face recognition: an initial study,” in *Proc. of Audio- and Video-Based Biometric Person Authentication*, 2003, pp. 44-51.

[Gao04] W. Gao, B. Cao, S. Shan, D. Zhou, X. Zhang, and D. Zhao, “The CAS-PEAL large-scale chinese face database and evaluation protocols,” *Technical Report No. JDL_TR_04_FR_001, Joint Research & Development Laboratory, CAS,* pp. 1-13, 2004.

[Gat00] N. Gat, “Imaging spectroscopy using tunable filters: a review,” in *Proc. of SPIE*, vol. 4056, 2000, pp. 50-64.

[Garguet-Duport96] B. Garguet-Duport, J. Girel, J.-M. Chassery, and G. Pautou, “The use of multiresolution analysis and wavelets transform for merging SPOT panchromatic and multispectral image data,” *Photogrammetric Engineering & Remote Sensing*, vol. 62, no. 9, pp. 1057-1066, 1996.

[Garzelli04] A. Garzelli, F. Nencini, L. Alparone, B. Aiazzi, and S. Baronti, **“**Pan-sharpening of multispectral images: a critical review and comparison,” in *Proc. IEEE International Symposium of Geoscience and Remote Sensing*, 2004, vol. 1.

[Georghiades01] A. S. Georghiades, P. N. Belhumeur, and D. W. Jacobs, “From few to many: illumination cone models for face recognition under variable lighting and pose,” *IEEE Trans. Pattern Anal. Mach. Intel,* vol. 23, no. 6, pp. 630-660, 2001.

[Georghiades00] A. S. Georghiades, P.N. Belhumeur, and D. J. Kriegman, “From few to many generative models for recognition under variable pose and illumination,” in *Proc. of the IEEE Conference on Face and Guesture Recognition,* 2000, pp. 277-284.

[Georghiades98] A. S. Georghiades, D. J. Kriegman, and P. N. Belhumeur, “Illumination cones for recognition under variable lighting faces,” in *Proc. of the IEEE Conference on CVPR Santa Barbara*, 1998, pp. 52-58.

[Gokberk07] B. Gokberk, M. Okan ˙Irfanoglu, L. Akarun, and E. Alpaydın, “Learning the best subset of local features for face recognition,” *Pattern Recognition***,** vol. 40, no. 5, pp. 1520-1532, 2007.

[Gonzalez-Audicana04] M. Gonzalez-Audicana, J. L. Saleta, R. G. Catalan, and R. Garcia, “Fusion of multispectral and panchromatic images using improved IHS and PCA merges based on wavelet decomposition,” *IEEE Trans. Geoscience and Remote Sensing*, vol. 42, pp. 1291-1299, 2004.

[Gonzalez-Audicana06] M. Gonzalez-Audicana, X. Otazu, X. Fors, and O. Alvarez-Mozos, “A low computational-cost method to fuse IKONOS images using the spectral response function of its sensors,” *IEEE Trans, on Goesience and remote sensing*, vol. 44, pp. 1683- 1691, 2006.

[Gross01] R. Gross, J. Shi, and J. Cohn, “Quo vadis face recognition,” *Third Workshop on Empirical Evaluation Methods in Computer Vision*, pp. 1-14, 2001.

[Grudin00] M. Grudin, “On internal representations in face recognition,” *Pattern Recognition*, vol. 33, no. 7, pp. 1161-1177, 2000.

[Gruninger01] J. Gruninger, R. L. Sundberg, M. J. Fox, R. Levine, W. F. Mundkowsky, M. S. Salisbury, and A. H. Ratcliff, "Automated optimal channel selection for spectral imaging sensors," in *Algorithms for Multispectral, Hyperspectral and Ultraspectral Imagery VII, S.S.Shen and M.R.Descour, eds, Proc. SPIE,* vol. 4381, 2001, pp. 68-75.

[Guangda03] Hua Gu Guangda Su Cheng Du, "Feature Points Extraction from Faces”, *Proceedings of the Image and Vision Computing*, New Zealand, 2003.

[Guo06] B. Guo, S. R. Gunn, R. I. Damper, and J. D. B. Nelson, “Band selection for hyperspectral image classification using mutual information,” *Geoscience and Remote Sensing Letters, IEEE***,** vol. 3, no. 4, pp. 522-526, 2006.

[Hall83] R. A. Hall and D. P. Greenberg, “A testbed for realistic image synthesis,” *IEEE Computer Graphics and Applications*, vol. 3, no. 8, pp. 10-19, 1983.

[Hall99] R. A. Hall, “Comparing spectral color computations,” *IEEE Computer Graphics and Applications*, vol. 19, no. 4, pp. 36-45, 1999.

[Hallinan94] P.W. Hallinan, “A low-dimensional representation of human faces for arbitrary lighting conditions,” in *Proc. of the IEEE Conference on CVPR Seattle*, 1994, pp. 995-999.

[Hanrahan93] P. Hanrahan, and W. Krueger, “Reflection from layered surfaces due to subsurface scattering”, Proc. of SIGGRAPH 93, 1993, pp. 165-174.

[Hardeberg02] J. Y. Hardeberg, F. Schmitt, and H. Brettel, “Multispectral image capture using a liquid crystal tunable filters,” *Optical Engineering*, vol. 41, no. 10, pp. 2532-2548, 2002.

[Harikumar92] G. Harikumar and Y. Bresler, “Multi-spectral image visualization by projection pursuit,” *Visual. Biomed. Comput., SPIE*, vol. 1808, pp. 159-170, 1992.

[Healey99] G. Healey and D. Slater, “Invariant recognition in hyperspectral images,” in *Proc. IEEE Conference on Computer Vision and Pattern Recognition*, 1999, pp. 438-443.

[Hong98] L. Hong and A. K. Jain, “Integrating faces and fingerprints for personal identification,” *IEEE Trans. Pattern Anal. Mach. Intell*, vol. 20, no. 12, pp. 1295-1307, 1998.

[Huang05] R. Huang and M. He, “Band selection based on feature weighting for classification of hyperspectral data,” *IEEE Geosci. Remote Sens*, vol. 2, pp. 156-159, 2005.

[Huang07] J. Huang, P. C. Yuen, W-S. Chen, and J. H. Lai, “Choosing parameters of kernel subspace LDA for recognition of face images under pose and illumination variations**,”** *IEEE Transactions on Systems, Man, and Cybernetics, Part B*, vol. 37, no. 4, pp. 847-862, 2007.

[Hwang04] B. Hwang, M. Roh, and S. Lee, “Performance evaluation of face recognition algorithms on asian face database,” in *Proc. of the Sixth IEEE International Conference on Automatic Face and Gesture Recognition*, 2004, pp. 278-282.

[Ifarraguerri04] A. Ifarraguerri and M. W. Prairie**,** “Visual method for spectral band selection,” *Geoscience and Remote Sensing Letters, IEEE***,** vol. 1, pp. 101-106, 2004.

[Imai01] F. H. Imai, M. R. Rosen, and R. S. Berns, “Multi-spectral imaging of a van Gogh’s self-portrait at the National Gallery of Art, Washington, D.C,” in *Proc. of IS&T PICS*, 2001, pp. 185-189.

[Imai98] F. H. Imai and R. S. Berns, “High-resolution multispectral image archives: a hybrid approach,” in *Proc. of IS&T/ SID Sixth Color Imaging Conference*, 1998, pp. 224-227.

[IRIS03] http://www.imaging.utk.edu/files/IRISDB_0703_03.zip

[Ishiyama02] R. Ishiyama and S. Sakamoto, “Geodesic illumination basis: compensating for illumination variations in any pose for face recognition,” in *Proc. of the 16th International Conference on Pattern Recognition*, vol. 4, 2002, pp. 297-301.

[Jaehne00] B. Jaehne and K. Haussecker, *Computer Vision and Applications: A Guide for Students and Practitioners*, Academic Press, 2000.

[Jain02] A. K. Jain and A. Ross, “Learning user-specific parameters in a multibiometric system,” in *Proc. of ICIP*, 2002, pp. 57–70.

[Jiang02] L. Jiang, B. Mann, and A. Mathur, “Wavelet transform for dimensionality reduction in hyerpspectral linear unmixing,” in *Proc. of the IEEE International Geoscience and Remote Scensing Symposium*, vol. 6, 2002. pp. 3513-3515.

[Jimenez98] L. Jimenez and D. Landgrebe, “Supervised classification in high dimensional space: Geometrical, statistical, and asymptotical properties of multivariate data,” *IEEE Transactions on System, Man, and Cybernetics*, vol. 28, no. 1, pp. 39-54, 1998.

[Jin01] Y. Jin, L. Fayad, and A. Laine, “Contrast enhancement by multi-scale histogram equalization,” in *Proc. of the SPIE in Wavelet Applications in Signal and Image Processing IX San Diego*, 2001, pp. 206-213.

[Jing07] X-Y. Jing, Y-F. Yao , D. Zhang, J-Y. Yang, and M. Li, “Face and palmprint pixel level fusion and Kernel DCV-RBF classifier for small sample biometric recognition,” *Pattern Recognition*, vol. 40, no. 11, pp. 3209-3224, 2007.

[Kakadiaris05] I. A. Kakadiaris, G. Passalis, T. Theoharis, G. Toderici, I. Konstantinidis, and N. Murtuza, “Multimodal face recognition: combination of geometry with physiological information,” in *Proc. of IEEE Conference on Computer Vision and Pattern Recognition*, vol. 2, 2005, pp. 1022-1029.

[Kim04] T. K. Kim, H. Kim, W. Hwang, and J. Kittler, “Independent component analysis in a local facial residue space for face recognition,” *Pattern Recognition*, vol. 37, no. 9, pp. 1873-1885, 2004.

[Kobayashi99] F. Kobayashi, F. Arai, and T. Fukuda, "Sensor selection by reliability based on possibility measure,” in *the Proc IEEE Intl. Conference on Robotics and Automation,* vol. 4, 1999, pp. 2614-2619.

[Kohonen95] T. Kohonen, *Self-Organizing Maps*, Springer-Verlag, 1995.

[Koller96] D. Koller and M. Sahami, “Towards optimal feature selection,” in *Proc. of the 13th International Conference on Machine Learning*, 1996, pp. 284-292.

[Kong05] S. G. Kong, J. Heo, B. R. Abidi, J. Paik, and M. A. Abidi, “Recent advances in visual and infrared face recognition—a review,” *Compute, Vision Image Understanding*, vol. 97, no. 1, pp. 103-135, 2005.

[Kong07] S. G. Kong, J. Heo, F. Boughorbel, Y. Zheng, B. R. Abidi, A. Koschan, M. Yi, and M. A. Abidi, “Adaptive fusion of visual and thermal IR images for illumination-invariant face recognition,” *International Journal of Computer Vision*, vol. 71, no. 2, pp. 215-233, 2007.

[Korycinski03] D. Korycinski, M. M. Crawford, and J. W. Barnes, “Adaptive feature selection for hyperspectral data analysis using a binary hierarchical classifier and tabu search,” in *Proc. 2003 Int. Geosci. Remote Sens. Symp*, 2003, pp. 297-299.

[Koschan08] A. Koschan and M. Abidi, *Digital color image processing*, Wiley, Hoboken, New Jersey, 2008.

[Kudo00] M. Kudo and J. Sklansky, “Comparison of algorithms that select features for pattern classifiers,” *Pattern Recognition*, vol. 33, no. 1, pp. 25–41, 2000.

[Kohavi97] R. Kohavi and G. H. John, “Wrappers for feature subset selection,” *Artif Intell*, vol. 97, pp. 273-324, 1997.

[Kullback51] S. Kullback and R. A. Leibler, "On information and sufficiency,” *Annals of Mathematical Statistics*, vol. 22, pp. 79-86, 1951.

[Kumar01] S. Kumar, J. Ghosh, and M. M. Crawford, “Best basis feature extraction algorithms for classification of hyperspectral data,” *IEEE Trans. Geosci. Remote Sens*, vol. 39, no. 7, pp. 1368-1379, 2001.

[Lallier00] E. Lallier and M. Farooq, “A real time pixel-level based image fusion via adaptive weight averaging,” in *Proc. Int. Conf. Information Fusion*, vol. 2, WEC3-3- WEC3-13.

[Landgrebe02] D. Landgrebe, “Hyperspectral image data analysis as a high dimensional signal processing problem,” *IEEE Signal Proc. Mag*, vol. 19, no. 1, pp. 17-28, 2002.

[Landgrebe03] D. Landgrebe, *SignalTtheory Methods in Multispectral Remote Sensing*, 2003.

[Lanir06] J. Lanir and M. Maltz, “Impact of multispectral image fusion methods on visual search behavior,” in *Electrical and Electronics Engineers in Israel, 2006 IEEE 24th Convention*, 2006, pp. 199-202.

[Lanir06] J. Lanir, M. Maltz, I. Yatskaer, and S. R. Rotman, **“**Comparing multispectral image fusion methods for a target detection task,” in *Information Fusion, ICIF '06. 9th International Conference*, 2006, pp. 1-5.

[Lee2005] Y. J. Lee, K. H. Lee, S. B. Pan, “Local and global feature extraction for face recognition,” T.

Kanade, A. Jain, and N.K. Ratha (Eds.): *AVBPA*, LNCS 3546, pp. 219–228, 2005.

[Lee96] S. Y. Lee, Y. K. Ham and R. H. Park, “Recognition of human front faces using knowledge-based feature extraction and neuro-fuzzy algorithm”, *Pattern Recognition*, 1996, 9(11), pp 1863-1876.

[Lennon01] M. Lennon, G. Mercier, M. Mouchot, and L. Hubert-Moy, “Independent compoment anaylyssi as a tool for the dimensionality reduction and the representation of hyerpspectral image,” in *Proc. of the IEEE International Geoscience and Remote Sensing Symposium*, vol. 6, 2001, pp. 2893-2895.

[Li95] H. Li, B. S. Manjunath, and S. K. Mitra, “Multisensor image fusion using the wavelet transform,” *Graphical Models and Image Processing*, vol. 57, no. 3, pp. 235-245, 1995.

[Lissack76] T. Lissack and K. Fu, “Error Estimation in Pattern Recognition via L-Distance between Posterior Density Functions,” *IEEE Trans. Information Theory*, vol. 22, pp. 34-45, 1976.

[Liu00] C. Liu and H. Wechsler, “Evolutionary pursuit and its application to face recognition,” *IEEE trans. on Pattern Analysis and Machine Intelligence*, vol. 22, no. 6, pp. 570-582, 2000.

[Liu03] C. Liu and H. Wechsler, “Independent component analysis of gabor features for face recognition,” *IEEE Trans. Neural Networks*, vol. 14, no. 4, pp. 919-928, 2003.

[Liu06] Y. Liu, Y. Gu, Y. Zhang, and A. Wang, “Band selection based on a new seperability measure for hyperspectral images classification signal processing,” in *The 8th International Conference*, vol. 2, 2006, pp. 16-20.

[Liu06] Nan Liu, Han Wang, “Feature Extraction with Genetic Algorithms Based Nonlinear Principal Component Analysis for Face Recognition,” *Proc. IEEE of ICPR*, vol.3, pp. 461-464, 2006.

[Luis98] J. Luis and D. Landgrebe, “Supervised classification in high dimensional space: geometrical, statistical, and asymptotical properties of multivariate data,” *IEEE Trans. on System, Man, and Cybernetics*, vol. 28, pp. 39-54, 1998.

[Luo88] R. Luo and M-H. Lin, “Robot multi-sensor fusion and integration--optimum estimation of fused sensor data,” in *the Proc. of the IEEE International Conference on Robotics and Automation*, 1988, pp. 1076-108.

[Luo92] R. Luo and M. Kay, “Data fusion and sensor integration: state of art in 1990s,” *in Data Fusion in Robotics and Machine Intelligence, M. Abidi and R. Gonzalez, eds*., Academic Press, San Diego, 1992, pp.7-136.

[Luo95] R. C. Luo and M. G. Kay, *Multisensor Integration and Fusion for Intelligent Machines and Systems*, Ablex Pub, Reissue edition, 1995.

[Ma06] H. Ma, C. Jia, and S. Liu**, “**Wavelet-based PAN and multispectral image fusion,” *Intelligent Control and Automation*, vol. 2, pp. 9613-9617, 2006.

[Marschner99] S. R. Marschner, S. H. Westin, E. Lafortune, and D. Greenberg, “Image –based BRDF measurement including human skin”, *Eurographics Rendering Workshop*, 1999.

[Martin07] G. Martin, C. Lillo, and S. Mario, **“**QuickBird image fusion by a multirresolution-multidirectional joint image representation**,”** *Latin America Transactions, IEEE (Revista IEEE America Latina)* vol. 5, pp. 32-37, 2007.

[Martinez01] A. M. Martinez and A. C. Kak, “PCA versus LDA,” *IEEE trans. on Pattern Analysis and Machine Intelligence*, vol. 23, no. 2, pp. 228-233, 2001.

[Martinez98] A. M. Martinez and R. Benavente. “The AR face database,” *CVC Technical Report #24*, 1998.

[Martinez-Uso06] A. Martinez-Uso, F. Pla, J. M. Sotoca, and P. Garcia-Sevilla, "Clustering-based multispectral band selection using mutual information,” *in Pattern Recognition, 2006. ICPR 2006. 18th International Conference*, vol. 2, 2006, pp. 760-763.

[Matusita55] K. Matusita, “Decision Rules Based on the Distance for Problems of Fit, Two Samples and Estimation,” *Annals Math. Statistics*, vol. 26, pp. 631-640, 1955.

[Moghaddam02] B. Moghaddam, “Principal manifolds and probabilistic subspaces for visual recognition,” *IEEE trans. on Pattern Analysis and Machine Intelligence*, vol. 24, no. 6, pp. 780-788, 2002.

[Mugdadi03] A-R. Mugdadi and E. Munthali, **“**Relative efficiency in kernel estimation of the distribution function**,”** *Journal of Statistical Research*, vol. 37, no. 2, pp. 203-218, 2003.

[Nolle03] M. Nolle. “Distribution distance measures applied to 3-d object recognition - a case Study,” In *Proc. the 25th Pattern Recognition Symposium of the German Association for Pattern Recognition*, 2003.

[Nunez99] J., X. Nunez, O. O. Fors, A. Prades, V. Palà, and R. Arbiol, “Multiresolution-based image fusion with additive wavelet decomposition,” *IEEE Trans. on Geoscience and Remote Sensing*, vol. 37, no. 3, pp. 1204-1211, 1999.

[Ohta81] N. Ohta, K. Takahashi, H. Urabe, and T. Miyagawa, “Image simulation by use of a laser color printer, O plus E.” vol. 22, pp. 57-64, 1981.

[Ohtsuki98] T. Ohtsuki and G. Healey, “Using color and geometric models for extracting facial features,” *Journal of Imaging Science and Technology*, vol. 42, no. 6, pp. 554-561, 1998.

[O'Toole05] A. J. O'Toole, J. Harms, S. L. Snow, D. R. Hurst, M. R. Pappas, J. H. Ayyad, and H. Abdi, “A video database of moving faces and people,” *IEEE Transactions on Pattern Analysis and Machine Intelligence*, vol. 27, no. 5, pp. 812-816, 2005.

[O'Toole07] A. J. O'Toole, P. J. Phillips, J. Fang, J. Ayyad, N. Penard, and H. Abdi, “Face recognition algorithms surpass humans matching faces over changes in illumination,” *Pattern Analysis and Machine Intelligence, IEEE Transactions*, vol. 29, no. 9, pp. 1642-1646, 2007.

[Pan03] Z. Pan, G. Healey, M. Prasad, and B. Tromberg, “Face recognition in hyperspectral images,” *IEEE Transactions on Pattern Analysis and Machine Intelligence*, vol. 25, no. 12, pp. 1552-1560, 2003.

[Pan04] Z. Pan, G. Healey, M. Prasad, and B. Tromberg, “Hyperspectral face recognition under variable outdoor illumination,” in *Proc. of SPIE*, vol. 5425, 2004, pp. 520-529.

[Parkkinen88] J. Parkkinen, E. Oja, and T. Jaaskelainen, “Color analysis by learning subspaces and optical processing,” in *Proc. of the International Conference on Neural Networks*, vol. 2, 1988, pp. 421-427.

[Patrick69] E. Patrick and F. Fisher, “Nonparametric Feature Selection,” *IEEE Trans. Information Theory*, vol. 15, pp. 577-584, 1969.

[Penev96] P. Penev, J. Atick, “Local feature analysis: A general statistical theory for object representation,” *Network: Computation in Neural Systems*, vol. 7, 1996. pp. 477–500.

[Peng05] H. Peng, F. Long, and C. Ding, “Feature selection based on mutual information: criteria of max-dependency, max-relevance, and min-redundancy,” *IEEE Trans. Pattern Anal. Mach. Intell*. vol. 27, no. 8, pp. 1226-1238, 2005.

[Petrie98] G. M. Petrie, P. G. Heasler, and T. Warner, “Optimal band selection strategies for hyperspectral data sets,” in *Geoscience and Remote Sensing Symposium Proc.1998 IEEE International*, vol. 3, 1998, pp. 1582-1584.

[Phillips00] P. J. Phillips, H. Moon, S. A. Rizvi, and P. J. Rauss, “The FERET evaluation methodology for face recognition algorithms,” *IEEE trans. on Pattern Analysis and Machine Intelligence*, vol. 22, no. 10, pp. 1090-1104, 2000.

[Phillips02a] P. J. Phillips, P. Grother, R. Micheals, D. Blackburn, E. Tabassi, and J. M. Bone, “FRVT 2002 evaluation report,” *Technical Report NISTIR 6965*, Available: http://www.frvt.org, 2003.

[Philips02b] P. J. Philips, P. Grother, R. J. Micheals, D. M. Blackburn, E. Tabassi, and J. M. Bone, “FRVT 2002: overview and summary,” Available: http://www.frvt.org/FRVT2002/documents.htm, 2002.

[Phillips05] P. Phillips, P. Flynn, T. Scruggs, K. Bowyer, J. Chang, K. Hoffman, J. Marques, J. Min, and W. Worek, “Overview of the face recognition grand challenge,” in *Proc. IEEE CVPR*, vol. 1, 2005, pp. 947-954.

[Phillips06] P. J. Phillips, P. J. Flynn, T. Scruggs, K.W. Bowyer, and W. Worek, “Preliminary face recognition grand challenge results,” in *Proc. Seventh Int’l Conf. Automatic Face and Gesture Recognition*, 2006, pp. 15-24.

[Phillips98] P. J. Phillips, H. Wechsler, J. Huang, and P. Rauss, “The FERET database and evaluation procedure for face recognition algorithms,” *Image and Vision Computing Journal*, vol. 16, no. 5, pp. 295-306, 1998.

[Pizer87] S. M. Pizer and E. P. Amburn, “Adaptive histogram equalization and its variations,” *Comput. Vis. Grap, Image Process*, vol. 39, no. 3, pp. 355-368, 1987.

[Poger01] S. Poger, and E. Angelopoulou, “Selecting Components for Building Multispectral Sensors". IEEE CVPR Technical Sketches, 2001. IEEE Computer Society Press, 2001.

[Pohl98] C. Pohl and V. Enderen, “Multisensor image fusion in remote sensing: concepts methods and applications,” *International Journal of Remote Sensing*, vol. 19, pp. 823-854, 1998.

[Prabhakar02] S. Prabhakar and A.K. Jain, “Decision-level fusion in fingerprint verification,” *Pattern Recognition*, vol. 35, no. 4, pp. 861-874, 2002.

[Riklin-Raviv99] T. Riklin-Raviv and A. Shashua, “The quotient image: class based recognition and synthesis under varying illumination conditions,” in *Proc. of the IEEE Conference on CVPR*, vol. 2, 1999, pp. 23-25.

[Rissanen78] Rissanen, "Modeling by shortest data description," *Automatica*, vol. 14, pp. 465-471, 1978.

[Rogova04] G. L. Rogova and V. Nimier, "Reliability in information fusion: literature survey", in *the Proc. of the 7th Intl. Conference on Information fusion*, 2004, pp. 1158-1165.

[Rosen99] M. Rosen and X. Jiang, “Lippmann2000: a spectral image database under construction,” in *Proc. of the International Symposium on Multispectral Imaging and Color Reproduction for Digital Archives*, 1999, pp. 117-122.

[Ross03] A. Ross and A. K. Jain, “Information fusion in biometrics,” *Pattern Recognition*, vol. 24, no. 13, pp. 2115-2125, 2003.

[Roweis00] S. T. Roweis and L. K. Saul, “Nonlinear dimensionality reduction by locally linear embedding,” *Science*, vol. 290, pp. 2323–2326, 2000.

[Sadjadi05] F. Sadjadi, “Comparative image fusion analysis,” in *IEEE Computer Society Conference*, vol. 3, 2005, pp. 20-26.

[Savvides03] M. Savvides and V. Kumar, “Illumination normalization using logarithm transforms for face authentication,” in *Proc. IAPR AVBPA*, 2003, pp. 549-556.

[Scheunders00] P. Scheunders, **“**Multispectral image fusion using local mapping techniques,**”** in *Pattern Recognition, Proc. of 15th International Conference*, vol. 2, 2000, pp. 311-314.

[Scheunders01] P. Scheunders, and S. De Backer, **“**Multispectral image fusion and merging using multiscale fundamental forms,” in *Image Processing, Proc. of International Conference*, vol. 1, 2001, pp. 902-905.

[Schwarz78] G. Schwarz, "Estimating the dimension of a model," *Annals of Statistics*, vol. 6, pp. 461-464, 1978.

[Shaw02] G. Shaw and D. Manolakis, “Signal processing for hyperspectral image exploitation,” *IEEE Signal Processing Magazine*, pp. 12-16, 2002.

[Shan03] S. Shan, W. Gao, B. Cao, and D. Zhao, “Illumination normalization for robust face recognition against varying lighting conditions,” in *Proc. IEEE Workshop on AMFG*, 2003, pp. 157-164.

[Shashua97] A. Shashua, “On photometric issues in 3D visual recognition from a single 2D image,” *Internat. J. Comput. Vision 21***,** pp. 99-122, 1997.

[Shettigara92] V. Shettigara, “A generalized component substitution technique for spatial enhancement of multispectral images using a higher resolution data set,” *Photogram. Eng. Remote Sens*, vol. 58, pp. 561-567, 1992.

[Slater01] D. Slater and G. Healey, “Physics-based model acquisition and identification in airborne spectral images,” in *International Conference on Computer Vision*, 2001, pp. 257-262.

[Socolinsky01] D. A. Socolinsky, L. B. Wolff, J. D. Neuheisel, and C. K. Eveland, “Illumination invariant face recognition using thermal infrared imagery,” in *Proc. of IEEE Conference on Computer Vision and Pattern Recognition*, vol. 1, 2001, pp. 527-534.

[Sotoca04] J. M. Sotoca, F. Pla, and A. C. Klaren, "Unsupervised band selection for multispectral images using information theory," in *The 17th International Conference on Pattern Recognition (ICPR'04)*, vol. 3, 2004, pp. 510-513.

[Stoerring00] M. Stoerring, H. J. Andersen, and E. Granum, “Estimation of the illuminant colour from human skin colour,” in *IEEE Conference on Automatic Face and Gesture Recognition*, 2000, pp. 26-30.

[Stoerring99] M. Stoerring, H. J. Andersen, and E. Granum, “Skin colour detection under changing lighting conditions,” *Symposium on Intelligent Robotics Systems*, pp. 187-195, 1999.

[Swain73] P. Swain and R. King, “Two effective feature selection criteria for multispectral remote sensing,” in *International Joint Conference on Pattern Recognition*, 1973.

[Tefas01] A. Tefas, C. Kotropoulos, and I. Pitas, “Using support vector machines to enhance the performance of elastic graph matching for frontal face authentication,” *IEEE trans. on Pattern Analysis and Machine Intelligence*, vol. 23, no. 7, pp. 735-746, 2001.

[Tenenbaum00] J. B. Tenenbaum, V. Silva, and J. C. Langford, “A global framework for nonlinear dimensionality reduction,” *Science*, vol. 290, pp. 2319-2323, 2000.

[Thrun04] S. Thrun, Y. Liu, D. Koller, A. Ng, Z. Ghahramani, and H. Durrant-Whyte, “Simultaneous localization and mapping with sparse extended information filters,” *Intl. Journal of Robotics Research*, vol. 23, pp. 693-716, 2004.

[Toet03] A. Toet and E. M. Franken, “Perceptual evaluation of different image fusion schemes,” *Displays*, vol. 24, pp. 25-37, 2003.

[Toet90] A. Toet, “Hierarchical image fusion machine Vision and Applications,” pp. 1-11, 1990.

[Tominaga96] S. Tominaga, “A multi-channel vision system for estimating surface and illuminant functions,” *Journal of Optical Society of America A*, vol. 13, pp. 2163-2173, 1996.

[Tseng01] D. Tseng; Y. Chen and M. S. C. Liu, **“**Wavelet-based multispectral image fusion,” in *Geoscience and Remote Sensing Symposium, IGARSS '01. IEEE 2001 International*, vol. 4, 2001, pp.1956-1958.

[Tu07] J. L. Tu, Huang, T.S., “Locating Nosetips and Estimating Head Pose in Images by Tensorposes,” *Proc. IEEE of ICIP*, vol.4, pp. 513-516, 2007.

[Turk91] M. A. Turk, A.P. Petland, “Face recognition using eigenface,” *Proc. of IEEE Conf. on Computer Vision and Pattern Recognition*, 1991.

[Van Gemert89] M. J. C. Van Gemert, S. L. Jacques, H. J. C. M. Sterenborg, and W. M. Star, “Skin optics,” *IEEE Transactions on Biomedical Engineering*, vol. 36, no. 12, pp. 1146-1154, 1989.

[Verlinde00] P. Verlinde, G. Chollet, and M. Acheroy, “Multi-modal identity verification using expert fusion,” *Inf. Fusion***,** vol. 1, no. 1, pp. 17-33, 2000.

[Vezhnevets03] V. Vezhnevets, V. Sazonov, and A. Andreeva, “A survey on pixel-based skin color detection techniques,” in *Proc. Graphicon*, 2003, pp. 85-92.

[Vidal-Naquet03] M. Vidal-Naquet and S. Ullman, “Object recognition with informative features and linear classification,” in *International Conference on Computer vision*, 2003, pp. 281-288.

[Viola03] M. J. Viola and P. Viola, “Face recognition using boosted local features,” in *Proc. of IEEE International Conference on Computer Vision*, 2003.

[Vossepoel88] A. M. Vossepoel, B. C. Stoel, and A. P. Meershoek, “Adaptive histogram equalization using variable regions,” in *Proc. of the ninth International Conference on Pattern Recognition*, vol. 1, 1988, pp. 351-353.

[Wang05] Z. Wang, D. Ziou, C. Armenakis, D. Li, and Q. Li, “A comparative analysis of image fusion methods” *IEEE Trans. Geoscience and Remote Sensing*, vol. 43, pp. 1391-1402, 2005.

[Wang05] H-H. Wang, J. Wang, and W.Wang, “Multispectral image fusion approach based on GHM multiwavelet transform,” in *Proc. of 2005 International Conference Machine Learning and Cybernetics*, vol. 8, 2005, pp. 5043-5049.

[Wang06] H. Wang and E. Angelopoulou, “Sensor band selection for multispectral imaging via average normalized information,” *Journal of Real-Time Image Processing*, vol. 1, no. 2, pp. 109-121, 2006.

[Wang06] J. Wang, “Efficient Facial Component Extraction for Detection and Recognition,” *Proc. IEEE of ICPR*, vol. 2, pp. 1208-1211, 2006.

[Wanga07] F. Wanga, J-D. Wangb, C-S. Zhanga, and J. Kwokb, “Face recognition using spectral features,” *Pattern Recognition*, vol. 40 pp. 2786-2797, 2007.

[Wiskott97] L. Wiskott, J. M. Fellous, N. Kruger, and C. Malsburg, “Face recognition by elastic bunch graph matching,” *IEEE trans. on Pattern Analysis and Machine Intelligence*, vol. 19, no. 7, pp. 775-779, 1997.

[Withagen01] P. E. Withagen, E. den. Breejen, E. M. Franken, A. N. de Jong, and H. Winkel, “Band selection from a hyperspectral datacube for a real-time multispectral 3ccd camera,” in *Algorithms for Multispectral, Hyperspectral and Ultraspectral Imagery VII, S.S.Shen and M.R.Descour, eds., Proc. SPIE*, vol. 4381, 2001, pp. 84-93.

[Xie05] X. Xie and K-M. Lam, “Face recognition under varying illumination based on a 2D face shape model,” *Pattern Recognition*, vol. 38, pp. 221-230, 2005.

[Yocky95] D. Yocky, “Image merging and data fusion by means of the discrete two-dimensional wavelet transform,” *J. Opt. Soc. Am. A*, vol. 12, no. 9, pp. 1834-1841, 1995.

[Yocky96] D. A. Yocky, “Multiresolution wavelet decomposition image merger of landsat thematic mapper and SPOT panchromatic data,” *Photogrammetric Engineering & Remote Sensing*, vol. 62, no. 9, pp. 1067-1074, 1996.

[Yuille89] A. L. Yuille, D. S. Cohen, and P. W. Hallinan, “Feature extraction from faces using deformable templates,” *Proc. IEEE of CVPR*, 1989, pp. 104-109.

[Zhang99] Y. Zhang, M. Desai, J. Zhang, and M. Jin. “Adaptive subspace decomposition for hyperspectral data dimensionality reduction,” in *Proc. International Conference on ImageProcessing*, vol. 2, 1999, pp. 326–329.

[Zhao00] W. Zhao and R. Chellappa, “Illumination-insensitive face recognition using symmetric shape-from-shading,” in *Proc. of the IEEE Conference on CVPR Hilton Head*, 2000, pp. 286-293.

[Zhao03] W. Zhao, R. Chellappa, P. J. Phillips, and A. Rosenfeld, “Face recognition: a literature survey,” *ACM Computing Surveys*, vol. 35, pp. 399-459, 2003.

[Zhao03] J. Zhao, Y. Su, D. Wang, and S. Luo, “Illumination ratio image synthesizing and recognition with varying illuminations,” *Pattern Recognition*, vol. 24, no. 15, pp. 2703-2710, 2003.

[Zhou06] S. Zhou and R. Chellappa, “From sample similarity to ensemble similarity: probabilistic distance measures in reproducing kernel hilbert space,” *IEEE Transactions on Pattern Analysis and Machine Intelligence*, vol. 28, pp. 917-929, 2006.

[Zuo03] F. Zuo and P. H. N. de With, ‘Towards fast feature adaptation and localization for real-time face recognition systems,” *Proc. SPIE*, 2003, vol. 5150, pp. 1857-1865.

[Zuo04] F. Zuo, P.H. de With, “Fast facial feature extraction using a deformable shape model with haar-wavelet based local texture attributes,” *Proc. IEEE of ICIP*, vol.3, pp. 1425-1428, 2004.

Vita

Hong Chang was born in Tangshan, China, on January 31, 1976. After graduating in 1994 from Tangshan 1st High School, Tangshan, China, she attended Beijing University of Aeronautics and Astronautics (Beihang University) where she received both a Bachelor of Science degree in 1998 and a Master of Science degree in 2001 from the Electronic Engineering Department. During the summer of 2004, she joined the Imaging, Robotics, and Intelligent Systems Laboratory as a graduate research assistant where she completed her Doctor of Philosophy degree in 2008.